

# FLOAT – Flexible Levitation on a Track

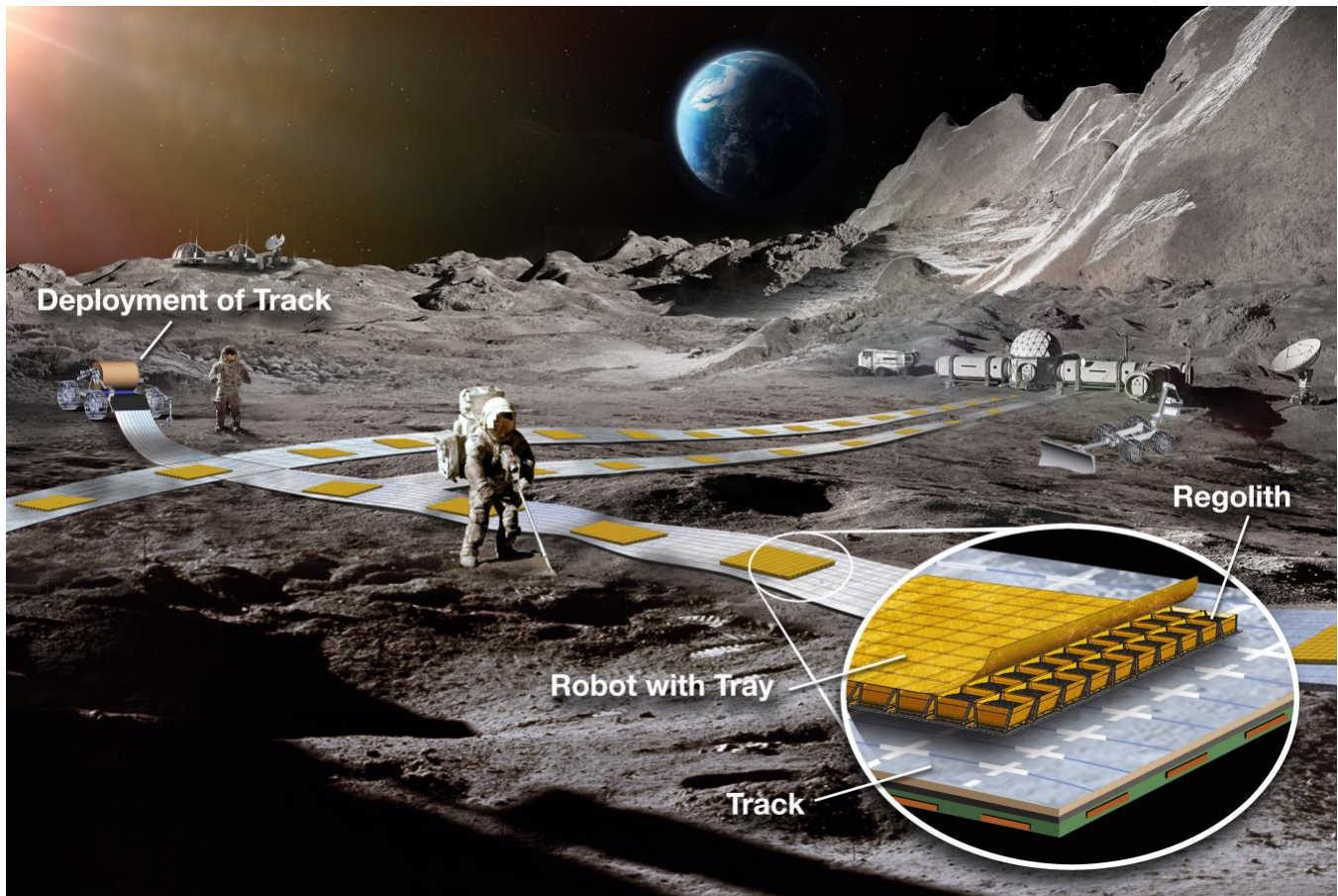
Ethan W. Schaler, Ph.D. (P.I.)

A. Scott Howe, Ph.D.

Allen Hsu, Ph.D.

Ronald Pelrine, Ph.D.

Rui J. de Gouvea Pinto



E.W. Schaler is with the Jet Propulsion Laboratory, California Institute of Technology, M/S 82-110, 4800 Oak Grove Drive, Pasadena, CA, USA, 91101

E-mail: [ethan.w.schaler@jpl.nasa.gov](mailto:ethan.w.schaler@jpl.nasa.gov).

Website: [https://www-robotics.jpl.nasa.gov/people/Ethan Schaler/](https://www-robotics.jpl.nasa.gov/people/Ethan%20Schaler/).

A.S. Howe is with the Jet Propulsion Laboratory, California Institute of Technology

A. Hsu is with SRI International

R. Pelrine was with SRI International, now with Pelrine Innovations LLC

R.J. de Gouvea Pinto is with the Jet Propulsion Laboratory, California Institute of Technology and Georgia Institute of Technology

## ABSTRACT

We propose building the first lunar railway system, to provide reliable, autonomous, and efficient payload transport on the Moon. A durable, long-life robotic transport system will be critical to the daily operations of a sustainable lunar base in the 2030's, as envisioned in NASA's Moon to Mars plan and mission concepts like the Robotic Lunar Surface Operations 2 (RLSO2), to transport regolith mined for ISRU consumables (H<sub>2</sub>O, LOX, LH<sub>2</sub>) or construction, and transport payloads around the lunar base and to / from landing zones or other outposts. We propose developing FLOAT – Flexible Levitation on a Track – to meet these transportation needs.

The FLOAT system employs unpowered magnetic robots that levitate over a 3-layer flexible film track: a graphite layer enables robots to passively float over tracks using diamagnetic levitation, a flex-circuit layer generates electromagnetic thrust to controllably propel robots along tracks, and an optional thin-film solar panel layer generates power for the base when in sunlight. FLOAT robots have no moving parts and levitate over the track to minimize lunar dust abrasion / wear, unlike lunar robots with wheels, legs, or tracks.

FLOAT tracks unroll directly onto the lunar regolith to avoid major on-site construction – unlike conventional roads, railways, or cableways. Individual FLOAT robots will be able to transport payloads of varying shape / size ( $> 30 \text{ kg/m}^2$ ) at useful speeds ( $> 0.5 \text{ m/s}$ ), and a large-scale FLOAT system will be capable of moving up to 100,000s kg of regolith / payload multiple kilometers per day while consuming  $< 40 \text{ kW}$  of power. FLOAT will operate autonomously in the dusty, inhospitable lunar environment with minimal site preparation, and its network of tracks can be rolled-up / reconfigured over time to match evolving lunar base mission requirements and can even support automated inspection, cleaning, and maintenance functions.

In this Phase 1 Report, we establish the fundamental feasibility of designing a FLOAT system with meter-scale robots that travel on km-scale tracks, to support human exploration (HEO) and ISRU activities on the Moon, through the following 4 Major Tasks:

- 1) Defining mission requirements (payload mass / size / quantity, transport distance, power, etc.) from NASA lunar base studies.
- 2) Simulating FLOAT systems with meter-scale robots / km-scales tracks in lunar conditions to refine performance estimates.
- 3) Experimenting on existing cm-scale, FLOAT-like robots to study the most pressing questions about FLOAT system feasibility.
- 4) Calculating / sizing FLOAT system designs to match mission requirements, using predicted lunar performance from simulations and experiments.

### ACKNOWLEDGEMENTS

The authors would like to thank the NASA Innovative Advanced Concepts (NIAC) program office for the opportunity to conduct this Phase I study, as well as the technical contributions from a number of Subject Matter Experts at JPL, NASA, and beyond. In particular, thank you to Mark Hetzel (JPL) and Pioneer Circuits for guidance on flex-circuit design and manufacturing considerations, and David Hinkle (JPL) for concept artwork / illustrations.

We are also extremely grateful for the positive public response / feedback to our work on FLOAT, including when presenting at the 2021 NIAC Symposium and independent outreach / inquiries made to learn more about FLOAT or share information about FLOAT with a broader audience.

The research was carried out at the Jet Propulsion Laboratory, California Institute of Technology, under a contract with the National Aeronautics and Space Administration (80NM0018D0004). The cost information contained in this document is of a budgetary and planning nature and is intended for informational purposes only. It does not constitute a commitment on the part of JPL and/or Caltech. © 2022. All rights reserved.

# CONTENTS

<b>Acknowledgements</b>	3
<b>List of Figures</b>	6
<b>List of Tables</b>	7
<b>1 Introduction</b>	8
1.1 FLOAT Concept Overview . . . . .	9
1.1.1 FLOAT Performance . . . . .	9
1.1.2 FLOAT Innovation . . . . .	10
1.2 FLOAT Mission Context . . . . .	10
1.3 Phase I Key Findings . . . . .	12
<b>2 Background</b>	13
2.1 Lunar Environment . . . . .	13
2.1.1 Regolith Properties . . . . .	13
2.1.2 Distribution of Lunar Rocks / Craters . . . . .	13
2.1.3 Thermal Conditions . . . . .	15
2.1.4 Shackleton Crater . . . . .	16
2.2 Lunar Transportation Options . . . . .	17
2.3 Diamagnetic Levitation . . . . .	18
2.4 Lunar Solar Power . . . . .	19
2.4.1 Thin-Film Solar Cells & Space-Rated Flexible Solar Cells . . . . .	20
<b>3 Simulations</b>	21
3.1 Levitation Analysis . . . . .	21
3.1.1 Lunar Payload versus Magnet Geometry and Graphite Thickness . . . . .	23
3.1.2 Out-of-Plane Curvature Analysis . . . . .	26
3.2 Electromagnetic Drive Analysis . . . . .	29
3.2.1 Equations of Motion . . . . .	30
3.2.2 Force Analysis . . . . .	31
3.2.3 Incline Analysis . . . . .	32
3.2.4 Velocity Analysis . . . . .	34
3.2.5 In-Plane Curvature Analysis . . . . .	35
3.3 Magnetic Confinement Analysis . . . . .	36
3.3.1 Magnetic Dipole-Dipole Confinement . . . . .	36
<b>4 Experiments</b>	39
4.1 10 cm <sup>2</sup> Magnet Array . . . . .	39
4.1.1 Motion Analysis . . . . .	39
4.2 Dust and Abrasion Testing . . . . .	41
4.3 Life-Cycle Testing . . . . .	42
4.4 Flexible Compliant Robots . . . . .	44
4.5 Magnetization and Repair of Magnets . . . . .	45
4.6 Vacuum Testing . . . . .	46
<b>5 System Design</b>	48
5.1 Trade Space Analysis . . . . .	48
5.1.1 Track Configurations . . . . .	48
5.1.2 Trade Space Analysis Results . . . . .	49
5.1.3 Future System Model Development . . . . .	50
5.1.4 FLOAT Sizing for RLSO2 . . . . .	51
5.1.5 Cost-of-Transport Comparison . . . . .	54
5.2 Phase I System Design . . . . .	55
5.2.1 Modular Track Concept . . . . .	55
5.2.2 Control Electronics . . . . .	56
5.2.3 Integrated CAD Concept for FLOAT System / Deployment . . . . .	57
5.2.4 Cost Analysis . . . . .	58

FLOAT – FLEXIBLE LEVITATION ON A TRACK	5
<b>6 Conclusion</b>	60
6.1 Open Questions for Future Investigation	60
6.2 Potential Impact	61
<b>References</b>	63
<b>Biographies</b>	66
Ethan W. Schaler, Ph.D. (NASA JPL)	66
Allen Hsu, Ph.D. (SRI International)	66
Ronald Pelrine, Ph.D. (SRI International / Pelrine Innovations)	66
A. Scott Howe, Ph.D. (NASA JPL)	66
Rui J. de Gouvea Pinto (NASA JPL / Georgia Institute of Technology)	66

# LIST OF FIGURES

1.1	FLOAT Mission Concept	8
1.2	FLOAT Hardware Overview	9
1.3	RLSO2 Mission Overview	11
2.1	Lunar Soil Particle Parameters and Lunar Soil Simulant	14
2.2	Lunar Rock and Crater Size-Frequency Distributions	15
2.3	Shackleton Crater Topography	16
2.4	Solar Flux Calculations Diagram	19
3.1	Simulation Overview	21
3.2	Diagram for Diamagnetic Levitation Analysis	22
3.3	Magnet Arrays (Configurations)	23
3.4	Magnet Arrays (Magnetic Fields)	23
3.5	Lunar Levitation Payload for Various Magnet Geometries and Graphite Thicknesses	24
3.6	Lunar Payload for Various Magnet Geometries, with Fixed Levitation Gap and Graphite Thickness	25
3.7	Lunar Levitation Payload for Varying Magnet Thickness	26
3.8	Levitation Gap vs. Out-of-Plane Curvature	27
3.9	Simulated Compliant Robots with Flexures	28
3.10	Design Space for Compliant Robots	29
3.11	Diagram of Electromagnetic Drive	29
3.12	Electromagnetic Force and Interaction	30
3.13	Electromagnetic Force vs Area Power Density	31
3.14	Diagram of Incline	32
3.15	Incline vs Power/Area and Power/Total Mass	33
3.16	Robot Max Velocity due to Effect of Graphite Thickness on Eddy Current Drag	34
3.17	Maximum Velocity vs. Turn Radius and Power	36
3.18	Simulated Magnetic Dipole-Dipole Attractive / Repulsive Forces	37
3.19	Passive Magnetic Confinement Concept	38
4.1	10 cm <sup>2</sup> Magnet Array	39
4.2	Motion Analysis for 10 cm <sup>2</sup> Robot	40
4.3	Dust and Abrasion Testing	41
4.4	Dust Plow Robot Concept	42
4.5	Protective Sleeve Concept	42
4.6	Life Cycle Testing	43
4.7	Rigid and Compliant Robots Traversing a Crater	44
4.8	Robot Demagnetization / Remagnetization	45
4.9	Remagnetization Procedure	46
4.10	Operation of Diamagnetic Levitated System within a Scanning Electron Microscope	47
5.1	Track Configuration Options	49
5.2	System Trade Space Analysis: Robot Speed v. Payload Capacity v. Robots	50
5.3	System Trade Space Analysis: Robot Speed v. Track Distance v. System Mass	51
5.4	System Trade Space Analysis: Robot Speed v. Track Distance v. Net Power Generation / Consumption	52
5.5	System Trade Space Analysis: Robot Speed v. Track Distance v. Total System Packing Volume	53
5.6	Power and Cost of Transport Comparison	55
5.7	Modular Track Concept	56
5.8	Control Electronics	57
5.9	Concept for FLOAT Robot, FLOAT Track, and Track Deployment Robot	58

**LIST OF TABLES**

2.1	Summary of Lunar Regolith Properties . . . . .	13
2.2	Comparison of Alternative Lunar Transportation Systems . . . . .	17
2.3	Table of Diamagnetic Materials . . . . .	18
2.4	Thin-Film Solar Cell Materials . . . . .	20
5.5	Cost Analysis for FLOAT . . . . .	59



## 1 INTRODUCTION

In the next decade, NASA plans to reestablish a human presence on the Moon. Manned Artemis missions planned for the mid- to late-2020s will deliver a series of human landers to the lunar south pole and beyond, while unmanned missions will facilitate technology demonstrations of in-situ resource utilization (ISRU) and water ice resource exploration (VIPER) before culminating in the first Lunar Surface Asset deployment [1], [2]. NASA is poised to establish a sustainable, human-rated base at a lunar pole by the 2030s [1]–[3], and we propose to build with it the first lunar railway system – to provide reliable, autonomous, and efficient robotic payload transport on the Moon.

A durable, long-life robotic transport system will be critical to daily operations of an established lunar base, with robots (semi) autonomously performing repetitive tasks and reducing astronaut workload by: transporting mined regolith and consumables (H<sub>2</sub>O, LH<sub>2</sub>, and LOX) to ISRU processing / construction sites; and transporting payloads between base modules (potentially even through airlocks), or to lunar landers, scientific test sites, and other outposts.

Any viable system must function in an extreme environment (-170 to +130°C, abrasive dust, electrostatic charging) with minimal site preparation (landscaping vs. demolition, road / railway construction). It must operate on limited electrical power, move at reasonable speeds with good spatial accuracy, and use autonomous controls simple enough to run on radiation-hardened microprocessors yet robust enough to avoid frequent faults that require human intervention.

In Phase I, we investigated developing a deployable and reconfigurable lunar transport system – hereafter called Flexible Levitation on a Track (FLOAT) – that’s ideal for automated robotic transportation of raw materials, scientific instruments, and other variably-sized payloads. The FLOAT system (Fig. 1.1 and 1.2) is composed of unpowered magnetic robots and a 3-layer flex-circuit track: the graphite layer enables robots to passively float over tracks using diamagnetic levitation, the flex-circuit layer generates electromagnetic thrust to controllably propel robots along tracks, and the optional thin-film solar panel (similar to NASA’s ROSA [4]) allows power generation during lunar day operations.

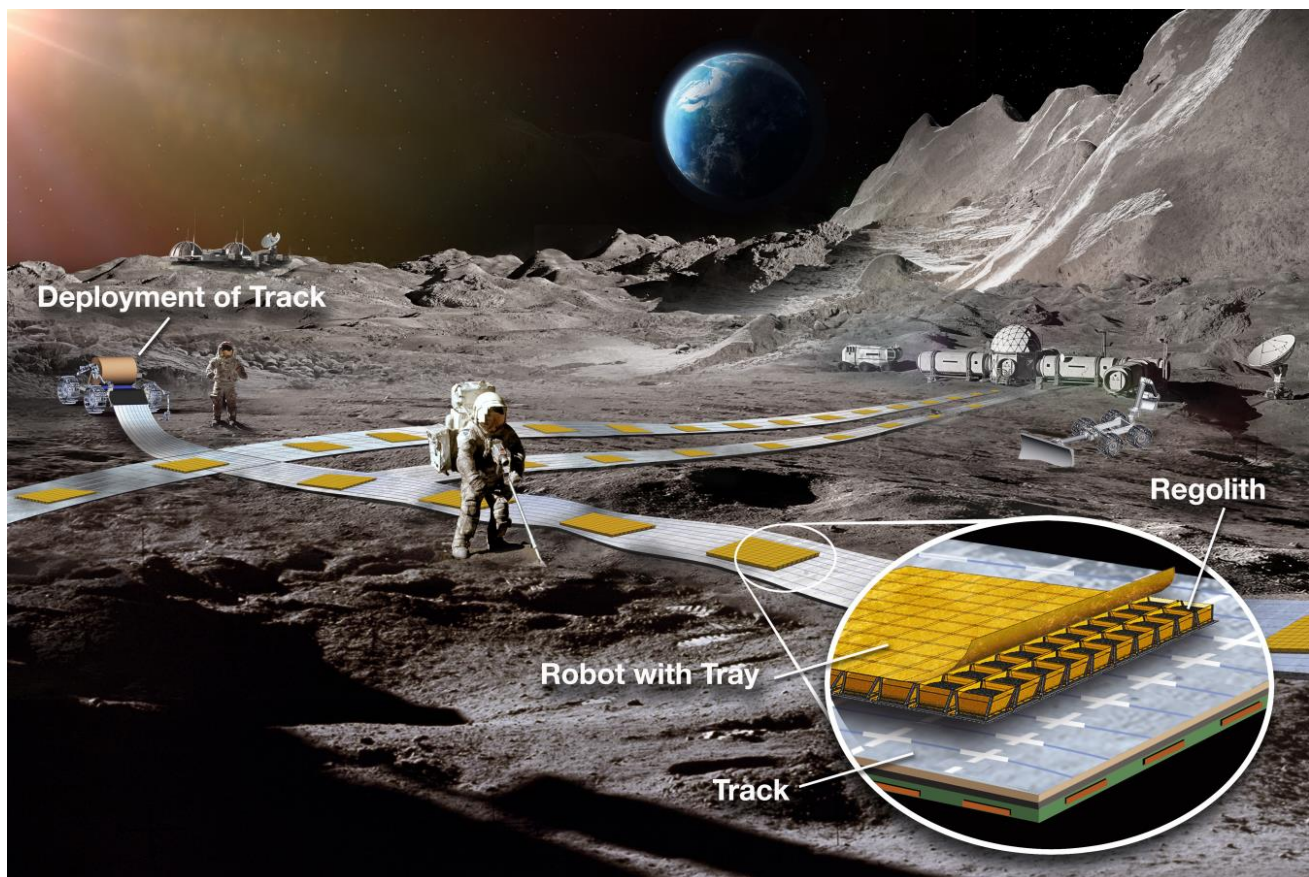


Fig. 1.1: FLOAT Mission Concept



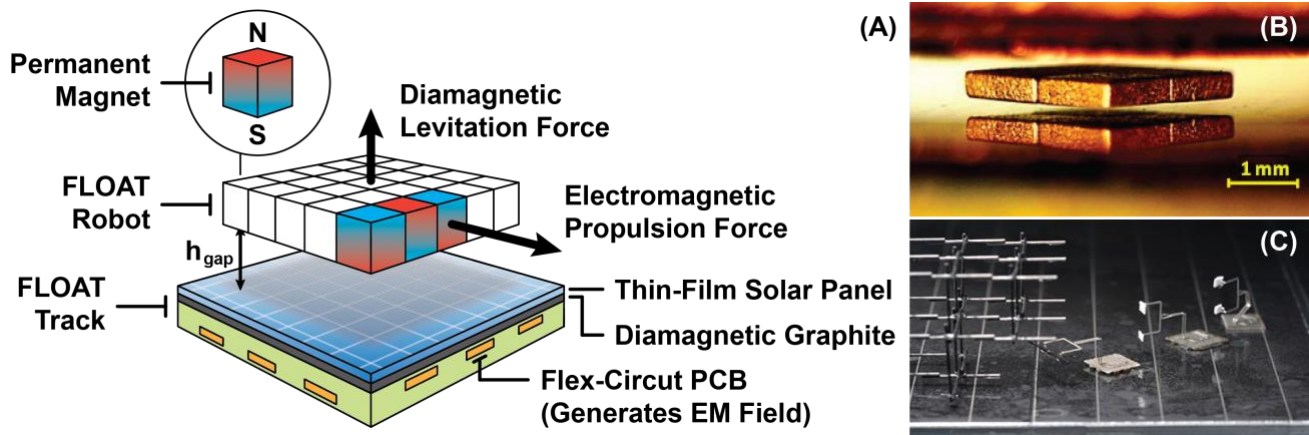


Fig. 1.2: FLOAT diagram (A), with robot levitating over track at height ( $h_{gap}$ ) and currents (+I, -I) generating electromagnetic fields that exert a propulsion force on the robot. (B) One magnet robot levitating over its own reflection, and (C) three robots with truss-assembly tools [5], [6].

FLOAT tracks will be unrolled directly over the lunar terrain and reconfigured as-needed to form a robotic transport network connecting lunar landing zones, ISRU-mining sites, and modules for habitation, scientific research, and manufacturing. Studying FLOAT now establishes a path to lunar tech demos in this decade and full-scale deployment in the 2030s.

## 1.1 FLOAT Concept Overview

### 1.1.1 FLOAT Performance

FLOAT's core technology – DiaMagnetic Micro Manipulator (DM3) by SRI International – has been demonstrated using cm-scale robots with mg-payloads operating in a clean, Earth-based lab [6]–[9]. See the video below for details. In Phase I, we demonstrated the fundamental feasibility of scaling DM3 by  $10^2$ - $10^4$ x to build meter- / kg-scale robots for the Moon.

**Video:** Magnetically Actuated Micro-Robots for Advanced Manufacturing

**Link:** <https://www.youtube.com/watch?v=Bxb3-bT8uxk>

On Earth, these robots currently hover at  $\sim 100 \mu\text{m}$  gaps and generate levitation pressures that support payloads of  $3 \text{ kg/m}^2$  (30 Pa). The electrical power to confine floating robots in-place is  $\sim 15 \text{ W/m}^2$  of robot area or  $\sim 2.5 \text{ W/kg}$  of robot mass, and supplying additional electrical power enables lateral motion (acceleration ( $a$ ) is proportional to current ( $I$ ), and power ( $P$ ) squared). On the Moon ( $1/6 \text{ g}$ ), our initial calculations predict FLOAT performance will dramatically improve:

**System Mass:** 3-6  $\text{kg/m}^2$  robots and 1-2  $\text{kg/m}^2$  tracks, with easy assembly in  $1/6$  gravity

**System Payload:**  $\sim 30 \text{ kg/m}^2$  (11x Earth payload, and  $>15$ x with design improvements)

**Power Use:** 36x reduction in lunar gravity, to  $<< 30 \text{ mW/kg}$  and  $<< 1 \text{ W/m}^2$  for motion on flat terrain and  $< 0.15 \text{ W/kg}$  and  $< 5 \text{ W/m}^2$  on slopes up to 30 degrees. Frictionless lateral motion without air resistance allows ballistic gliding between powered acceleration phases

**Solar Power:** Flexible, thin-film solar panels have thicknesses as small as  $2.3 \mu\text{m}$  (organic cell) [10] and have demonstrated efficiencies up to 20.4% (CIGS cells) [11]

**Motion:** 0.55 m/s max tested translation speed (air drag limited),  $>> 1 \text{ m/s}$  expected on Moon

Creating articulated robots (magnets linked with flexible joints) and integrating a lightweight load distribution mechanism on top can also facilitate transport of both uniformly distributed (e.g. lunar regolith) and compact (e.g. fuel cannisters) payloads without locally bottoming-out on the track.

This document has been reviewed and determined not to contain export controlled technical data.

### 1.1.2 FLOAT Innovation

Considerable funding has been allocated via NASA programs like NIAC and GCD to design key aspects of a lunar base, including: power (Kilopower, ROSA) [4], [12], reusable landers (Human Landing System) [1], sustainable human-rated habitats [1], heavy-lift utility robots (ATHLETE) [13], ISRU-mining robots (RASSOR) [14], and human-rated transporters (Space Exploration Vehicle, SEV) [15]. FLOAT is designed to complement existing robots – ATHLETE can deploy FLOAT tracks, and FLOAT robots can transport ore mined by RASSOR – and physically link these NASA initiatives together to form a sustainable lunar base.

Current lunar robots use wheels (SEV, RASSOR) [14], [15], legs (Spidernaut) [16], or wheel-on-leg hybrids (ATHLETE) [13] for mobility. Unlike these motor-driven robots, FLOAT robots are solid-state (no motors, gearboxes, or other moving parts) and consist only of permanent magnets connected in planar arrays. As a result, they are lightweight (3-4 kg/m<sup>2</sup>), unpowered (no batteries), easily repairable, and reconfigurable in size from cm- to meter-scale. The lunar environment poses significant hazards that limit robot life, so we plan to investigate how FLOAT can avoid or mitigate these risks:

**Dust Abrasion:** Robot levitation ( $\sim 100\ \mu\text{m}$ ) is larger than magnetic dust particle size ( $< 20\ \mu\text{m}$ ) [17] and no actuated joints minimizes wear to robot and track (unlike wheels / legs).

**Dust Mitigation:** Floating robots don't kick up dust while moving (unlike wheels / legs), and tracks can self-clean with electrostatic dust repulsion [18], [19], or FLOAT robots with brushes / magnets / charged surfaces.

**Triboelectric Charging:** Reduced, since FLOAT robots don't touch the lunar surface, and additional mitigations like discharge spikes can be added

**Vacuum / Temperature Effects:** Flexures within the track and magnet robots minimizes consequences of thermal expansion mismatch ( $-170$  to  $+130^\circ\text{C}$  temp. cycles), and temperatures around the lunar south pole are notably more stable and cooler across the lunar day [20]. Neodymium magnets have Curie temps.  $> 300^\circ\text{C}$  and alloys that maintain field strength at lunar temps. Other mitigations are available, such as multi-layer insulation covers, to shield the magnets from extreme heat in non-polar regions.

**Power Consumption:** No need for heat-to-use during night operations (a major power drain for motors). FLOAT's solar panels can potentially generate net positive power in sunlight.

Multiple FLOAT robots can operate simultaneously and independently on the same track with sub-millimeter positioning accuracy, using an open-loop control scheme similar to linear stepper-motors. Like conventional railway systems, FLOAT tracks only consume power in regions that are actively maneuvering robots, and the tracks can be manufactured with standardized forms and junctions to allow modular deployment. Unlike conventional rail systems, FLOAT tracks generate power in sunlight, need little site-preparation (no foundation / ballast), are lightweight (metal rails have  $> 40\times$  mass), and can be rolled up for transport, storage, or reconfiguration as missions evolve.

## 1.2 FLOAT Mission Context

NASA / JPL have developed numerous lunar base concepts, as natural extensions of Artemis, Lunar Gateway, and other programs. The mission we will focus upon in this NIAC proposal – and see FLOAT as a critical enabling technology for – is the Robotic Lunar Surface Operations 2 (RLSO2) concept [21]–[24], which was conceived by NASA JPL, NASA Ames, and others. A coauthor of the RLSO2 concept (Dr. A. Scott Howe), is a member of this NIAC Study.

The RLSO2 mission proposes a permanent lunar South Pole base (Fig. 1.3), with the goal to:

“build and operate a human-tended base that produces enough oxygen and hydrogen from lunar polar ice In-Situ Resource Utilization (ISRU) for four flights per year of a reusable lander shuttling between the Lunar Gateway and the base.” [22]

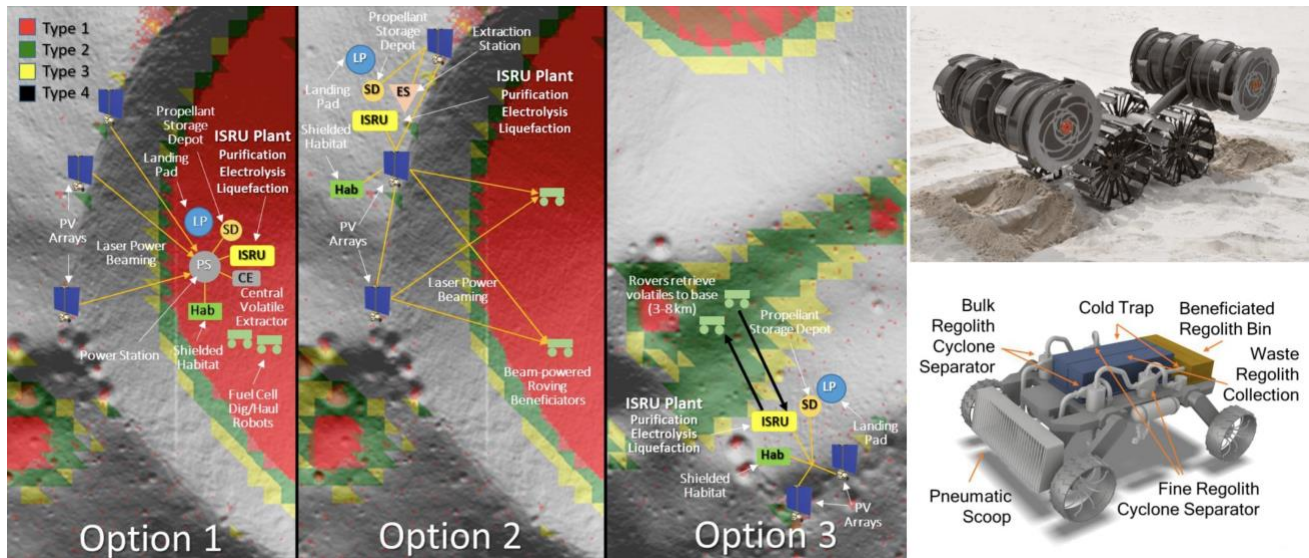


Fig. 1.3: (Left) RLSO2 mission options: base / mining within Shackleton crater (Option 1), base on Shackleton rim / mining in crater (Option 2), base / mining on Shackleton West Ridge (Option 3) [21], [22]. (Right, Top) RASSOR mining lunar simulant [14] and (Right, Bottom) model of an extractor / beneficiator rover [24].

RLSO2 identifies three possible mission options (see Fig. 1.3) that yield the required 1,130 kg/day of water. The relevant transportation requirements are highlighted below, from [21], [22]:

**Option 1:** Full base / mining located in Shackleton Crater (permanently shadowed region)

- **Ice:** <1 km to high-quality ice (2 wt%, 20-100 cm deep); no in-field regolith processing.
- **Transport:** 7-9 bucket Excavator rovers dig and move 236,000 kg/day of raw regolith.

**Option 2:** Full base located on Shackleton Rim (in full sunlight), mining in Shackleton Crater

- **Ice:** ~10 km to high-quality ice (2 wt%, 20-100 cm deep); in-field beneficiation to 5.7 wt%.
- **Transport:** 7-9 pneumatic Beneficiator Rovers yield 80,000 kg/day of beneficiated regolith.

**Option 3:** Full base / mining located on Shackleton West Ridge (in partial sunlight)

- **Ice:** ~3-8 km to mid-quality ice (1 wt%, 40-100 cm deep); in-field volatile extraction.
- **Transport:** Many corer-based volatile Extractor rovers produce 1,130 kg/day of water.

The RLSO2 study has no dedicated transportation system for mined regolith / ice, and instead relies on the ISRU-mining rovers for material transport. Each rover must thus drive >2 hours per trip between mine / base – reducing time for mining, consuming limited onboard power, carrying unnecessary mass (mining equipment), and accumulating wear during non-mining activities.

FLOAT can easily integrate into all three RLSO2 mission options, to perform the repetitive, long-distance transportation of regolith / volatiles from mining sites to ISRU extraction / processing plants to dumping sites. In this role, FLOAT can dramatically improve the RLSO2 mission feasibility – and reduce the required number of mining vehicles by up to 75% – by enabling the regolith-mining rovers to be used exclusively on the complex, high-value task of resource extraction and minimizing rover driving time. This also minimizes wear on rover mobility systems (extending operational life), and reduces rover mobility as a constraint on site selection.

The unique reconfigurability of FLOAT tracks permits this system to regularly be extended / rerouted to terminate at active mining sites (unlike rail or cable systems). FLOAT’s ability to traverse steep grades may also allow it to serve as the ‘resource escalator’ needed to climb the Shackleton crater slope (in Option 2), and our Phase I work shows that electromagnetically pushing robots with large payloads up steep slopes remains a viable strategy (see Fig. 5.6b).

### 1.3 Phase I Key Findings

FLOAT Simulation Results (backed by empirical data) and proof-of-concept experiments reaffirmed that FLOAT's diamagnetic levitation robots have a viable path to implementation as a Lunar transportation system with meter-scale robots / kilometer-scale tracks.

**FLOAT Simulation Results** – We refined models of robot levitation force under lunar conditions, for multiple robot / track designs (e.g. magnet size / pattern, track layer thicknesses), and identified manufacturable robot / track configurations that achieve 50-100  $\mu\text{m}$  levitation gaps (1-2x mean lunar regolith particle sizes [25], [26]) while carrying  $>30 \text{ kg/m}^2$  payloads. We also created analytical models of electrical power required to propel robots with a range of payloads / velocities up slopes of varying steepness and around turns of various radii of curvature; and built finite-element models to estimate required robot compliance to conform to varying lunar terrains (and confirmed model agreement with tests of physical compliant robot prototypes). Results show that FLOAT robots maintain extremely low power requirements over a range of terrains – using  $<5 \text{ W/m}^2$  or  $<0.15 \text{ W/kg}$  to carry up to  $30 \text{ kg/m}^2$  payload on tracks with slopes  $<40^\circ$  and curves  $>5 \text{ m}$  in-plane radius or  $>25 \text{ m}$  out-of-plane radius – and use 10-100x less power for transport than wheeled vehicles.

**FLOAT Experimental Results** – We successfully built a  $10 \text{ cm}^2$  robot ( $\sim 10\times$  larger in area than prior state of the art) and operated it with open-loop control to measure mobility characteristics. We also constructed a compliant robot, composed of 4 magnet arrays (that passively repel one another) linked by film flexures, and demonstrated it can levitate over / conform to non-flat bowls, while an equivalently-sized rigid magnet robot bottoms out and gets stuck. Robot compliance and scaling are critical preconditions for operating on non-flat terrain with limited site preparation.

In addition, we have demonstrated track debris clearing and track resilience to abrasion, by first applying lapping compound (at similar size-scales to lunar regolith) to the track, then using a robot to push away the debris, and finally running a robot over that cleared patch of track for  $\sim 600 \text{ m}$  (53,500 cycles).

**FLOAT System Engineering within Mission Context** – We have built a model that combines the robot / track performance estimates from our simulation / experimental results with parameters of the Robotic Lunar Surface Operations 2 (RLSO2) mission concept to generate system design estimates – e.g. number of robots, length of track, peak power consumption, and mass / volume – for a complete transportation system that meets RLSO2 regolith volumetric flow requirements. We have also developed concepts for track deployment robots and refined designs for multi-panel tracks (to mitigate thermal effects) and track junctions / turns (to accommodate misalignment).



## 2 BACKGROUND

### 2.1 Lunar Environment

The Lunar environment presents a number of interesting challenges to robotic or human operations, including: abrasive regolith (Sec. 2.1.1), large variation in rock sizes (Sec. 2.1.2), large diurnal temperature variation combined with a thermally insulating regolith (Sec. 2.1.3), and low gravity (which affects maximum terrain steepness, Sec. 2.1.4).

#### 2.1.1 Regolith Properties

Lunar regolith properties have been studied in detail since some of the earliest lunar lander missions (Luna 13's penetrometer in 1966 [27] and Surveyor III's soil mechanics surface sampler in 1967 [28]), and subsequent sample-return missions by the United States (Apollo 11, 12, 14-17) in 1969-72, Soviet Union (Luna 16, 20, 24) in 1970-76, and China (Chang'e 5) in 2020 have further enhanced our understanding of regolith composition, size distribution, and mechanical behaviors. An overview of lunar regolith properties is provided in Table 2.1, and discussed in greater detail below.

D. Kring [29], [30], reported that regolith particles are dominantly  $< 1\text{ mm}$  in size, with mean particle size of  $70\text{ }\mu\text{m}$ , median 50% particle size range of  $40\text{-}130\text{ }\mu\text{m}$ , and approximately 10-20% are finer than  $20\text{ }\mu\text{m}$ . Average particle elongation is 1.35, average aspect ratio is 0.55, and average roundness is 0.22. Additional details on particle distribution is shown in Fig. 2.1c.

It's also important to note that [30] presents evidence, first reported by Apollo astronauts, of small permanently-shadowed regions (PSRs) underneath boulders that have no discernible differences from adjacent lunar regolith outside these PSRs. This provides support for generalizing lunar regolith properties observed around the Lunar south pole in non-PSRs to the regolith expected to be found within PSRs like Shackleton crater.

W.D. Carrier [31], studied soil samples obtained from seven landing sites on the Moon (Apollo 11, 12, 14, 15, 16, and 17; Luna 24), and reports that 95% of the soil is finer than  $1.37\text{ mm}$ , and 5% finer than  $0.0033\text{ mm}$ , with an average/median particle size of  $0.072\text{ mm}$ . Particle size distribution of lunar soil is very consistent, and 68% of the data points fall in a narrow band. They also suspect that lunar soil may be internally erodible. Additional details on particle distribution is shown in Fig. 2.1a.

C. Meyer [32] reports that the lunar regolith layer is  $10\text{ m}$  thick in highland surfaces,  $5\text{ m}$  thick in mare surfaces, and presents another particle size-frequency distribution in Fig. 2.1b.

L.A. Taylor [17] aggregates investigations into the magnetic properties of lunar soils, and reveals that coarse-grained magnetized particles  $>20\text{ }\mu\text{m}$  can be separated with a magnet, while fine-grained magnetized particles  $<20\text{ }\mu\text{m}$  clump together with other particles of similar size and behave as if all particles have relatively high magnetic susceptibility.

Lunar regolith simulants attempt to generate mixtures of particles that closely match the physical particle size distributions, chemical compositions, and/or terramechanical properties (e.g. soil compaction, inter-particle friction, etc.), to support various experiments on Earth. Simulants previously used by NASA include JSC-1, NU-LHT, OB-1, and LHS-1. A comparison of LHS-1 simulant to Apollo 16 soil samples is shown in Fig. 2.1d.

#### 2.1.2 Distribution of Lunar Rocks / Craters

The prevalence of boulders, craters, hills, sink-holes, and other non-flat terrain on the Moon is well documented. Deployment of a viable track system like FLOAT will require navigating around / over such obstacles, or else performing sufficient site preparation / landscaping to remove excessively large obstacles.

Table 2.1: Summary of Lunar Regolith Properties.

Source	Mean Particle Size	Notes
D. Kring [29]	$70\text{ }\mu\text{m}$	10-20% of regolith is smaller than $20\text{ }\mu\text{m}$
W.D. Carrier [31]	$72\text{ }\mu\text{m}$	95% of the soil is finer than $1.37\text{ mm}$
C. Meyer [32]	–	50% of soil is smaller than $100\text{ }\mu\text{m}$ , 90% of the soil is finer than $1\text{ mm}$
L.A. Taylor [17]	–	50 wt% is $<50\text{ }\mu\text{m}$

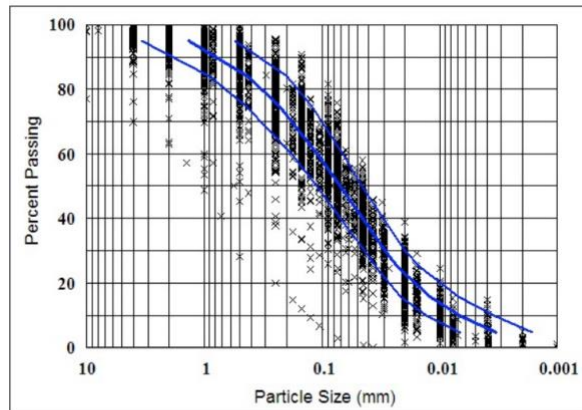
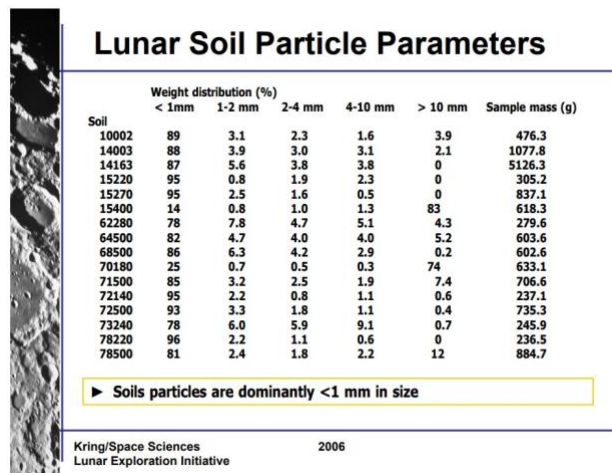


Fig. 1: Lunar soil particle size distribution (Carrier 2003).  
The middle curve shows the average distribution; the left-hand and right-hand curves show  $\pm$  one standard deviation.  
On average, approximately 2% coarse sand (2.0 to 4.75 mm); 14% medium sand (0.425 to 2.0 mm); 33% fine sand (0.074 to 0.425 mm); and 51% silt.

(a) Lunar soil particle parameters, from [31].



(c) Lunar soil particle parameters, from [29].

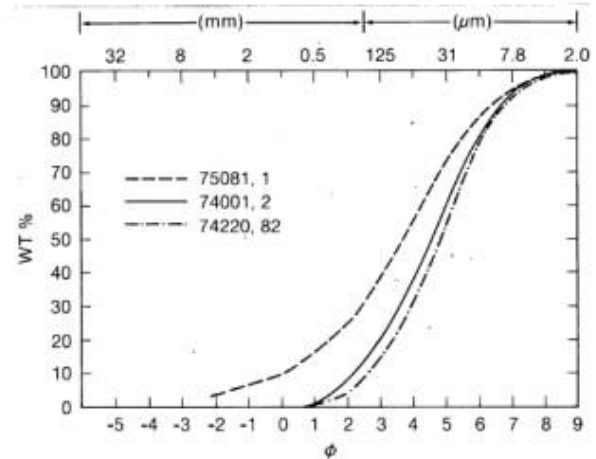
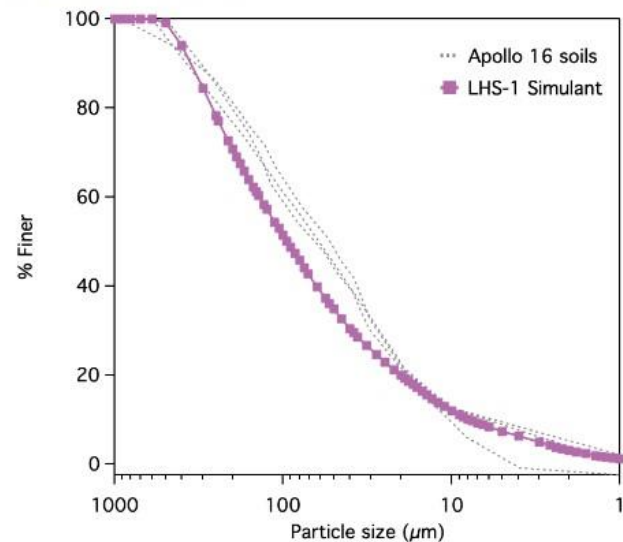


Figure 55 - Grain size distribution of mature lunar soil (75081) and orange soil (74220). About 10 percent of a lunar soil is greater than 1 mm, 50 percent is greater than 100 microns, and 90 percent is greater than 10 microns (from Heiken *et al.* 1974).

(b) Lunar soil particle parameters, from [32].

Particle size distribution:

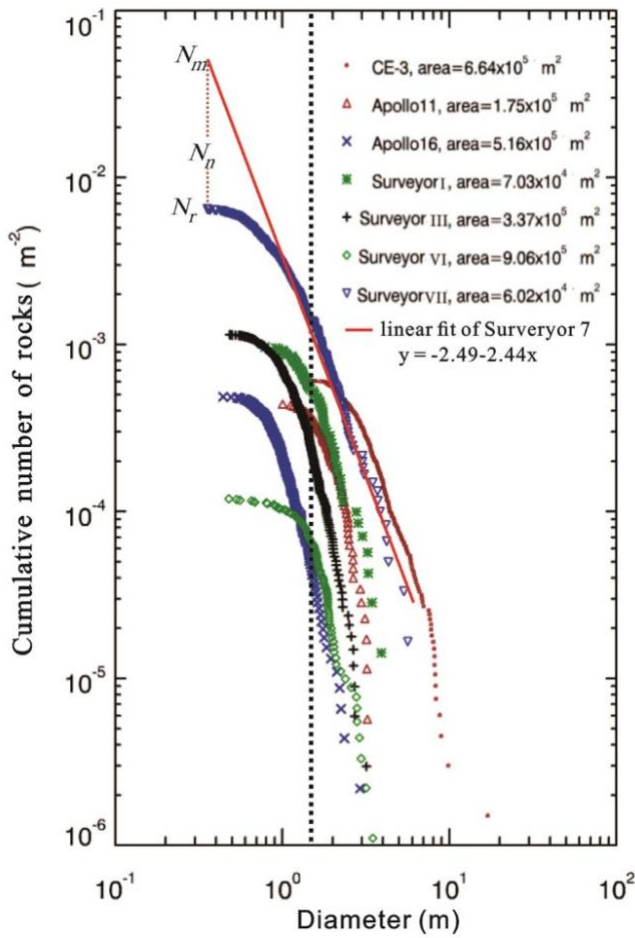


(d) Lunar Regolith Simulant, compared to Apollo 16 soil samples, from [33].

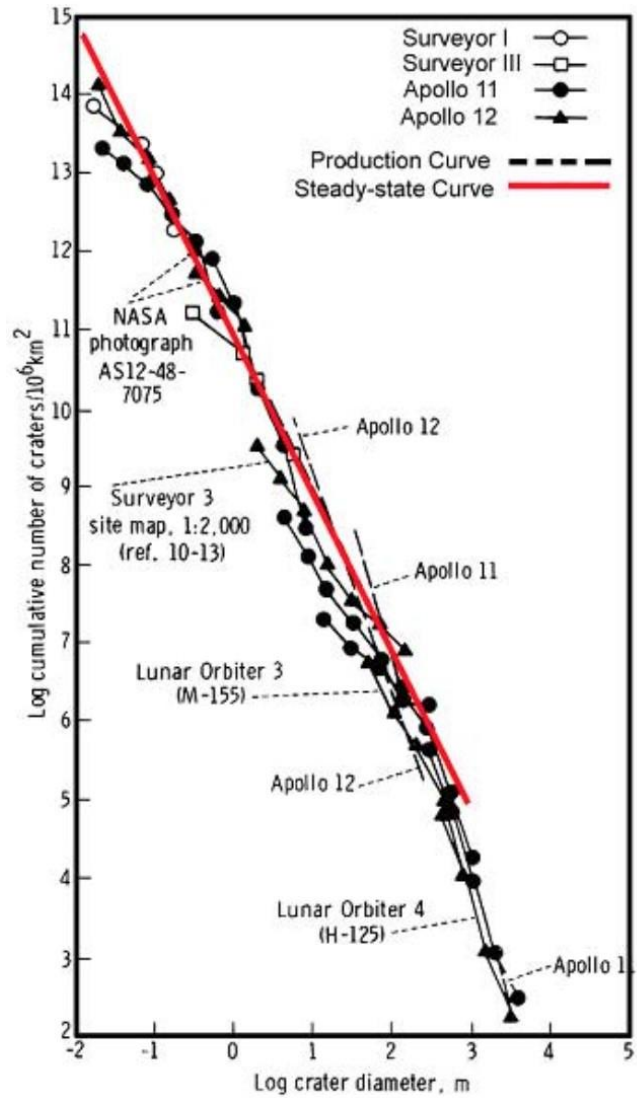
Fig. 2.1: Lunar Soil Particle Parameters, from [29], [31], [32] as well as comparison to a lunar soil simulant [33].

B. Wilcox [34] provides a model for determining the mean free path of a rover within a field of boulders (on Mars). While this work focuses on Martian rover traversability, the methods are applicable to the problem of deploying segments of straight tracks on the lunar surface and estimating the degree of terrain landscaping that will be required before surveying an actual Lunar site in detail.

Considerable work has also been performed to estimate the Lunar rock size-frequency distribution [35]–[39], using a combination of imagery from the Lunar Reconnaissance Orbiter (LRO) narrow-angle camera (LRO-NAC), and multi-spectral thermal infrared data from the LRO Diviner Radiometer (LRO-DR). Similar work has also been performed to estimate lunar



(a) Lunar rock size-frequency distributions, from [38].



(b) Lunar crater size-frequency distributions, from [40].

Fig. 2.2: Lunar rock [38] and crater [40] size-frequency distributions.

crater size-frequency distributions [40]. Two plots of this data are provided in Fig. 2.2.

J.L. Bandfield, C. Elder and teams [35]–[37] leverage differing thermophysical properties between rocks and regolith to identify / estimate rock size-frequency density from thermal imagery. They also report that this technique produces estimates of derived rock concentrations that have both qualitative and quantitative agreement with LRO-NAC / camera data, although results are limited to between 60°N/S and thus do not include regions of interest around the Lunar south pole.

B. Li and team [38], [39] identified and analyzed rock size based on high contrast illuminated / shadowed rock faces in LRO-NAC imagery at a number of sites visited by prior missions, including Apollo 11 / 16, Surveyor I / III / VI / VII, and Chang’e 3. They also focused on data with large sun angles (i.e. closer to the horizon) to increase rock shadow sizes.

### 2.1.3 Thermal Conditions

Surface temperature on the Moon range from +127°C / 400 K (in full Sun) to -173°C / 100 K (during lunar night) over its 27.3 day orbital period [41].

At the Lunar poles, permanently shadowed regions (PSRs) within craters experience substantially lower temperatures – -248°C to -203°C / 25 K to 70 K – that make these locations ideal for preserving volatile ice deposits [42], [43]. Regions near the lunar poles that are not within PSRs, however, remain in near-perpetual sunlight with the sun close to the horizon.



This creates a comparatively benign average surface temperature of  $-23$  to  $-3^{\circ}\text{C}$  /  $250$  to  $270$  K year-round [20].

Apollo astronauts measured thermal conductivity of lunar regolith using heat-flow probes, and noted that thermal conductivity of the surface regolith is exceptionally low: starting at  $1.5 \times 10^{-3}$  W/m-K in the top 1-2 cm, before increasing sharply at 2 cm by 5-7x, and then more gradually increasing with depth to approximately  $1.5 \times 10^{-2}$  W/m-K at a depth of 1 meter [29]. Regolith temperature is stable and unaffected by thermal day / night cycling by 80 cm depth. Other work relying on LRO Diviner Radiometer data shows wider variation in solid thermal conductivity across the lunar regolith of  $1 \times 10^{-4}$  W/m-K to  $3 \times 10^{-2}$  W/m-K depending on location [44].

Lunar regolith is thus a highly insulating material, especially when compared to more standard insulating materials (0.035 - 0.16 W/m-K) – such as fiberglass (0.04 W/m-K), and silica aerogel (0.02 W/m-K) – and conductors – copper (384 W/m-K) and graphite (168 W/m-K) – that are found on Earth. As a result, radiative heat transfer into space will be the dominant dissipation method for all heat generated by currents running through the track (Ohmic losses).

### 2.1.4 Shackleton Crater

As the RLSO2 Mission concept focuses on lunar base sites around / in the Shackleton crater, it is also important to note additional geological characteristics of this large crater, which is located nearly coincident with the lunar south pole, as described in [43], [45], [46].

Shackleton crater has a 20 km diameter at the rim, and 7 km diameter at the floor (see Fig. 2.3). The crater has an average wall slope of 31 degrees and maximum slope of approximately 35 degrees (roughly equivalent to 36 degree angle of repose for regolith on the Moon) [43], [46]. The crater wall smoothly transitions from the  $\sim 35$  degree rim to a nearly-flat floor over course of  $\sim 1$  km.

A majority of the Shackleton crater is a PSR, and thus it is a leading location on the Moon for finding permanently sequestered volatiles (such as water ice).

Highly-detailed maps of Shackleton crater can be found in [43], including a high-resolution elevation map of the floor of Shackleton and illumination percentage of the terrain in / around the crater.

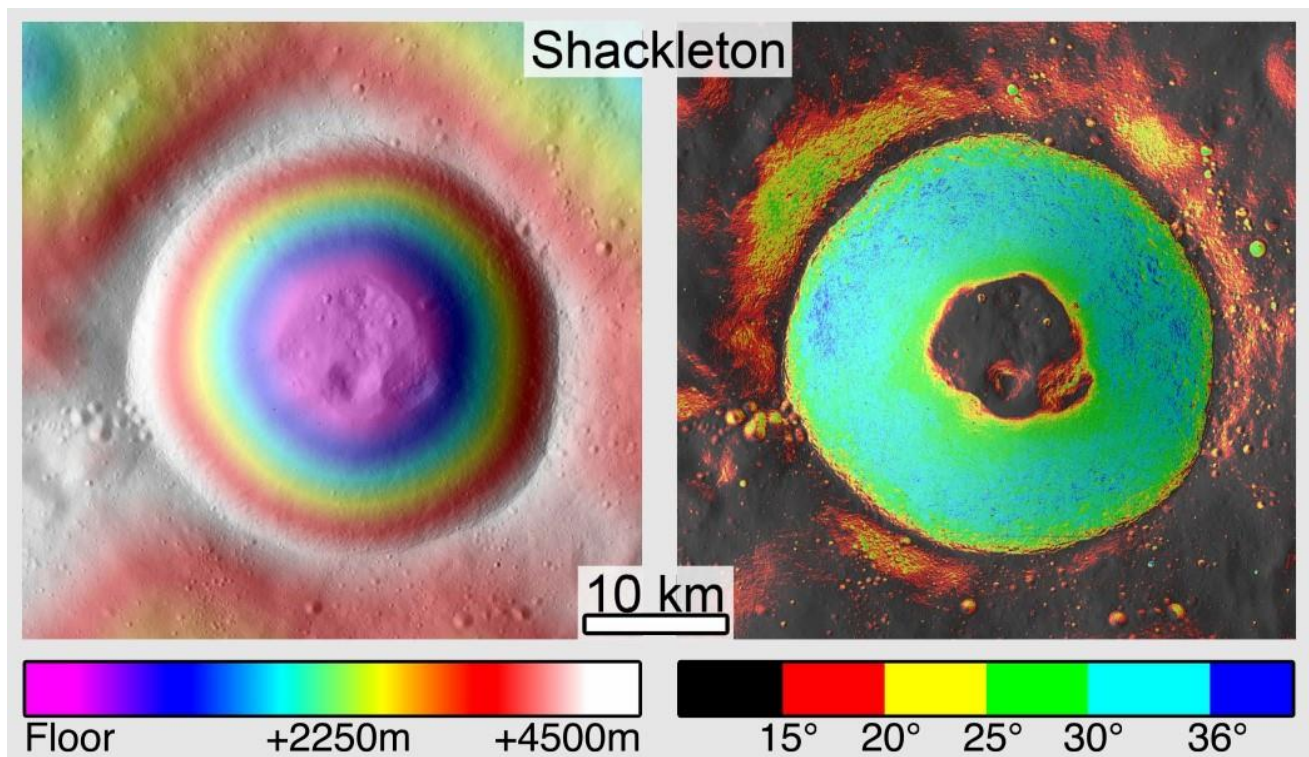


Fig. 2.3: Shackleton Crater Topography, from [46].

## 2.2 Lunar Transportation Options

A preliminary comparison of FLOAT's capabilities to those of alternative transportation systems is provided in Table 2.2. It is clear, that a successful lunar base will employ a variety of robotic vehicles with complementary attributes:

**Rovers** are best used for operations on unstructured terrain and that take advantage of special capabilities beyond mobility (ISRU mining, outpost construction, etc.).

**Fliers** are fast and able to move supplies to / from the Moon or between remote points on its surface, but use expendable fuel and are the most expensive vehicles.

**Rail, Cable, or FLOAT** are ideal for established routes, where up-front infrastructure costs are offset by higher efficiency, simple automation, and reduced maintenance.

Among this last category of transport systems, FLOAT is unique in that it is also easily deployable / reconfigurable, is dramatically lower mass, is entirely solid-state (no moving parts), and requires minimal site preparation or heavy construction equipment (no foundation / towers). NASA has invested heavily in new lunar rovers and fliers, without a commensurate investment in rail or cable systems. The successful development of FLOAT will enable a great leap in lunar surface transport capabilities for NASA and the greater (lunar-focused) aerospace community.

A more detailed comparison of rover performance versus FLOAT performance, focusing primarily on power and cost of transport is included in Sec. 5.1.5.

Table 2.2: Comparison of lunar transport systems (rovers, fliers, rail / cable, and FLOAT).

No / Yes = N / Y Good = + Neutral = o Poor = -		[kg] Mass (Vehicle)	[kg/m] Mass (Road, Rail, Cable)	[kg] Payload (Lunar)	[m/s] Speed	Cost	Fuel / Efficiency	Infrastructure / Setup	Maintenance / Wear	Debris Generation
System	Notes									
<b>Rovers</b>										
Tri-ATHLETE	All-terrain heavy transport	1.4K	N	10K	< 2.0	\$\$	o	+	-	o
P@X	Multi-function mobile gantry	6.6K	N / Y	15K	-	\$\$	-	+ / -	-	o
Excavator	Excavator transport rover	> 1K	N / Y	3.5K	-	\$\$	-	+ / -	--	-
Excav. / Benef.	Excavator / beneficiator rover	> 1K	N / Y	525	-	\$\$\$	-	+ / -	--	-
Extractor	Volatile extraction rover	>> 1K	N / Y	< 1K	-	\$\$\$	--	+ / -	-	o
RASSOR	Low-gravity excavator rover	67	N	90	0.49	\$\$	o / -	+	-	-
<b>Fliers</b>										
Artemis Landers	Repurposed lunar lander craft	3-22K	N	1-3.6K	++	\$\$\$	-	+	o	--
RLSO2 Lander	Purpose-built lunar freighter	> 42K	N / Y	30K	++	\$\$\$	-	+ / o	o	--
<b>Rail &amp; Cable</b>										
Track & Train	Mono- and dual-rail systems	> 500	> 40	Large	+	\$\$	+	-	+	+
Mag-Lev Train	Magnetic levitation railway	>> 500	>> 40	Large	++	\$\$\$	+	--	++	+
Cable Railway	Suitable for steep grades	> 500	> 42-50	Large	o	\$\$	+	--	o	+
Aerial Lift	Cable-suspended system	> 50	2-20	Large	o	\$\$	+	o / -	o	+
<b>FLOAT</b>	<b>Ultra-light rail alternative</b>	<b>3/m<sup>2</sup></b>	<b>1-2</b>	<b>&gt; 33/m<sup>2</sup></b>	<b>0.55</b>	<b>\$</b>	<b>+</b>	<b>o</b>	<b>o / +</b>	<b>+</b>

### 2.3 Diamagnetic Levitation

Diamagnetism is a property relating how a material's magnetic flux density ( $\mathbf{B}$ ) responds in the presence of an applied magnetic field ( $\mathbf{H}$ ). This relationship is written in Eq. 2.1:

$$\mathbf{B} = \mu_0(1 + \chi)\mathbf{H} \quad (2.1)$$

Where,  $\mu_0$  is the vacuum permeability, and  $\chi$  is the volume magnetic susceptibility [47]. Diamagnetic materials are those materials where  $\chi < 0$ , which implies that a diamagnetic material partially repels an external applied field and in turn can generate a repulsive force as shown by the magnetic force density on a material written in Eq. 2.2:

$$\nabla \chi \mathbf{H} \cdot \mathbf{B} = \nabla \frac{\chi}{\chi+1} \frac{\mathbf{B}^2}{\mu_0} \approx \nabla \frac{\chi}{\mu_0} \mathbf{B}^2 \quad (2.2)$$

This repulsive force is passively generated when a permanent magnet is placed in the vicinity of a diamagnetic material and it allows for the passive generation of **stable levitation configurations**, as Earnshaw's Theorem forbids stable levitation only for materials where  $\chi > 0$ .

Unfortunately,  $|\chi| \ll 1$  for many materials at room temperature, such that the repulsive levitation forces are relatively weak, as shown in Table 2.3. Super-conductors are perfect diamagnets (i.e. they repel all incident magnetic fields) and have  $\chi = -1$ , however they typically require exotic / expensive materials and only operate at extremely cold temperatures. These limitations make it challenging to operate a FLOAT-style system using super-conductors, and thus drive our focus towards more readily-available materials that still exhibit diamagnetic properties.

The idea of levitating an object using diamagnetic levitation originated in 1847 by William Thomson [48]; however, it wasn't demonstrated until 1939 by Werner Braunbek [49] using a strong electromagnet. Since then various configurations of diamagnetically stabilized levitation have been demonstrated including stable diamagnetic levitation of a living frog [50], [51].

Due to the small forces, the applications on Earth are limited as compared to other active levitation approaches using electromagnets or Eddy currents. One of the recent advances in completely passive levitation has been the introduction of high magnetic field strength rare-earth magnets such as Neodymium-Iron-Boron (NdFeB), which are necessary for self-levitation.

In recent years, members of the FLOAT team have been investigating the applications of diamagnetic levitation on small scales (i.e. microns to millimeters) for micro-manipulation and micro-assembly applications, where levitation enables controllable motions with extremely high levels of precision ( $\sim nm$ ) [52]–[54].

On Earth, performance is excellent at these miniature size scales, but diamagnetic levitation force and robot weight scale unfavorably in larger robots (due to operating under Earth gravity). On the Moon, in contrast, the robot weight is 1/6 that on Earth but the diamagnetic levitation force remains the same, allowing robots to carry significantly larger payloads relative to their own body weight.

Table 2.3: Table of Diamagnetic Materials, based on [55].

Material	$\chi$ [SI]
Superconductor	-1
Pyrolytic Graphite (Out-of-Plane)	$-59.5 \times 10^{-5}$
Pyrolytic Graphite (In-Plane)	$-0.85 \times 10^{-5}$
Bismuth	$-16.4 \times 10^{-5}$
Copper	$-0.96 \times 10^{-5}$
Water	$-0.91 \times 10^{-5}$

## 2.4 Lunar Solar Power

In order to calculate the power generation of the track's solar panels it is necessary to model the solar irradiance on the moon's surface over the course of a lunar day at varying latitudes. A model to calculate solar radiation on the moon has been developed for engineering purposes [56] comprised of the following equations (see also Fig. 2.4):

$$E_{dir}(t) = TSI \cdot \cos(\delta(t)), \text{ in } \left[ \frac{W}{m^2} \right] \quad (2.3)$$

$$\delta = \arccos(\sin(h) \cdot \sin(h_p) + \cos(h) \cdot \cos(h_p) \cdot \cos(A_n - A)) \quad (2.4)$$

$$A_n = \frac{\pi}{2} - A_p \quad (2.5)$$

$$A = \arcsin\left(\frac{\sin \varepsilon}{\cosh}\right) \quad (2.6)$$

$$h = \arcsin(\cos \phi \cdot \cos \varepsilon) \quad (2.7)$$

$$\varepsilon = t \cdot \frac{1}{t_s} \cdot 2\pi \quad (2.8)$$

Where,

$E_{dir}$  = Direct solar irradiance on a flat surface  $\left( \frac{W}{m^2} \right)$

$TSI$  = Average total solar irradiance on the moon, value assumed to be  $1363.03 \frac{W}{m^2}$

$\delta$  = Angle of incidence for solar radiation (*rad*)

$h$  = Solar altitude (*rad*)

$h_p$  = Plane's normal elevation (*rad*)

$A_n$  = Azimuth angle of the plane normal (*rad*)

$A$  = Azimuth angle of the sun (*rad*)

$A_p$  = Azimuth angle of the plane, equivalent to the latitude on the moon (*rad*)

$\varepsilon$  = Length of arc drawn by sun between time steps

$\phi$  = Longitude on the moon (*rad*)

$t$  = Time from the start of the lunar day (Earth days)

$t_s$  = Length of a lunar day, 29.53 Earth days

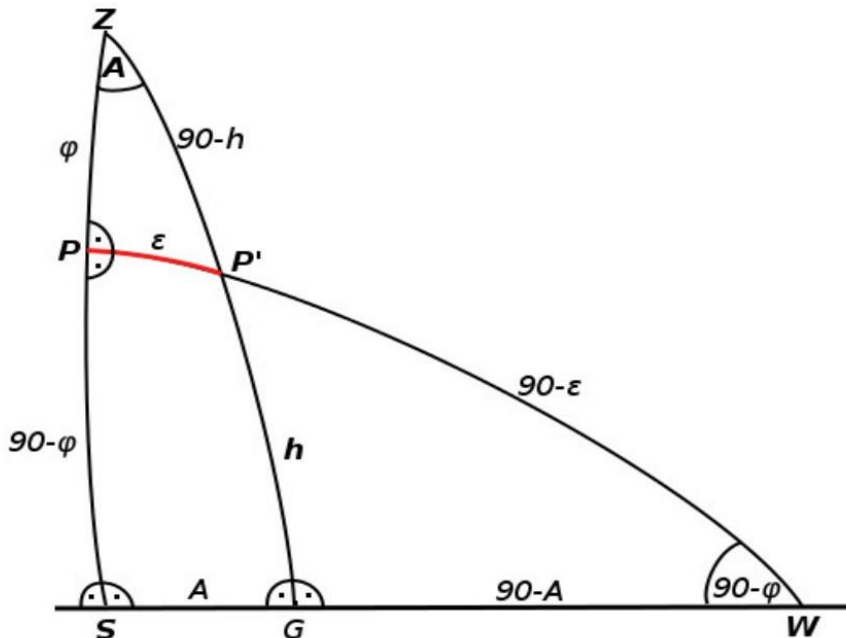


Fig. 2.4: Solar Flux Calculations Diagram: Visual representation of the terms defined in equations: 2.3-2.8. Figure from [56].

Using this set of equations we are able to model the solar irradiance at a given latitude and given time on the moon. For different RSLO2 mission options we can then calculate the solar irradiance we expect to see on the track’s solar panels to estimate the power generation of the solar panels. In our power estimations, the solar irradiance is calculated at 100 different time steps across the Lunar day, which allows us to determine the average and peak solar irradiance over the course of a lunar day for a given latitude.

#### 2.4.1 Thin-Film Solar Cells & Space-Rated Flexible Solar Cells

There are various flexible thin film solar technologies available that would be candidates for the solar panel layer of the FLOAT track. NASA has experimented with roll-out solar array [4] (ROSA) technology and has deployed it on the ISS. Additionally, there are other technologies in development such as GaAs solar cells [57], CIGS solar cells [58], and Parylene-C coated cells [59]. An efficiency of up to 20.4% can be achieved with these thin film solar cells, this is the value that we use in our models to estimate the power generation of the track [11]. Table 2.4 lists the various technologies and their properties. Most of these technologies have only been demonstrated at small-scales, so advancements in their manufacturing processes will be necessary before use on FLOAT.

Table 2.4: Thin-Film Solar Cell Materials [11], [57]–[59]

Technology	Cost	Efficiency	Manufacturing Process	Thickness
Parylene-C	$\$14/m^2$	2.3%	Pyrolytic Polymerization	215 nm
GaAs	$\$10k/m^2$	19.9%	Soft Nanoimprint Lithography	205 nm
CIGS	—	20.4%	Sputtering	1500 nm

### 3 SIMULATIONS

FLOAT Phase I simulations have focused on modelling the physics and dynamics of a scaled up diamagnetically levitated track in a lunar environment (Figure 3.1). The following is the list of input design parameters for the FLOAT track:

$w_{magnet}$  – width of individual magnet  
 $h_{magnet}$  – height of individual magnet  
 $h_{graphite}$  – thickness of graphite  $I_x$  –  
 current in X-oriented traces  
 $h_{X,trace}$  – separation between magnet and X-oriented traces  $I_y$  –  
 current in Y-oriented traces  
 $h_{Y,trace}$  – separation between magnet and Y-oriented traces

By varying these input parameters, we can examine the design and trade-off space for the following properties:

$h_{gap}$  – levitation gap  
 $F_{levitate}$  – diamagnetic levitation forces  
 $F_{thrust}, F_{confinement}$  – lateral in plane forces  
 $P$  – power consumption  
 $F_{drag}$  – Eddy Current Drag

With these fundamental physical variables, we can then extract out relevant system parameters such as (1) Lunar Payload (Sec. 3.2.2), (2) Maximum Incline vs Power (Sec. 3.2.3), (3) Maximum Velocity (Sec. 3.2.4), (4) Maximum In-Plane Curvature (Sec. 3.2.5), and (5) Maximum Out-of-Plane Curvature (Sec. 3.1.2), which all factor in as inputs into our system level design in Sec. 5.

Due to the small magnetic susceptibility of the graphite and the large magnetic fields generated by NdFeB relative to the current in the traces, we can separate the analysis of diamagnetic levitation (Sec. 3.1) from the forces from the electromagnetic drive (Sec. 3.2).

#### 3.1 Levitation Analysis

The levitation force ( $F_z$  or  $F_{levitate}$ ) in a planar configuration is proportional to the difference in z-component of the magnetic flux density ( $B_z$ ) normal to the top and bottom surface of the graphite (Eq. 3.9). This equation can also be derived from the volume

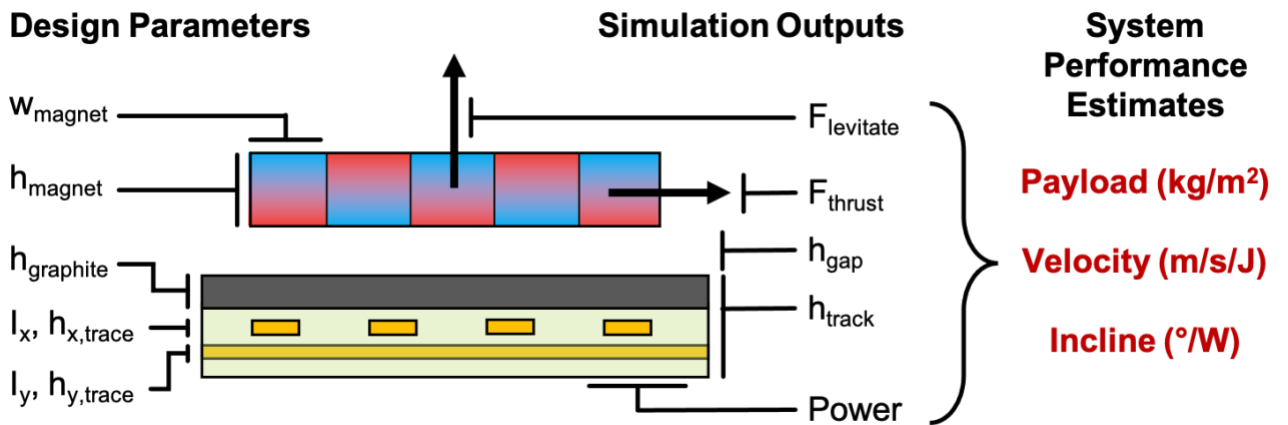


Fig. 3.1: Simulation Overview



integral of Eq. 2.2 and the application of the Divergence theorem, resulting in:

$$F_z = \frac{1}{2} \chi_{\text{graphite}} \iint_A [B_{z,\text{top}}^2 - B_{z,\text{bot}}^2] dx dy \quad (3.9)$$

Where  $\chi_{\text{graphite}}$  is the magnetic susceptibility of graphite,  $B_{z,\text{top}}^2$  and  $B_{z,\text{bot}}^2$  is the z-component of the magnetic flux density at the top and bottom of the graphite, as shown in Figure 3.2. The magnetic flux density is generated passively by the rare earth magnets (Neodymium Iron Boron - NdFeB) and whose strength is proportional to the volume and geometry of the individual magnets ( $w_{\text{magnet}}$ ,  $h_{\text{magnet}}$ ).

To compute the forces, we utilized finite element simulations (FEM) using COMSOL 5.5. While analytical solutions and methods have also been used previously, finite element methods provided more rapid prototyping and analysis of more complex magnetic geometries (i.e. Hallbach). Figure 3.3 shows the two magnet array configurations – Standard (Checkerboard) arrays and Hallbach arrays – that are passively diamagnetically stable and were analyzed for our FLOAT design. These arrays, and their matching in-track drive electrode trace patterns, follow existing designs [53] and provide generally equal lateral, inplane forces (in X and Y). Other track patterns can be used to optimize other control aspects, but utilizing the track design in [53] has multiple operational advantages: it enables control of both large and small robots on the same track, and it enables 2 degrees-of-freedom (DOF) control, which in turn permits track junctions, lateral confinement, compensation due to track misalignments, and the ability to avoid parts of the track (i.e. debris, electrical failure, etc).

The standard magnet array consists of a checkerboard magnetic array of alternating north / south magnetic dipoles. The Hallbach magnet array is very similar except in between neighboring magnets there are additional magnetic dipoles oriented with their dipole in the XY plane, as opposed to the Z direction, which results in an asymmetry in the magnetic flux above and below the magnet array.

Figure 3.4 shows a COMSOL simulation of the  $|B|$  and  $B_z$  for both the standard versus Hallbach configurations. In the standard configuration the B field along the top and bottom surfaces of the magnet array are symmetric and equal, while for a Hallbach

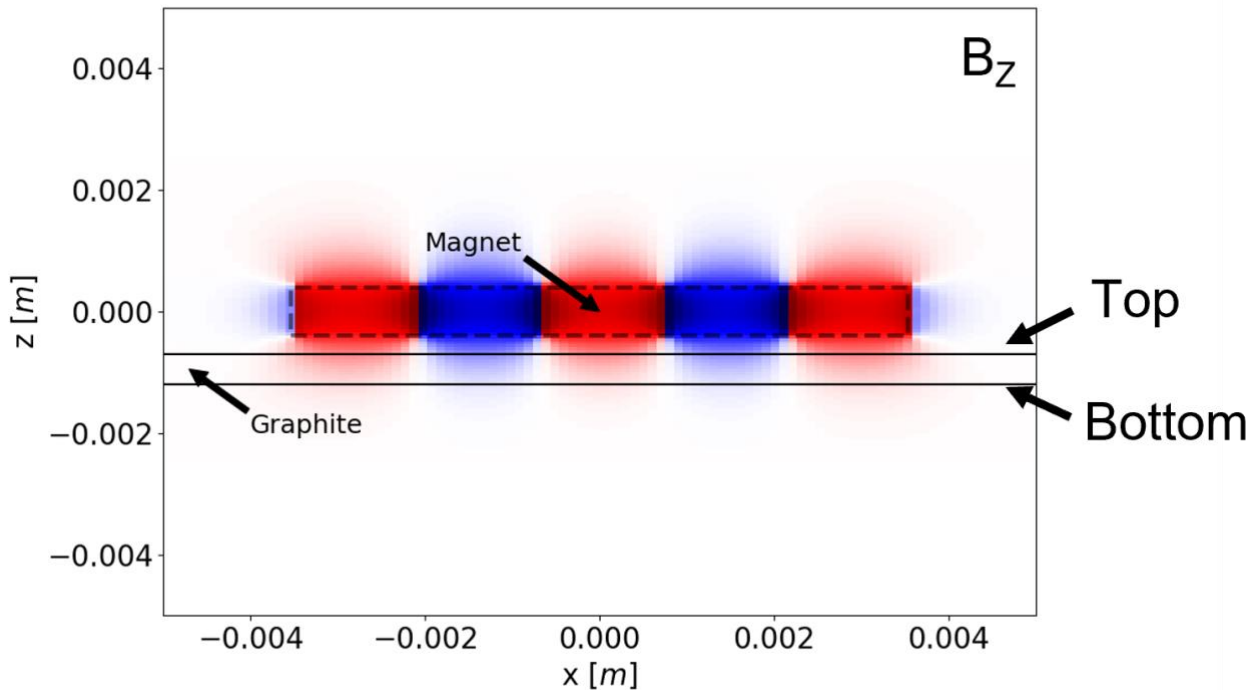


Fig. 3.2: Diagram for Diamagnetic Levitation Analysis, showing a cross section of  $B_z$  for a standard magnet array.



Standard Magnet Array

Hallbach Magnet Array

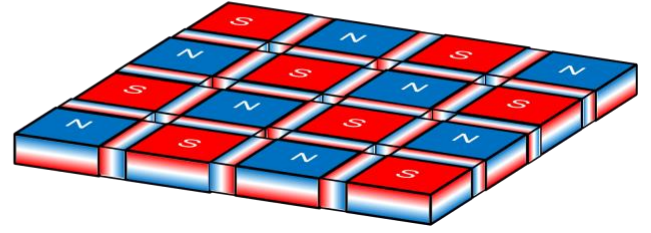
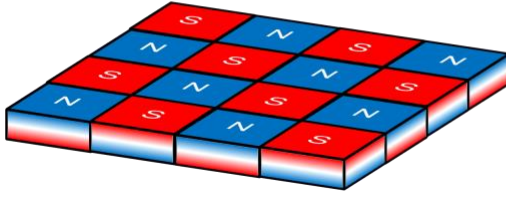


Fig. 3.3: Magnet Array Configurations – Illustrations of a Standard (Checkerboard) magnet array (left) vs. Hallbach magnet array (right), colored by idealized magnetization orientations.

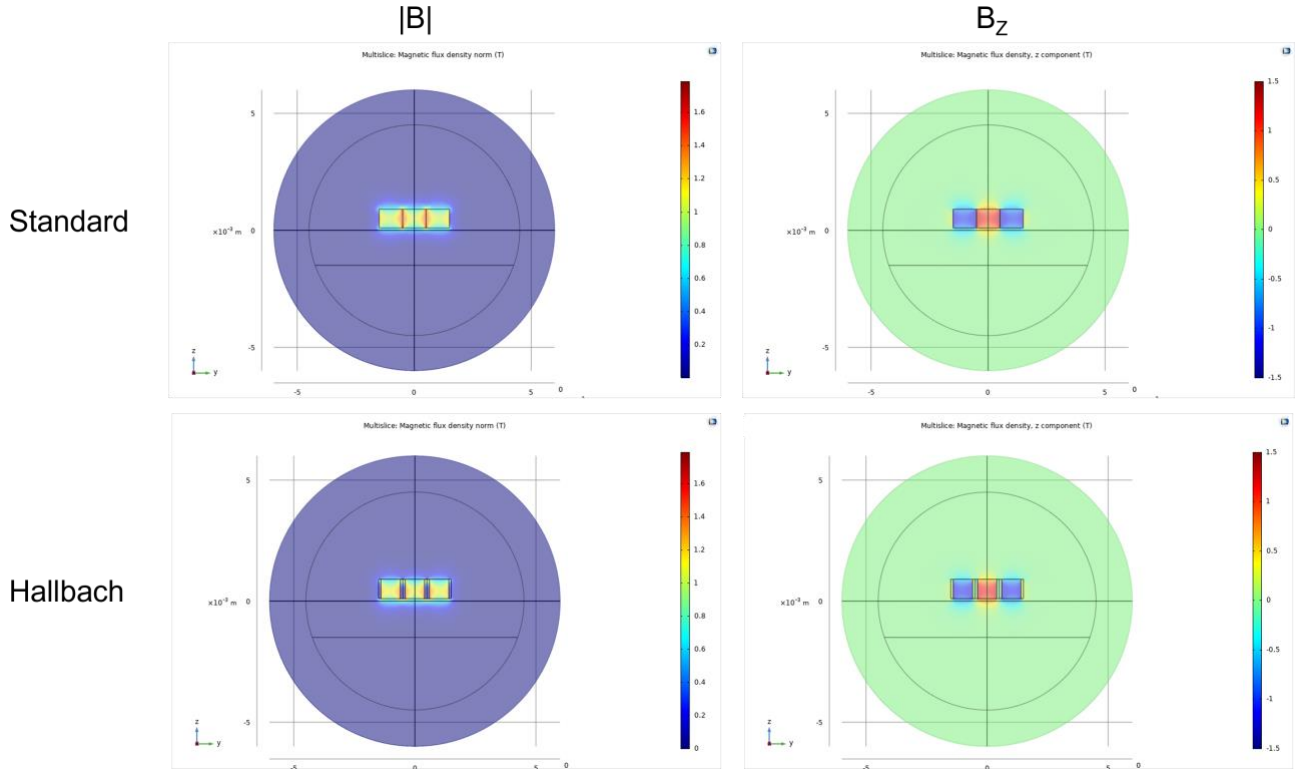


Fig. 3.4: Magnet Array Configurations – Standard (Checkerboard) magnet array (top row) vs. Hallbach magnet array (bottom row). Finite element simulation results for  $|B|$  and  $B_z$  are shown for each magnet array type.

configuration, the field is concentrated underneath the magnet array, thus resulting in a larger magnetic field and subsequently a larger levitation force. In Section 3.1.1, we analyze and compare the various lunar payload capacities that these two magnet array geometries can achieve, assuming anisotropic graphite  $\chi_{x,graphite} = 1.36 \times 10^{-5}$ ,  $\chi_{y,graphite} = 1.36 \times 10^{-5}$ ,  $\chi_{z,graphite} = 60 \times 10^{-5}$  [55].

### 3.1.1 Lunar Payload versus Magnet Geometry and Graphite Thickness

Figure 3.5 shows the lunar payload capacities (i.e. mass in addition to the magnet array's mass) as a function of levitation gap. We examined various magnet types (standard vs Hallbach), magnet widths (1, 1.4 mm), magnet thickness (0.4 and 0.8 mm) and graphite thicknesses (100, 250, 500, 1000, 2000  $\mu m$ ) in our design space analysis. These initial design parameters were chosen to be similar to parameters that have been used in our micro-robotic levitation systems and have experimentally been demonstrated to self-levitate on Earth.

In Figure 3.5, we computed the levitation force as a function of levitation gap; however to plot it in terms more relevant

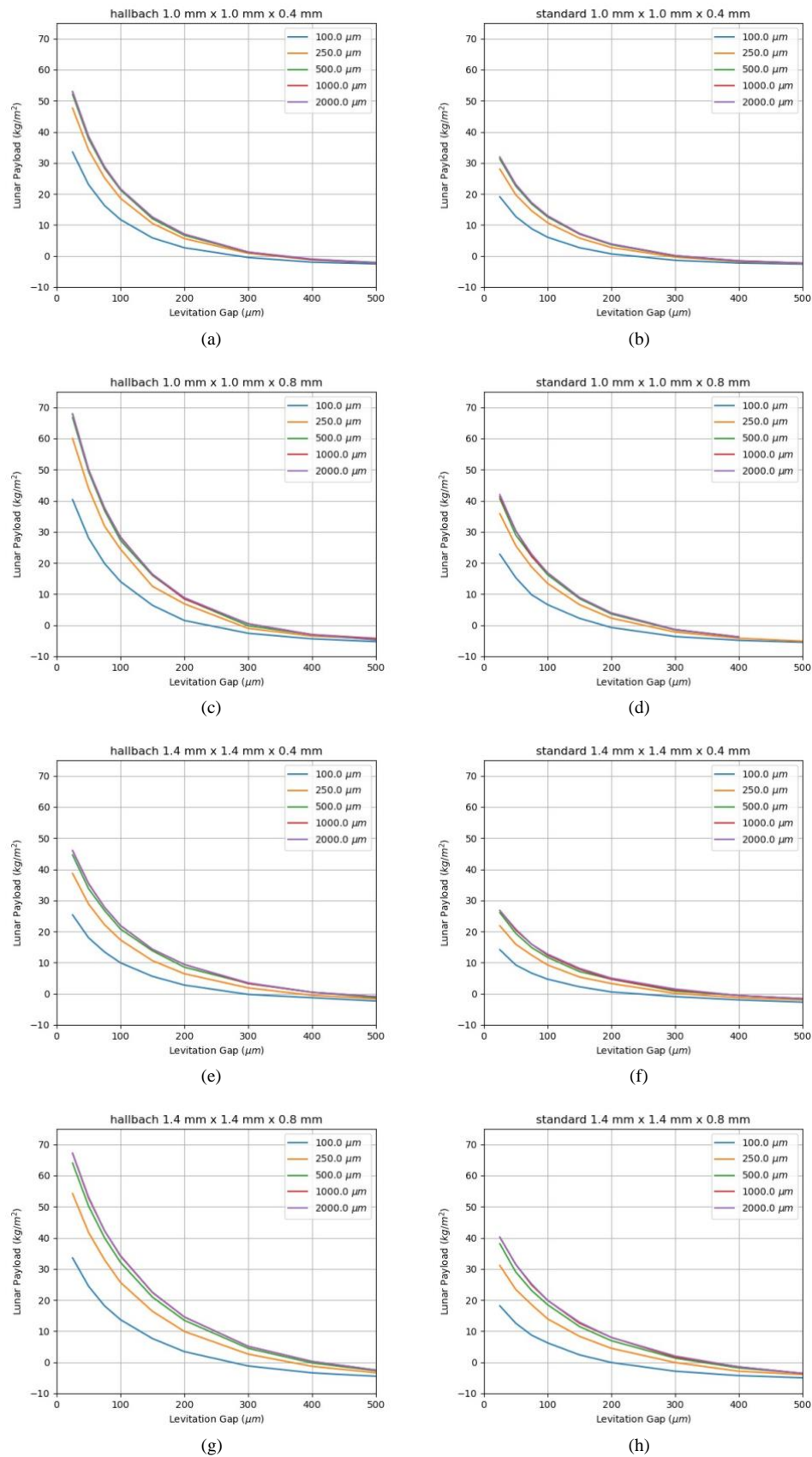


Fig. 3.5: Lunar Levitation Payload for various magnet arrays, magnet geometries, and graphite thicknesses.

for system design parameters, we instead plot the Lunar Payload normalized by Robot Area, as shown in Eq. 3.10:

$$\frac{F_{levitate}}{A_{array}} = \frac{g_{lunar}(m_{array} + m_{payload})}{A_{array}} \quad (3.10)$$

$$\frac{m_{payload}}{A_{array}} = \frac{F_{levitate} - g_{lunar}m_{array}}{g_{lunar}A_{array}} \quad (3.11)$$

Where  $A_{array}$  is the area of the magnet array,  $g_{lunar}$  is the gravitational constant of the moon,  $m_{array}$  is the mass of the magnet array, and  $m_{payload}$  is the mass of the payload.

Figure 3.5 shows as expected the increased lunar payload capacity that one can achieve with a Hallbach array over a standard array. In addition, the levitation forces eventually saturate after a given graphite thickness, which can be seen in Eq. 3.9 since the maximum force occurs when  $B_{z,bot}^2 = 0$ . Therefore the maximum levitation force for a given graphite thickness is determined by the trade off between the maximum surface normal magnetic flux (which is proportional to the magnetic volume) and the decay of the surface magnetic flux from the surface of the magnet (which is inversely proportional to the magnetic volume). Therefore, for a given graphite thickness, there exists an optimal thickness of magnet that maximizes the total levitation force. Also note that the maximum levitation force achievable with current modern technology is related to the maximum surface magnetic flux density which is a fundamental material property of NdFeB.

To better emphasize the trade-off between magnet geometry, we plot in Figure 3.6 the lunar payload capacity for a fixed graphite thickness for all of the various input design parameters. The Hallbach arrays all show improved performance compared to the standard magnet array configuration achieving  $\sim 30 \text{ kg/m}^2$  at  $\sim 100 \mu\text{m}$  levitation gap for  $h_{mag} = 0.8 \text{ mm}$ .

Figure 3.7 illustrates the trade-offs that occur as a function of magnet thickness. As the magnet thickness increases, the volume of magnetic material that can contribute to the magnetic flux density at the surface next to the graphite eventually decreases, thus resulting in diminishing returns as it contributes to excess mass without an increase in levitation force. This is visualized in Figure 3.7b where we plot the ratio between lunar payload and robot mass. However, for thicker magnets there exists a trade-off between mass transport efficiency and levitation gap (Fig. 3.6 and 3.7b)

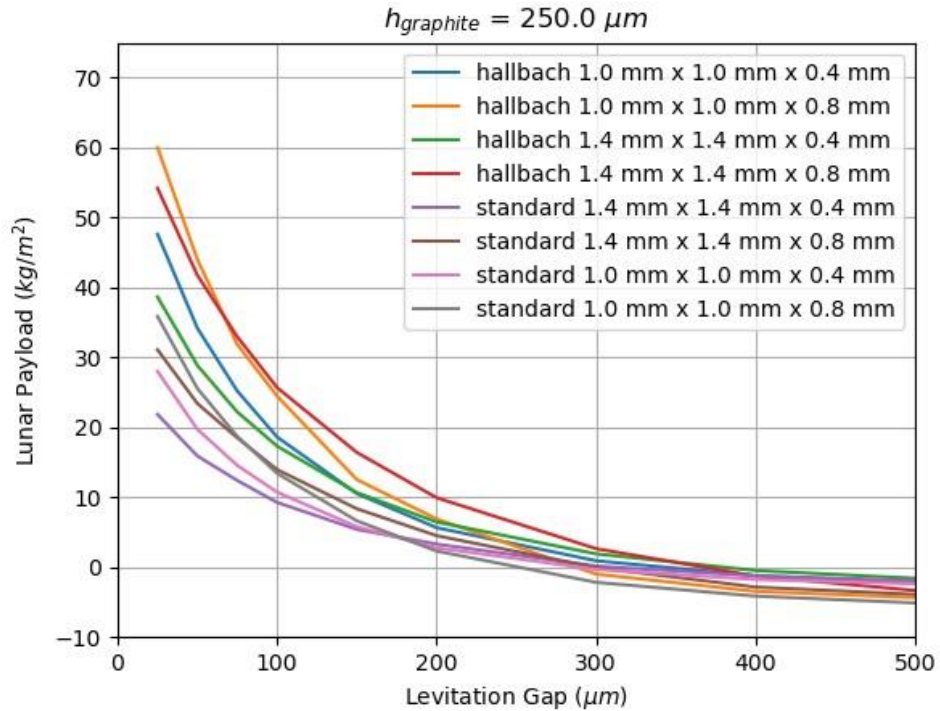


Fig. 3.6: Lunar Payload for Various Magnet Geometries for a Fixed Levitation Gap and Graphite Thickness

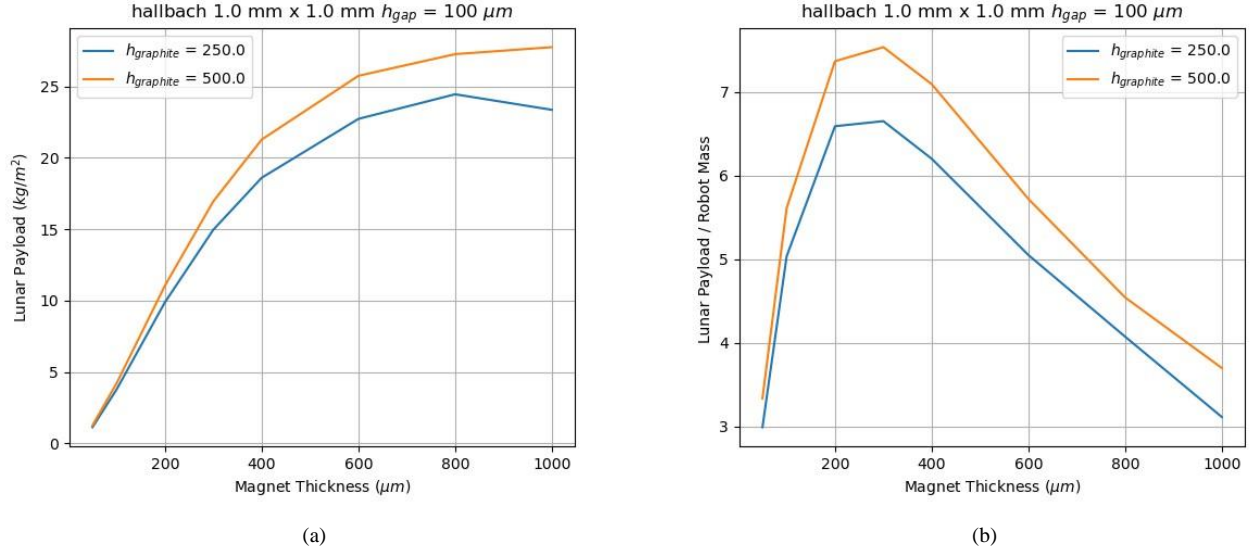


Fig. 3.7: Lunar Levitation Payload for Varying Magnet Thicknesses of a Hallbach Array, (a) Lunar Payload vs Magnet Thickness, (b) Lunar Payload (normalized by Robot Mass) vs Magnet Thickness. Magnet thickness of  $\sim 800 \mu\text{m}$  provides greatest payload capacity, while magnet thickness of  $\sim 300 \mu\text{m}$  provides optimal efficiency of robot mass vs. payload capacity.

### 3.1.2 Out-of-Plane Curvature Analysis

Given the levitation forces on the robot, we can also compute the effects of curvature on the robots assuming a weighted force as a function of graphite curvature. As shown in Figure 3.5, the diamagnetic force falls off quite rapidly as a function of distance to the graphite. Therefore, assuming a monolithic rigid robot, as the curvature increases (assuming the robot is flat to the surface) the robot, on average, moves further away from the graphite and consequently the levitation force also drops off. We simulated two types of configurations shown in Figure 3.8: (1) smoothly varying and (2) a triangle. (2) represents the situation where a certain curvature can be approximated using flat graphite plates. We simulated positive curvature to better sweep the effects of curvature, understandably the negative curvature is limited primarily by geometry of the robot, which as we will discuss later is a primary reason for us to investigate compliant and flexible robots.

As expected, for a rigid robot the maximum curvature is mainly limited by the separation distance between the magnets and the graphite at far ends of the robot, which means geometrically monolithic rigid robots cannot tolerate much out of plane curvature.

Therefore, to improve the robot's ability to handle out-of-plane curvature in the track we developed a finite-element model to simulated articulated or composite robots that are able to conform to the track geometry. The model discretizes the robot into a set of point masses, which are constrained to move only in the y-direction (up-down). The point masses interact via spring forces between them. The springs are defined by the effective spring constants of a cantilever beam connecting two neighboring points, as defined by the following equation:

$$k = \frac{3EI}{L^3} \quad (3.12)$$

Where,

$E$  = Modulus of Elasticity ( $\text{N/m}^2$ )

$I$  = Moment of Inertia ( $\text{m}^4$ )

$L$  = Distance between point masses ( $\text{m}$ )

The robot is comprised of two types of point masses, representing the magnets and the film flexures. The magnetic points are modeled as NdFeB elements (400-800  $\mu\text{m}$  thick, 41 GPa modulus of elasticity, 7000  $\text{kg/m}^3$  density) that interact with the track via diamagnetic levitation forces, which are modeled using the results of the lunar payload simulation discussed in Section 3.1.1.

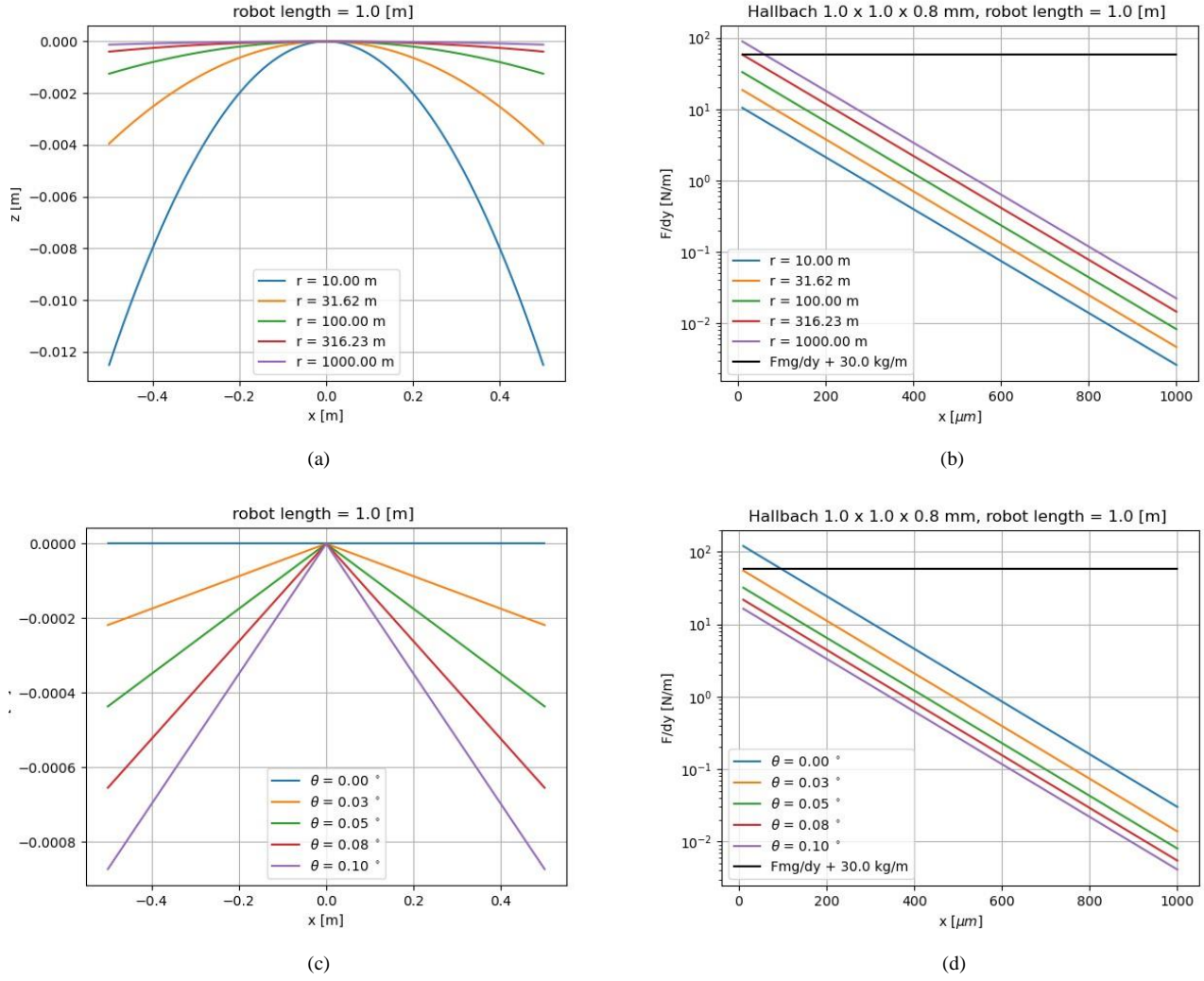


Fig. 3.8: Levitation Gap vs. Out-of-Plane Curvature, for a rigid robot. Right column plots the actual curvature shape, while the left column plots the force, with the black horizontal line representing the required force to self-levitate on the moon

The flexure points are modeled as stainless steel elements ( $6 \mu\text{m}$  thick, 193 GPa modulus of elasticity,  $7990 \text{ kg/m}^3$  density) that do not experience magnetic forces and serve exclusively to add compliance to the system. The model iteratively solves the acceleration of each particle using the following equation:

$$a_{n,t+1} = -g + \frac{F_{mag}A_{element}}{m_n} + \frac{k_n}{m_n} \left( \frac{y_{n+1} + y_{n-1} - 2y_n}{2} \right) - \frac{b}{m_n} v_{n,t} \quad (3.13)$$

Where,

$g$  = Acceleration due to gravity on the moon ( $\text{m/s}^2$ )

$F_{mag}$  = Force per unit area on the point mass ( $\text{N/m}^2$ )

$A_{element}$  = Discretized area of the point mass ( $\text{m}^2$ )

$m_n$  = Mass of the  $n^{\text{th}}$  point mass ( $\text{kg}$ )

$k_n$  = Equivalent stiffness at the  $n^{\text{th}}$  node ( $\text{N/m}$ )

$y_n$  = Position of the  $n^{\text{th}}$  point mass ( $\text{m}$ )

$v_n$  = Velocity of the  $n^{\text{th}}$  point mass ( $\text{m/s}$ )

$b$  = Damping constant ( $\text{Ns/m}$ )



The velocity and position of each point mass is iteratively updated until the acceleration of each point converges. The update equations are as follows:

$$v_{n,t+1} = v_{n,t} + a_{n,t+1}dt \quad (3.14)$$

$$y_{n,t+1} = y_{n,t} + v_{n,t+1}dt \quad (3.15)$$

The model allows for different configurations of the robot to be tested. The payload mass, number of magnets, and the ratio of magnet size to flexure size can be adjusted. Additionally, the radius of curvature and hill height / crater depth can be modified. The model outputs an image of what the robot looks like over the curved section of track as well as the minimum levitation gap for that case. Examples are shown in Fig. 3.9.

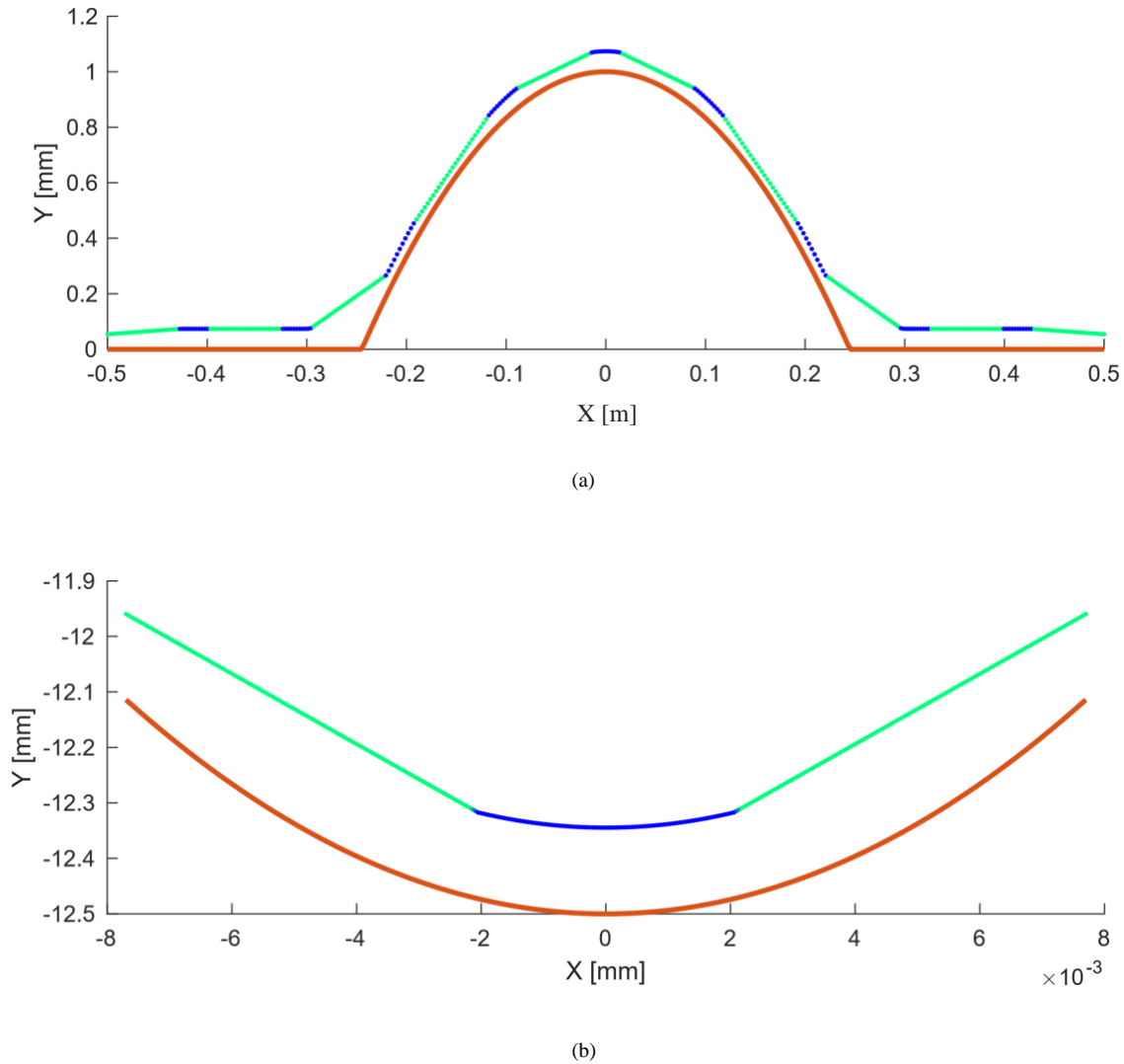


Fig. 3.9: Simulated Compliant Robots with Flexures. Green sections represent rigid magnet elements; blue sections represent compliant flexures; The solid orange line represents the flexible track. (a) Shows a 1 m x 1 m robot with 10 magnet sections that comprise 72.5% of the robot. The robot is levitating on the Moon, over a hill with a radius of 30m and a height of 1mm, and is loaded with 30kg of payload mass. The minimum levitation gap in this case is 49  $\mu\text{m}$ . The scale of the y-axis is in mm to make the compliance more clear. (b) Shows a recreation of an experiment (Sec. 4.4) we carried out on Earth, on a compliant robot made up of 4 magnet arrays linked with flexures in a 2 x 2 square configuration. The robot is levitating in a bowl with a radius of curvature of 7.5 cm and a depth of 1.25 cm. The minimum levitation gap in this case is 154  $\mu\text{m}$ .

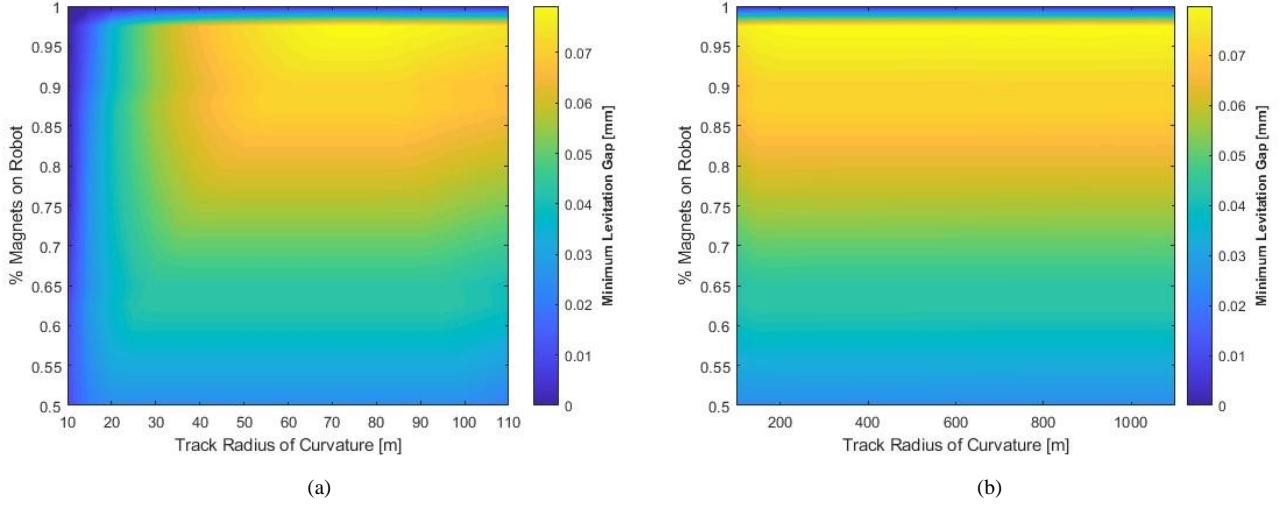


Fig. 3.10: Design Space for Compliant Robots. Relationship that the track's out-of-plane radius of curvature and the ratio of magnet size to flexure size has on the minimum levitation gap of the robot. (a) Shows the relationship for track radii between 10m and 100m. (b) Shows the relationship for track radii between 100m and 1100m.

Using this model we were able to understand the relationship between the radius of curvature, the ratio of magnet to flexures, and the minimum levitation gap. These results can be seen in Fig. 3.10. The results show that it may not be possible for the robot to avoid bottoming out on the track for out-of-plane radii of curvature  $\leq 25$  m and the robot should be made up of  $\geq 70\%$  and  $< 100\%$  magnets, and optimally around 90-95% magnets. The levitation gap remains constant for a single configuration once the radius of curvature is  $> 100$  m. These results also show that compliant features in the robots are necessary to handle out-of-plane curvature in the track, but that flexures add mass (without generating levitation force) and thus reduce levitation gap if they make up an excessive percentage of the total robot. As shown in Fig. 3.10, when the magnets make up 100% of the track, the robot bottoms out on the track.

### 3.2 Electromagnetic Drive Analysis

The electromagnetic forces used to drive the robots results from using a serpentine trace that generates a travelling magnetic field that the magnets in the magnet array essentially "surf" on.

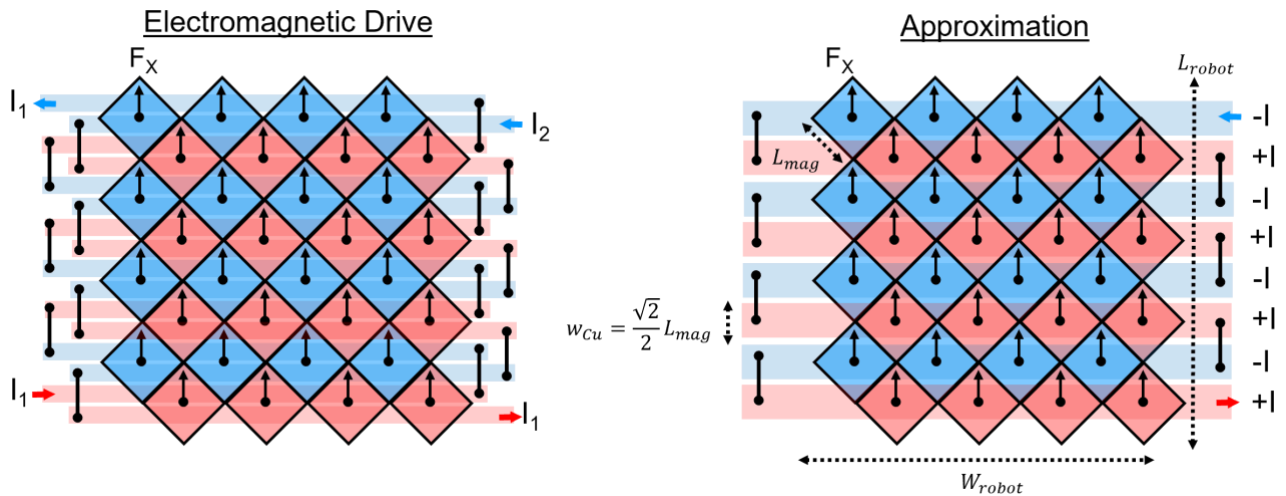


Fig. 3.11: Diagram of Electromagnetic Drive



Figure 3.11 shows the basic concept of the electromagnetic propulsion for a single layer. Two control currents ( $I_1$  and  $I_2$ ) are driven in quadrature to generate a travelling magnetic wave. More details can be found in [53], [54], [60]. For analysis purposes, we can look at Figure 3.11 and simplify the situation by consolidating the two wires flowing in the same direction into a single wire to provide a simpler analytical expressions for analysis. To generate forces or control in the orthogonal direction, the same traces are rotated by 90 degrees to this trace pattern.

### 3.2.1 Equations of Motion

Here, we focus on the electromagnetic interaction between the magnet and the track's coils / traces. Since the graphite's magnetic susceptibility is relatively small, we can ignore the interaction between the coils and the graphite. Through superposition, we can combine the levitation results from earlier with the electromagnetic drive analysis in this section. In addition, we can compute the force on a single magnet and then scale the forces by the number of magnets since the forces on the total magnet array scale linearly with number of magnets.

Fig. 3.12 and Eq. 3.16-3.19 describe the magnet-wire interaction physics, assuming an infinite wire (in y-axis):

$$m_D = \frac{B_r V}{\mu_0} \quad (3.16)$$

$$F_X = m_D \frac{\mu_0 I}{2\pi} \frac{z^2 - x^2}{(x^2 + z^2)^2} \quad (3.17)$$

$$F_Z = m_D \frac{\mu_0 I}{2\pi} \frac{-2zx}{(x^2 + z^2)^2} \quad (3.18)$$

$$P = \rho_{Cu} \frac{L}{\sigma_{Area}} I^2 \quad (3.19)$$

where  $m_D$  is the magnetic dipole for a single magnet in the array,  $V$  is the volume of the single magnet,  $\mu_0$  is the vacuum permeability ( $1.256 \times 10^{-6} \text{ N/A}^2$ ),  $I$  is the current in the wire,  $\rho_{Cu}$  is the resistivity of Copper ( $1.68 \times 10^{-8} \Omega m$ ),  $\sigma_{Area}$  is the copper cross sectional area, and  $L$  is the length of the wire in the y-axis. From Equation 3.17, the maximum lateral force on the magnet occurs when the magnet is directly above the wire. Equations 3.17 and 3.18 assume the magnet is a point dipole which is an approximation since the magnet has some finite geometry and is a distributed point dipole. However, this we find from comparison with finite element simulations is a reasonable approximation.

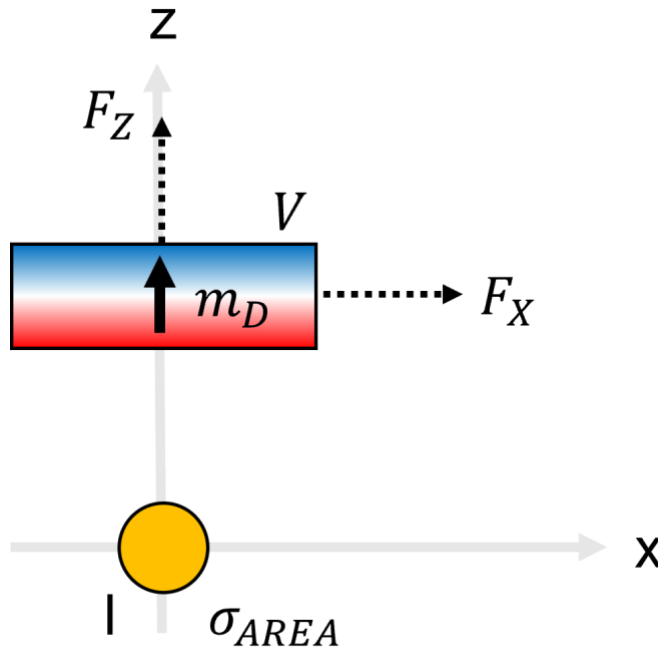


Fig. 3.12: Electromagnetic Force and Interaction

### 3.2.2 Force Analysis

The above equations apply for a single magnet, since the forces on the magnet add by superposition, the total forces for the magnet array (forming a robot) are expressed as the following:

$$V_{mag} = h_{mag} L_{mag}^2 \quad (3.20)$$

$$A_{mag} = L_{mag} W_{mag} = L_{mag}^2 \quad (3.21)$$

$$A_{robot} = L_{robot} W_{robot} \quad (3.22)$$

$$N_x = \frac{W_{robot}}{\frac{\sqrt{2}}{2} L_{mag}} \quad (3.23)$$

$$N_y = \frac{L_{robot}}{\frac{\sqrt{2}}{2} L_{mag}} \quad (3.24)$$

$$m_{robot} = \rho_{NdFeB} V_{mag} N_x N_y \quad (3.25)$$

$$F_{X,tot} = N_{mag} F_X \quad (3.26)$$

$$P_{track} = 2\rho_{Cu} \frac{W_{track} L_{robot}}{t_{Cu} L_{mag}^2} I^2 \quad (3.27)$$

$$P_{Area} = P_{track} / A_{robot} \quad (3.28)$$

$$P_{Mass} = P_{track} / m_{total} \quad (3.29)$$

Where  $V_{mag}$  is the volume of the individual magnet,  $L_{mag}$  is the length of an individual magnet,  $A_{mag}$  is the area of the individual magnet,  $A_{robot}$  is the area of the entire robot,  $L_{robot}$  and  $W_{robot}$  are the length and width of the robot respectively,  $N_x$  and  $N_y$  are the

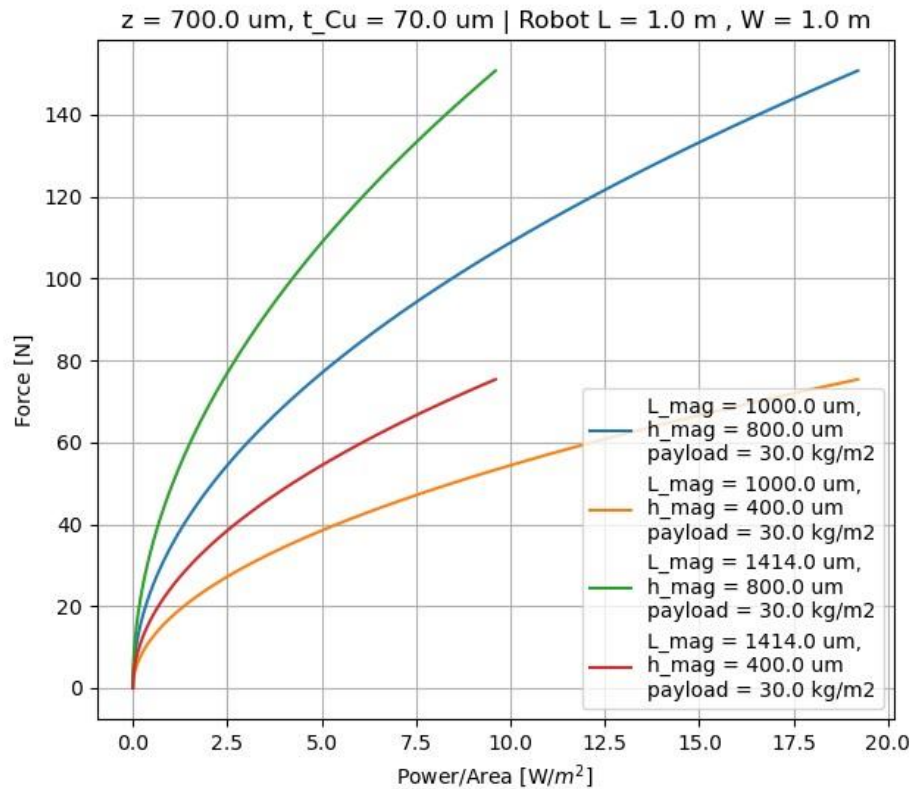


Fig. 3.13: Electromagnetic Force vs Area Power Density, assuming  $t_{Cu} = 70 \mu m$  which corresponds to 2 oz copper and the separation between the magnet dipole and the trace is  $700 \mu m$ , which is  $\sim 50 - 100 \mu m$  levitation gap

number of magnets in the X and Y direction,  $\rho_{NdFeB}$  is the density of NdFeB (7.5g/cc),  $W_{track}$  is the width of the track,  $t_{Cu}$  is the thickness of a copper trace,  $P_{Area}$  is the power per unit area, and  $P_{Mass}$  is the power per mass of robot and payload. For analysis purposes, we assume that with closed loop control, one can maintain the position of the magnet relative to the traces (as done in past work [53], [60]) to enable maximum efficiency of force applied to the magnet.

Figure 3.13 shows the amount of force as a function of area power density applied to 1 m<sup>2</sup> robots carrying 30 kg/m<sup>2</sup> payloads with different magnet configurations (described by  $L_{mag}$ ,  $h_{mag}$ ), where we also have assumed 2 mil copper traces ( $\sim 70\mu m$ ) and a z separation of  $700\mu m$  between the wires buried in the track and the robots levitating over the graphite.

As expected from Equations 3.17 and 3.27, there is a square-root dependence between force and power. In addition, by using larger volume magnets, greater forces can be achieved for a given power as represented by Equations 3.16, 3.17, 3.20, and 3.27, since the larger magnetic dipole scales with volume of magnet as well as larger magnets also require fewer traces, resulting in a lower resistance per unit area.

These trends also parallel our levitation analysis; therefore, one of the limiting factors determining the ideal size and shape of the individual magnets ends up being the desired graphite thickness and bending stiffness of the entire track.

### 3.2.3 Incline Analysis

Figure 3.14 shows the free body diagram for analyzing the lateral forces that a robot can experience while on an inclined (non-flat) track. In an inclined-track scenario, the electromagnetic forces generated by the traces must offset the gravity weight of the robot and payload even when the robot is static (consuming non-trivial electrical power), where as for a flat-track scenario almost negligible power must be provided to maintain static position of the robot.

$$F_{mg} = m_{robot} g_{lunar} \quad (3.30)$$

$$F_{X,tot} = F_{mg} \sin(\theta) \quad (3.31)$$

Where  $g_{lunar}$  is the gravitational constant of the moon, and  $\theta$  is the angle of incline.

Figure 3.15 shows the amount of Power per Area as well as Power per Total Mass for various robot configurations with a 30 kg/m<sup>2</sup> payload. If larger power is tolerated, eventually the electromagnetic drive is able to support a complete vertical operation, which is shown by the divergence in the maximum incline as it approaches vertical. However assuming  $<5 \text{ W/m}^2$ , a FLOAT robot can easily achieve controlled mobility on up to 40-45° inclines.

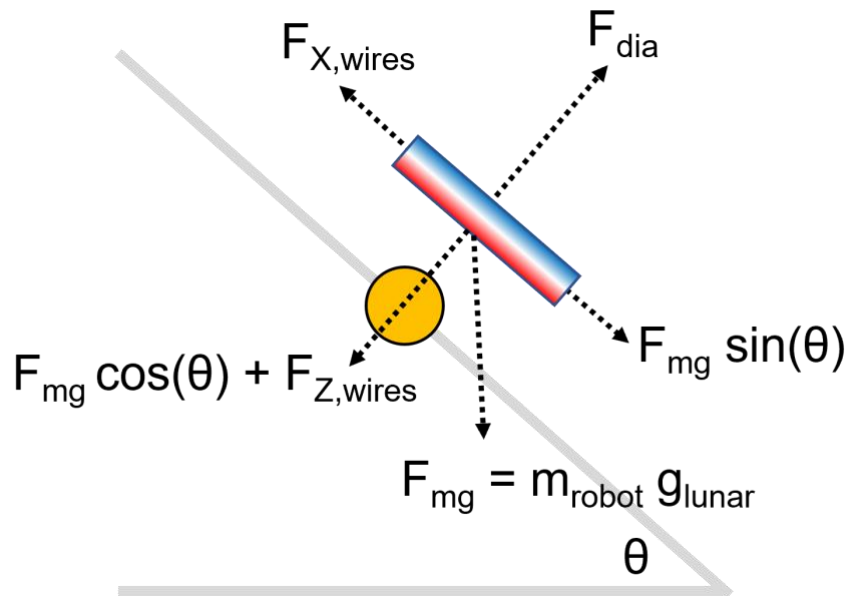
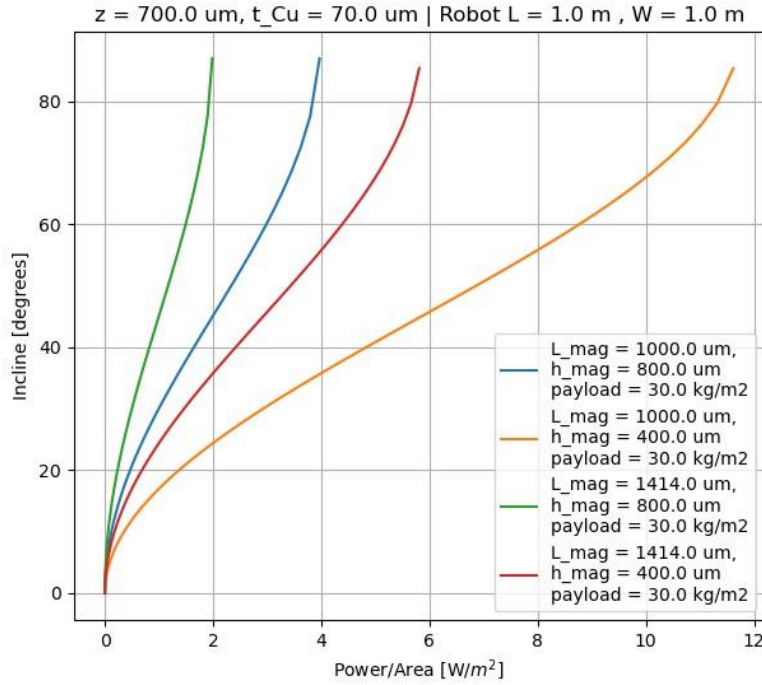
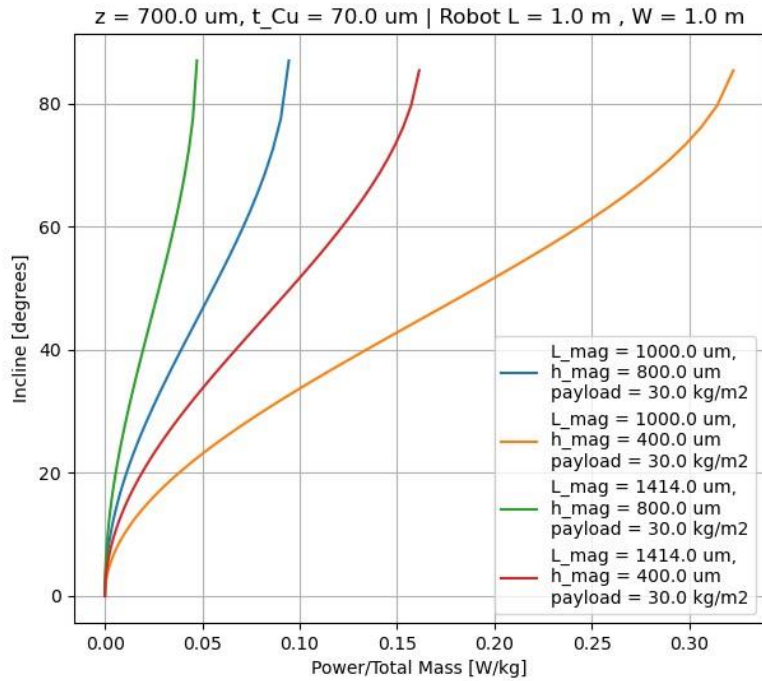


Fig. 3.14: Diagram of Incline



(a)



(b)

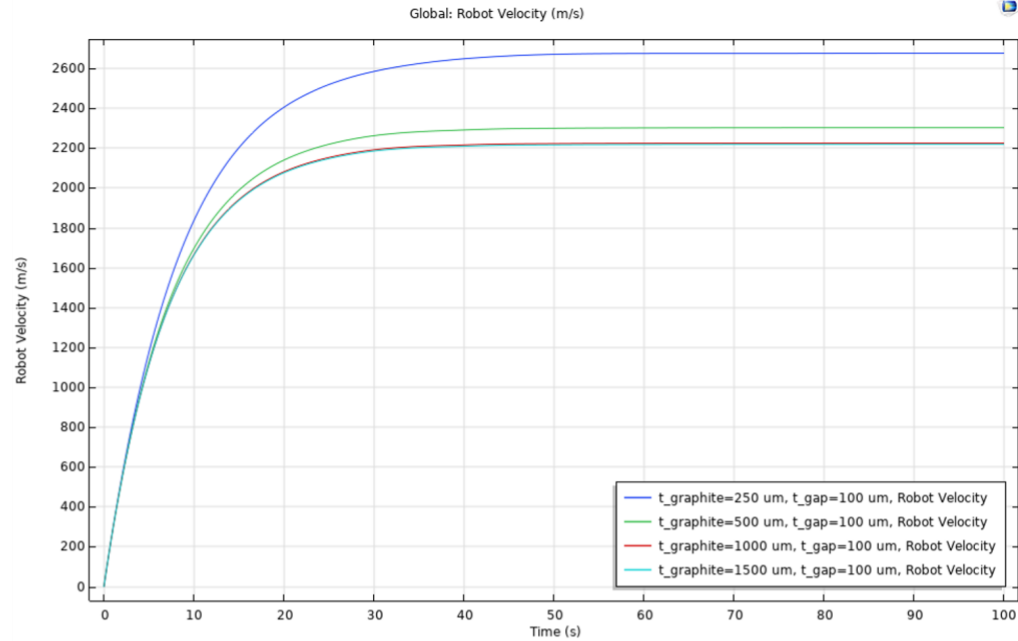
Fig. 3.15: Incline Analysis: (a) Incline vs Power/Area, (b) Incline vs Power/Total Mass, for  $1 \text{ m}^2$  area robots with various individual magnet geometries ( $L_{\text{mag}} = 1\text{-}1.41 \text{ mm}$ ,  $h_{\text{mag}} = 0.4\text{-}0.8 \text{ mm}$ ). With sufficient power, robots are able to be controllably-propelled up / down inclines of any angle (up to vertical), and use  $<5 \text{ W}/\text{m}^2$  for inclines  $<40\text{-}45^\circ$  for all tested magnet configurations.

### 3.2.4 Velocity Analysis

On the Moon, potentially very high robots speeds are possible with FLOAT, since the robot moves ballistically over straight segments of track and experiences few sources of drag (as illustrated in Fig. 3.16). On Earth, air drag and Eddy current drag are the two dominant drag terms that limit the maximum velocity of the levitated platform. In a lunar environment, we can easily ignore fluid or air drag effects, however eddy current drag terms can still exist. This drag term is due to the Lorentz force generated by the rapidly changing magnetic field induced in any conductive objects, although typically this is only relevant within a couple of hundred of microns away from the magnet surface.

Eddy currents are quite difficult to solve completely analytically; therefore, we use COMSOL to compute the Lorentz force

Standard



Hallbach

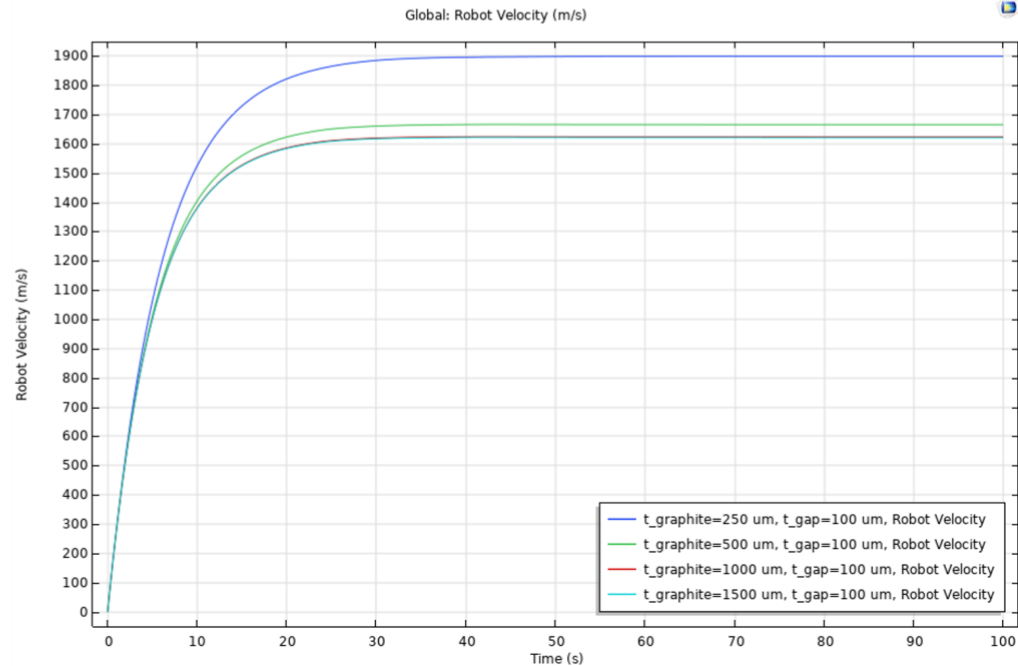


Fig. 3.16: Robot Max Velocity due to the effect of graphite thickness on Eddy current drag, for a Standard array type magnetic robot (top) and Hallbach array type robot (bottom). For each configuration,  $F = 0.1$  N for a  $9 \text{ mm}^2$  robot composed of  $1 \text{ mm} \times 1 \text{ mm} \times 0.8 \text{ mm}$  magnets with a  $30 \text{ kg/m}^2$  payload assuming a  $100 \text{ }\mu\text{m}$  levitation gap,  $\sigma_x, \sigma_y = 2.5\text{e}5 \text{ S/m}$ ,  $\sigma_z = 3.3\text{e}2 \text{ S/m}$  on the

magnet and then solve the rigid body differential equation to compute the robot's net velocity, as defined in the following equations:

$$m_{tot} = m_{robot} + m_{payload} \quad (3.32)$$

$$F_{X,tot} = m_{tot} \frac{dv}{dt} + F_{drag} \quad (3.33)$$

$$F_{drag} = \gamma_{eddy} v \quad (3.34)$$

$$v(t) = \frac{F_{X,tot}}{\gamma_{eddy}} \left[ 1 - \exp \left[ -\frac{\gamma_{eddy}}{m_{tot}} t \right] \right] \quad (3.35)$$

$$x(t) = \frac{F_{X,tot}}{\gamma_{eddy}} t + \frac{m F_{X,tot}}{\gamma^2} \left[ \exp \left[ -\frac{\gamma_{eddy}}{m_{tot}} t \right] - 1 \right] \quad (3.36)$$

Where,  $F_{drag}$  is the drag force,  $\gamma_{eddy}$  is the eddy current drag term. From Eq. 3.35, the maximum velocity ( $v_{max}$ ) achievable is  $F_{X,tot}/\gamma_{eddy}$ ; however both the force and drag both scale with area so  $v_{max}$  independent of the robot dimensions. Likewise the time constant to achieve the maximum velocity is  $m_{tot}/\gamma_{eddy}$ , which is independent of the applied force.

In Figure 3.16, we compute the maximum velocity for a robot assuming a constant force applied (0.1 N) for various thicknesses of graphite. Previously, we had only considered the anisotropy of the magnetic susceptibility when computing the levitation forces from the graphite. Because we are examining the Eddy currents from graphite, we also include in this simulation the anisotropic electrical conductivity of graphite ( $\sigma_x = 2.5e5$  S/m,  $\sigma_y = 2.5e5$  S/m,  $\sigma_z = 3.3e2$  S/m) [61].

Figure 3.16 shows there is less eddy current drag for thin graphite than thick graphite since less of the field is overlapping with the graphite; however, after a certain thickness of graphite most of the surface field of the magnet is encapsulated by the graphite. Therefore, materials more than  $> 1000\mu m$  have negligible effect on the eddy current drag since the magnetic field from the magnet array has attenuated from the surface. Figure 3.16 also compares the effect of a standard configuration versus that of a Hallbach array. Since the Hallbach array has an increased magnetic field underneath the magnet, the eddy current and drag terms are also proportionally larger, resulting in increased drag. The  $v_{max}$  for the standard and Hallbach array are  $\sim 2700m/s$  and  $\sim 1900m/s$ , which correspond to  $\gamma_{eddy}$  of  $3.7 \times 10^{-5}$  and  $5.3 \times 10^{-5}$  respectively. While we have assumed standard pyrolytic graphite, this drag term can also be further engineered through standard lamination techniques commonly found in ferrites to reduce eddy currents.

It should also be noted that achieving the maximum speeds calculated in this simulation would require a perfectly flat track (with no debris), and well-timed energization of track traces to generate the correct electromagnetic force as the robot passes overhead. Additionally, the escape velocity on the surface of the Moon is 2.38 km/s, which means that certain calculated velocities would actually exceed the Moon's escape velocity.

### 3.2.5 In-Plane Curvature Analysis

To analyze in-plane curvature (i.e. radius of curvature for turns in the track), we use the equation for centripetal motion (Eq. 3.37), where  $F_Y$  can be taken from Eq. 3.17, and where  $z$  is just adjusted for the slightly larger separation for the orthogonal layer of traces oriented to provide lateral confinement as opposed to direct electromagnetic thrust along the direction of the track. This allows us to can compute the design trade space between the minimum achievable radius of curvature, the maximum velocity at which the robot can still be electromagnetically confined on the tracks, and the electrical power required to achieve this force balance:

$$F_{Y,tot} = \frac{m_{total} v^2}{r_{max}} \quad (3.37)$$

Figure 3.17 shows the various powers required to confine a magnet array moving at various velocities and radii according to Equation 3.37. For nominal operation of a 1 m<sup>2</sup> robot at 0.5 m/s velocity,  $\sim 5$  m radius turns can be achieved for  $< 1$  W/m<sup>2</sup> power levels, for almost all magnet geometries simulated. Required power is also higher for more complicated track geometries (e.g. compound slopes, where the track simultaneously turns and is on an incline) and is not modeled here.



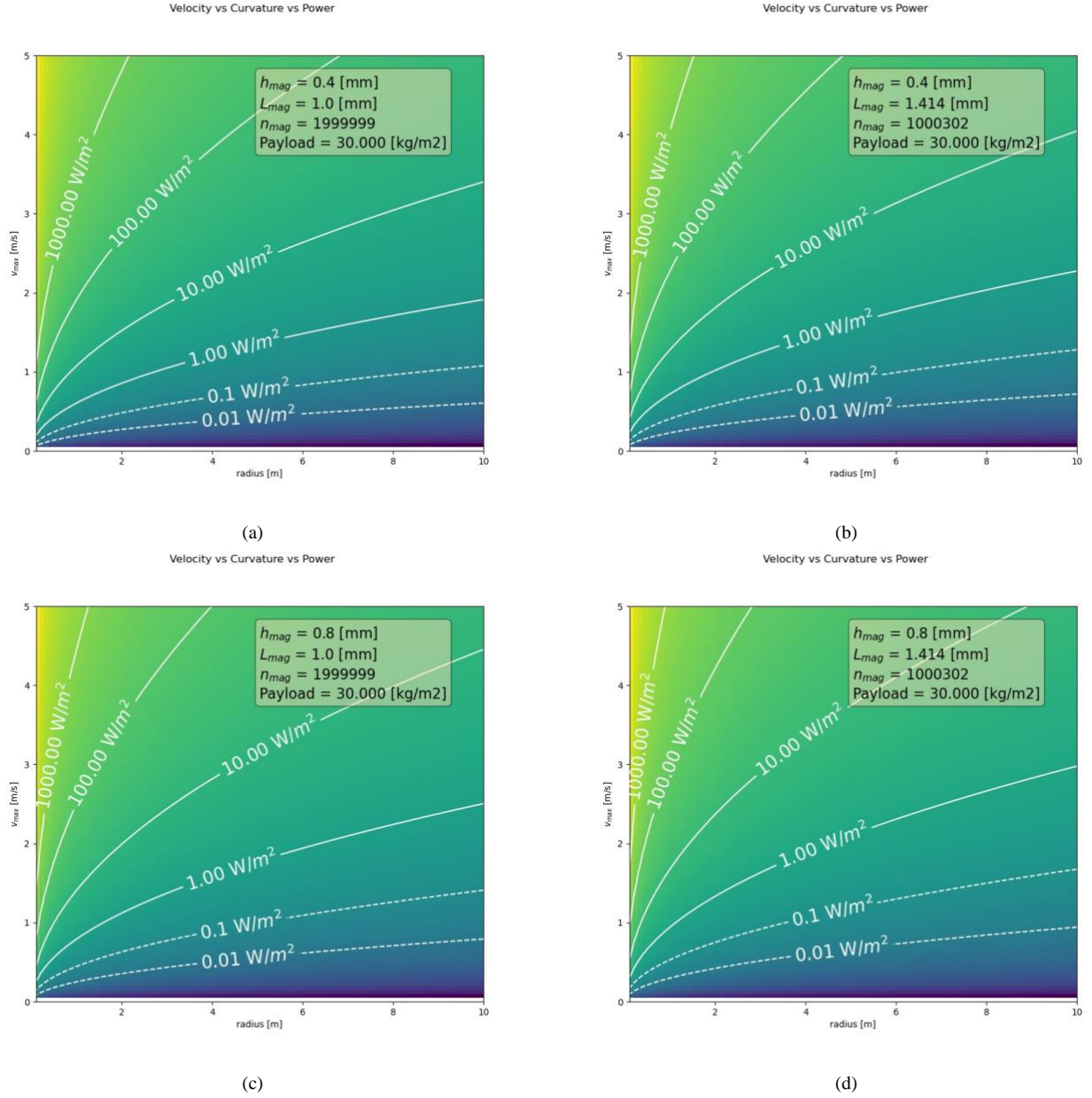


Fig. 3.17: Maximum Velocity vs. Turn Radius and Power for Various Magnet Geometries: (a)  $h_{mag} = 0.4mm, L_{mag} = 1.0mm$ , (b)  $h_{mag} = 0.4mm, L_{mag} = 1.414mm$ , (c)  $h_{mag} = 0.8mm, L_{mag} = 1.0mm$ , (d)  $h_{mag} = 0.8mm, L_{mag} = 1.414mm$

### 3.3 Magnetic Confinement Analysis

One potential concern / failure mode of the FLOAT system is what occurs when there is no power to the FLOAT track, since lateral (in-plane) confinement of the FLOAT robots is achieved using the electromagnetic forces generated by the track. Therefore, we also investigated a passive method of robot confinement within the lateral dimensions of the track using magnetic dipole-dipole interactions of permanent magnets.

#### 3.3.1 Magnetic Dipole-Dipole Confinement

Through Earnshaw's theorem, using only permanent magnets can not enable stable levitation in 3D; however, permanent magnets with constraints can provide stable 1D confinement. To compute the necessary confinement forces, we investigate, in two-dimensions, the force induced between two magnetic dipoles:

$$\mathbf{F}(\mathbf{r}, \mathbf{m}_1, \mathbf{m}_2) = \frac{3\mu_0}{4\pi r^5} \left[ (\mathbf{m}_1 \cdot \mathbf{r})\mathbf{m}_2 + (\mathbf{m}_2 \cdot \mathbf{r})\mathbf{m}_1 + (\mathbf{m}_1 \cdot \mathbf{m}_2)\mathbf{r} - \frac{5(\mathbf{m}_1 \cdot \mathbf{r})(\mathbf{m}_2 \cdot \mathbf{r})}{r^2} \mathbf{r} \right] \quad (3.38)$$



Where,

$\mathbf{m}_1$  = Magnetic Dipole Vector for Magnet 1

$\mathbf{m}_2$  = Magnetic Dipole Vector for Magnet 2

$\mathbf{r}$  = Position Vector between Magnet 1 and Magnet 2

$\mathbf{F}$  = Force Vector between Magnet 1 and Magnet 2

Figure 3.18 shows the attractive / repulsive forces  $F_x$  and  $F_z$  assuming both  $\mathbf{m}_1 = \mathbf{m}_2 = [0, 0, m_d]$ , where  $m_d$  is computed assuming a 1.4 x 1.4 x 0.4 mm magnet following Eq. 3.16. Figure 3.18 also has greyed out regions which correspond to keep out regions where instead of repulsion the magnets are attracted (snap-through condition). Therefore as long as physical barriers are placed in these regions to ensure the robots cannot enter into these positions, the dipoles should always repel one-another, ensuring the robot is passively confined.

The forces computed scale linearly with magnetic dipole, while the distances for a given force scale as  $1/r^4$ ; however,  $>10$  N of force can be exerted by these small magnets for confinement. As a point of comparison the gravitational force due to a 30 kg payload on the moon is equal to only  $\sim 50$  N.

Figure 3.19 shows a conceptual diagram of the track, where “confinement” magnets are placed along the edges of the robot’s magnet array and corresponding “bumper” magnets (plus a physical bumper for the “keep-out” zone) are placed along the edges of the track. Based on the simulation results, a series of only 5-10 individual “confinement” magnets attached at a small stand-off distance along the sides of the nominal FLOAT robot magnet array, along with larger or more tightly-spaced arrays of “bumper” magnets attached to the two edges of the track, would be sufficient for maintaining passive confinement of the FLOAT robot on the track. Likewise similar “confinement” magnets could also be used on the front / rear of each FLOAT robot, to generate repulsive forces between magnetic robots and ensure that the robots would repel one another (like bumper cars) if they are accidentally positioned too close together.

This illustrated configuration thus forms a magnetic “dove-tail” guide such that, as the robot drifts closer towards the edge of the track, the confinement magnets are pushed nearer to the bumper magnets and they will generate corresponding larger

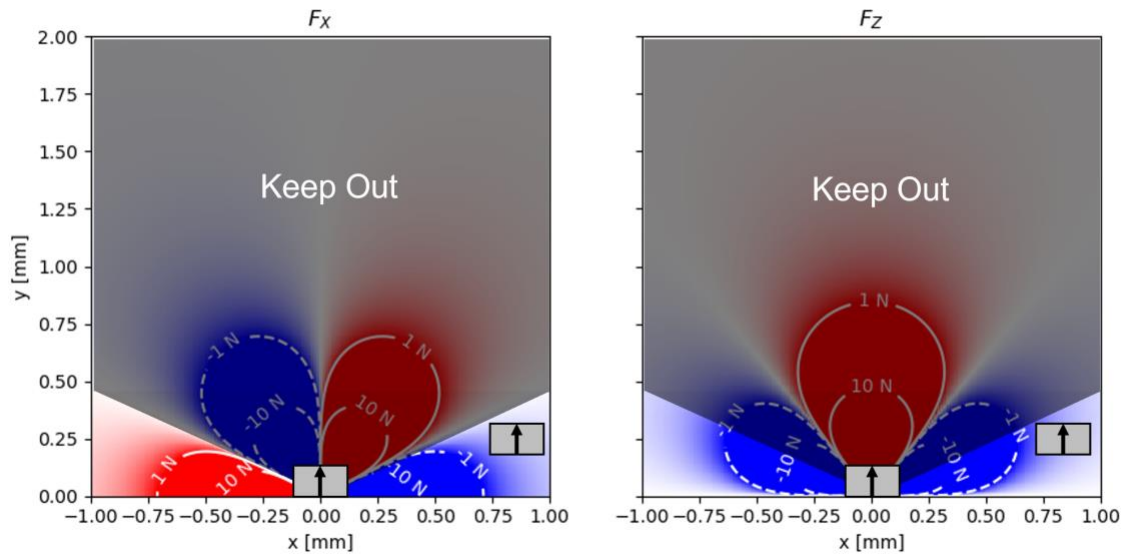


Fig. 3.18: Simulated magnetic dipole-dipole attractive (red) / repulsive (blue) forces, between a pair of 1.4 x 1.4 x 0.4 mm magnets (gray boxes, with arrows illustrating dipole direction).  $F_x$  force (left) and  $F_z$  force (right) are both plotted, as is a “keep-out” region (shaded) where the dipole-dipole magnetic force changes from a net repulsive force to a net attractive force, creating a pull-in instability.

repulsive forces that push the robot back towards the center of the track. By making the confinement and bumper magnets discrete, these elements do not affect the compliance of the track or robots for deployment, but can provide adequate coverage along the track. The confinement magnets on the robot (magnet array) can also be offset mechanically from the magnet array to avoid any unwanted interactions between the confinement magnets and the main magnet array.

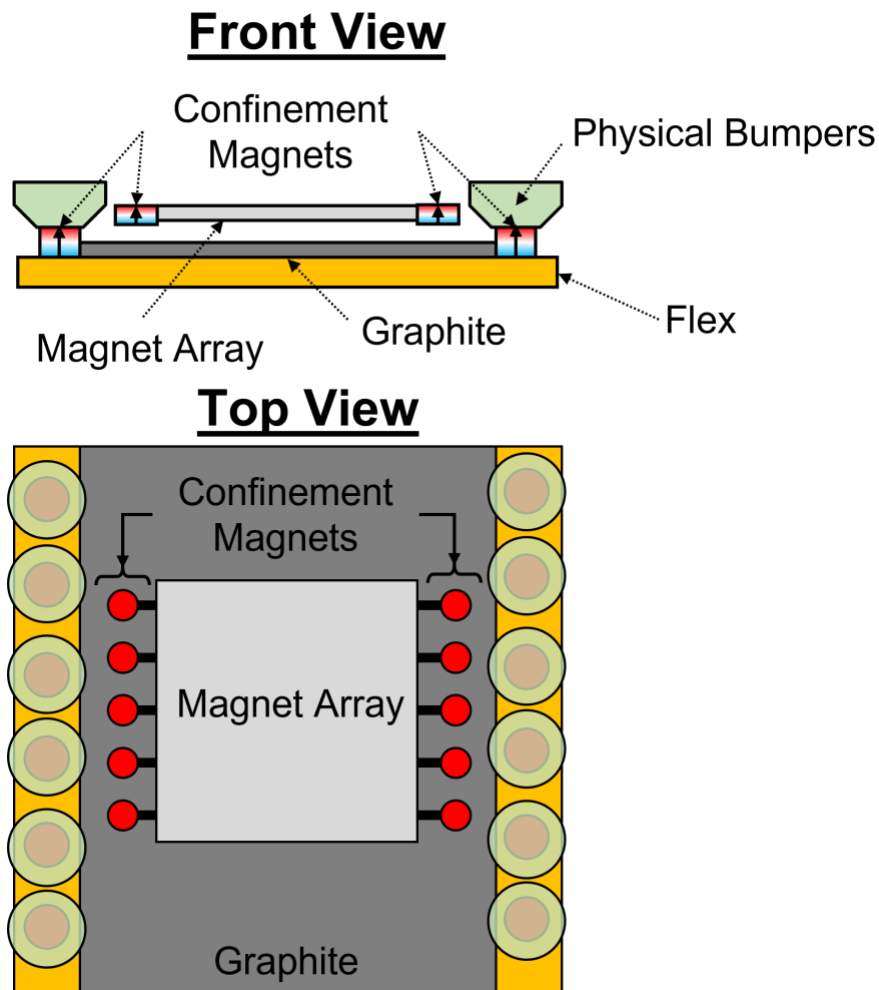


Fig. 3.19: Passive Magnetic Confinement Concept

## 4 EXPERIMENTS

Experimental work focused on 6 major risk areas for evaluating the feasibility of the FLOAT concept: (1) Scale up of the Magnet Array Sizes to  $10\text{ cm}^2$  (Sec. 4.1), (2) Effects of Dust and Abrasion (Sec. 4.2), (3) Life-Cycle Testing (Sec. 4.3), (4) Flexible and Compliant Robots (Sec. 4.4), (5) Magnetization and Repair of Magnets (Sec. 4.5), and (6) Vacuum Testing (Sec. 4.6).

### 4.1 $10\text{ cm}^2$ Magnet Array

To demonstrate the scalability of diamagnetic levitation, we scaled up the size of the robot from a  $5\times 5$  standard checkerboard magnet array to a  $23\times 23$  standard checkerboard magnet array constructed from  $1.414\text{ mm} \times 1.414\text{ mm} \times 0.4\text{ mm}$  magnets =  $10.37\text{ cm}^2$  (539 magnets), resulting in a  $10\times$  area increase over existing state-of-the-art micro-robot geometries. The individual magnet size was chosen since it had already been proven to reliably self-levitate on Earth. Figure 4.1 shows the full magnet array levitated on 500 microns of graphite and assembled by hand in about 1-2 hours.

#### 4.1.1 Motion Analysis

We ran initial motion experiments to test the open-loop mobility and stability of the  $10\text{ cm}^2$  robot. Unfortunately, this experiment was limited by the small area of our existing test space, so we performed experiments analyzing the step response of the robot rather than attempting to achieve the maximum velocity within our test space. We performed a series of motions moving the robot back and forth (6 mm) in decreasing time intervals, with a pause inserted after a complete forward / backward cycle.

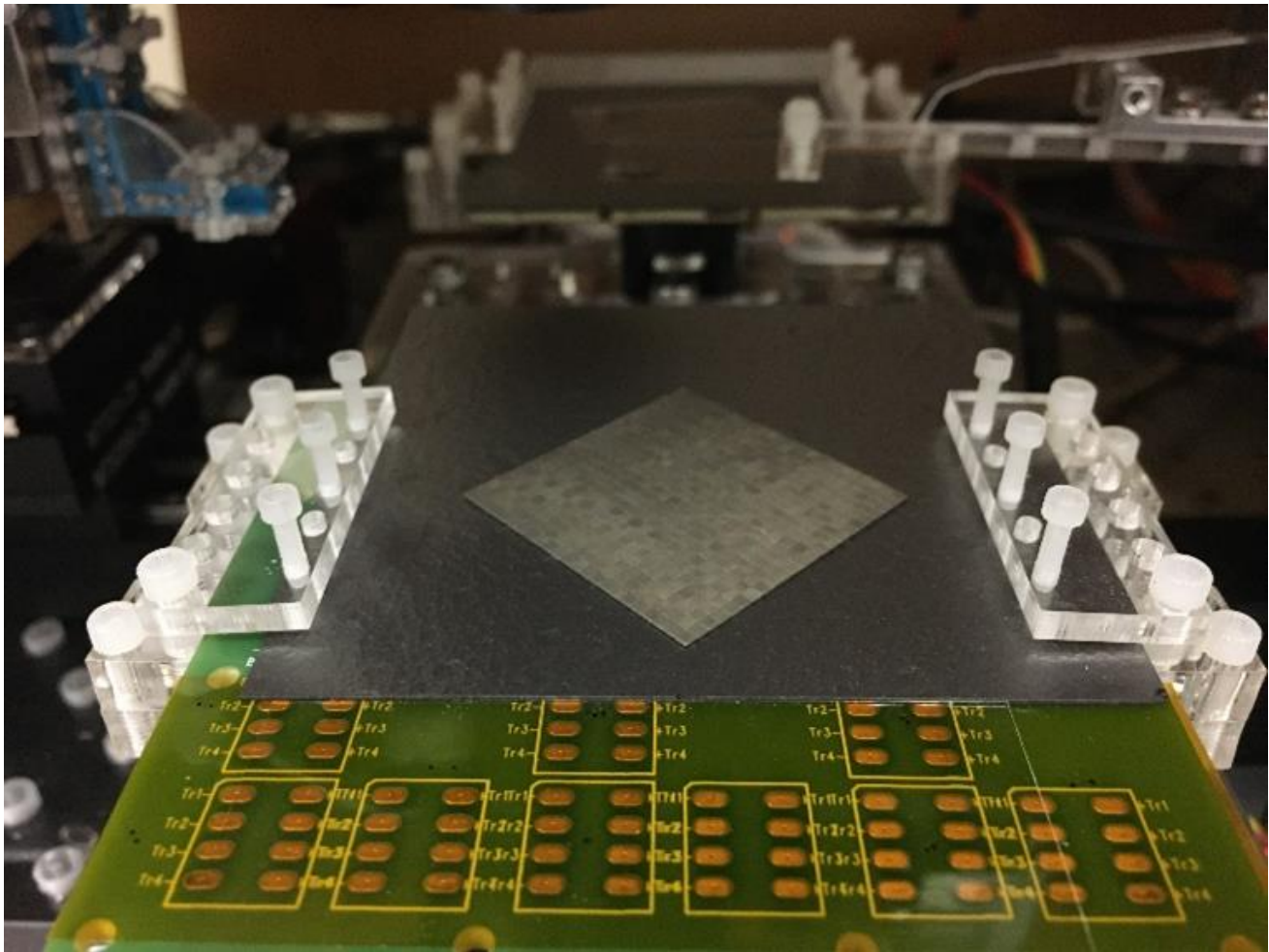


Fig. 4.1:  $10\text{ cm}^2$  Magnet Array

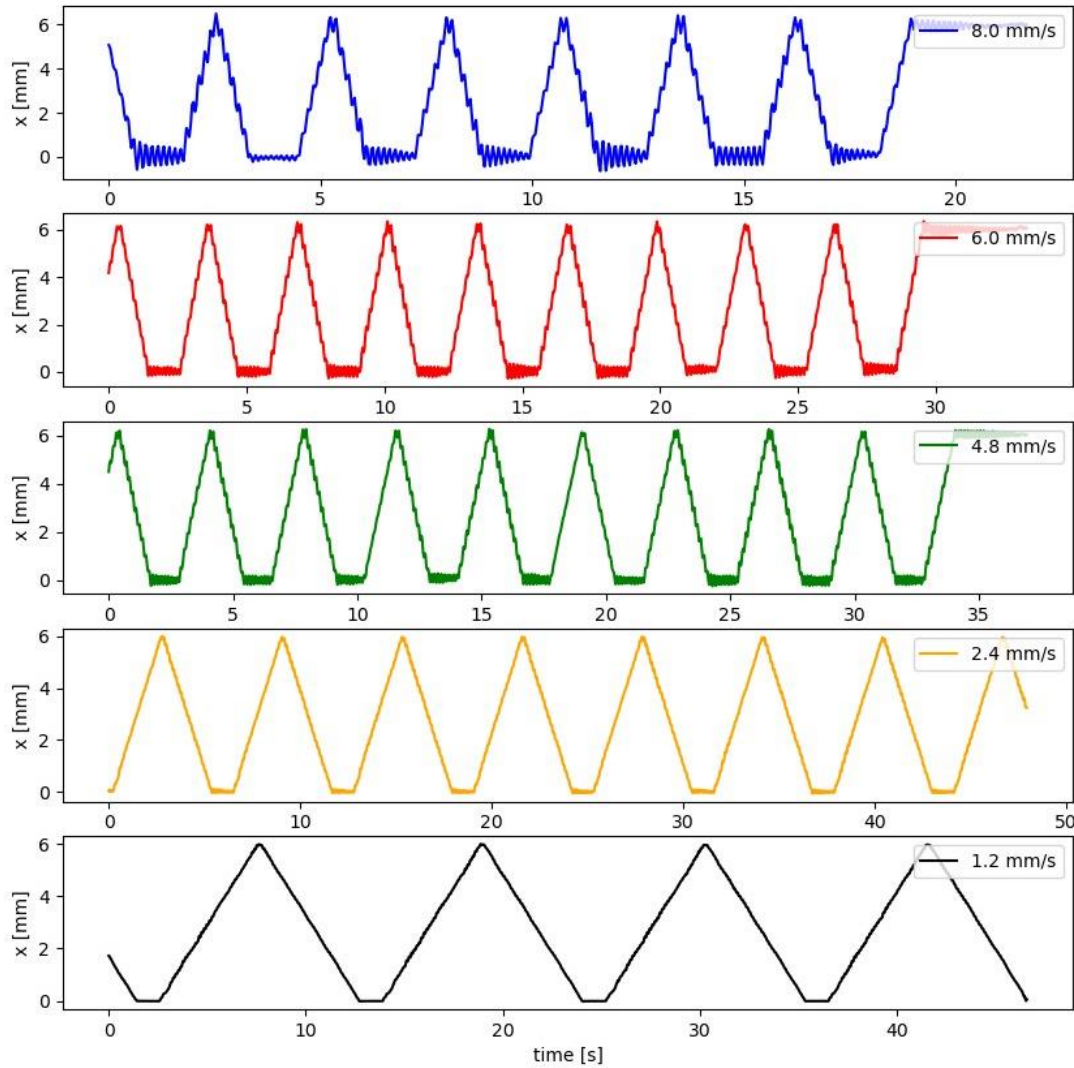


Fig. 4.2: Motion Analysis for 10 cm<sup>2</sup> robot at 8.0, 6.0, 4.8, 2.4, 1.2 mm/s.

Figure 4.2 shows the tracked motion of the robot for various cycles times of 8.0, 6.0, 4.8, 2.4 1.2 mm/s. Since the graphite itself has very low eddy current dampening, as the rate of motion increases and more closely approximates a step function, the natural resonant frequency of the levitated system ( $\sim 5\text{--}10\text{Hz}$ ) becomes excited when operating in open-loop and generates visible oscillations. When driving the system in open-loop, there is no active registration between the magnet position and the electromagnetic drive. Instead, the robot motion approximates a stepper motor, where advancing the phase of the electromagnetic traces across the track causes the magnet array to settle at a new equilibrium position (laterally translated from its prior position); however, nothing in the actuation of the robot is done to account for the mass and acceleration of the robot in these tests.

Therefore, closed-loop control is desired to achieve faster, more robust motion control. Closed-loop control can provide more efficient coupling with the force generated by the electromagnetic drive, and also introduce active dampening (using a derivative control term) to improve the step response behavior. Performing closed-loop control requires external sensing (e.g. camera or magnetic encoder) of the robot position, and has been demonstrated on smaller magnet arrays [8].



## 4.2 Dust and Abrasion Testing

To begin understanding the effects of abrasive lunar dust on the FLOAT robots / tracks, we performed a scaled experiment using lapping abrasion compounds (Lapping Compound 30654-333,  $\sim 30 \mu\text{m}$  from McMaster Carr), which have particle sizes approximately 50% of the levitation gap ( $\sim 70 \mu\text{m}$ ) for Earth-based robots [53], [60]. Initially, we simply deposited a nonuniform coating compound over the surface and then drove a small magnet array through the pile. However, we found that when too much lapping compound was placed on the surface, the robots (a 5x5 magnet array) would compact the abrasive compound rather than pushing the debris away, resulting in formation of a large debris wall that the robot could no longer move through. Since the force from the robot scales with area of the robot, we suspect that these dust compaction issues may be mitigated by a 1 m x 1 m robot (with a 40,000x increase in force).

By reducing the particle density to the level seen in Fig. 4.3, the test robot was able to easily push away the debris and clear a track. In this test, the robot follows an open-loop sweeping pattern, where the robot advances forward into the dust pile, retreats backwards a small distance, then repeats this cycle many times to slowly advance into the dust pile. At the end, the robot fully retracts from the pile. While a levitated robot is able to push through dust, two main challenges are observed:

- Electrostatic charging and attraction between particles
- Sweeping and cleaning of the robot

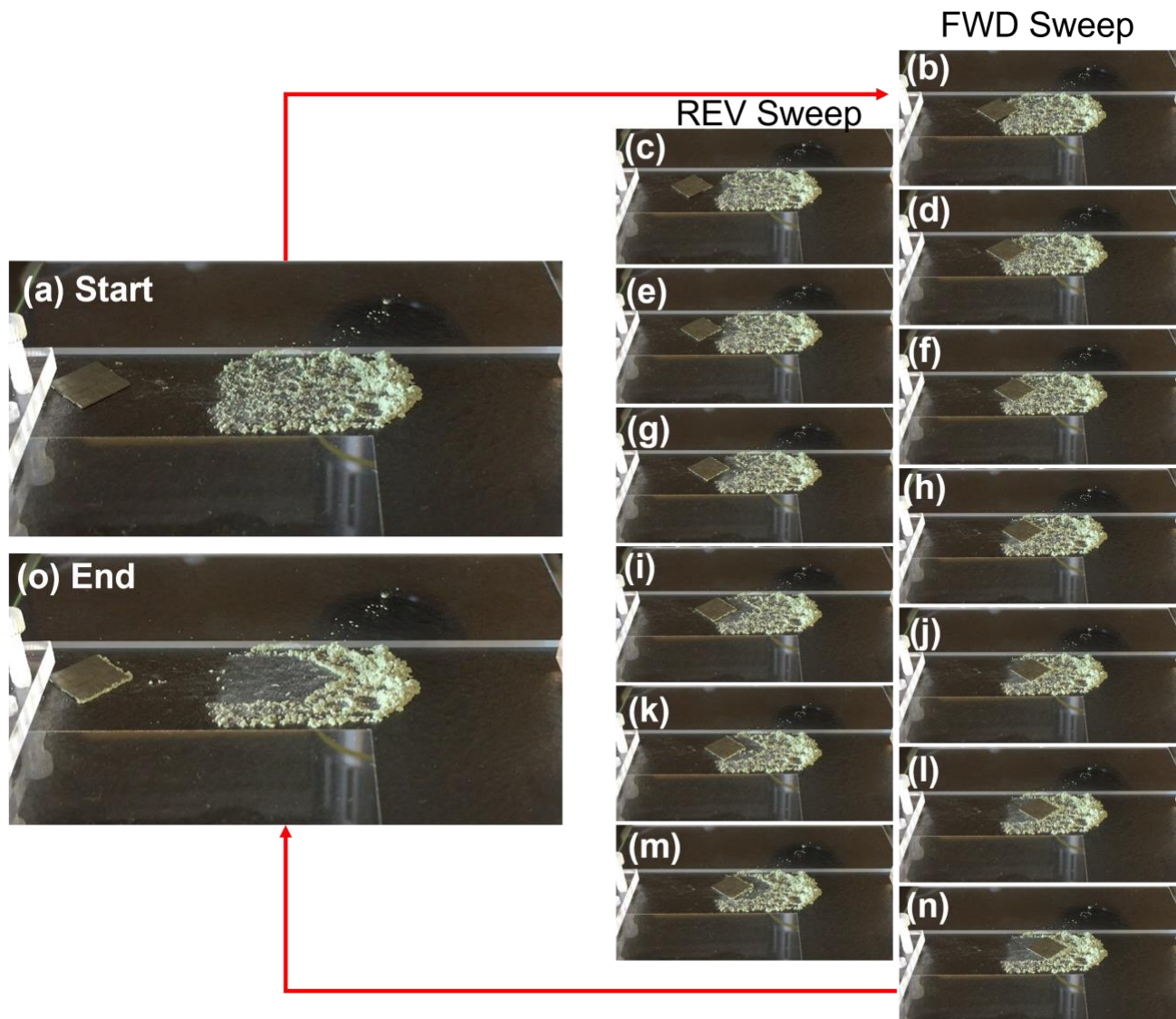


Fig. 4.3: Dust and Abrasion Testing, with the end-state robot visibly covered in debris.



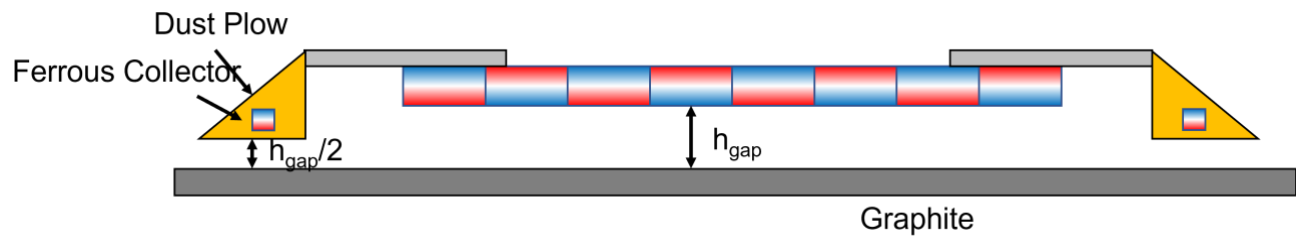


Fig. 4.4: Dust Plow Robot Concept

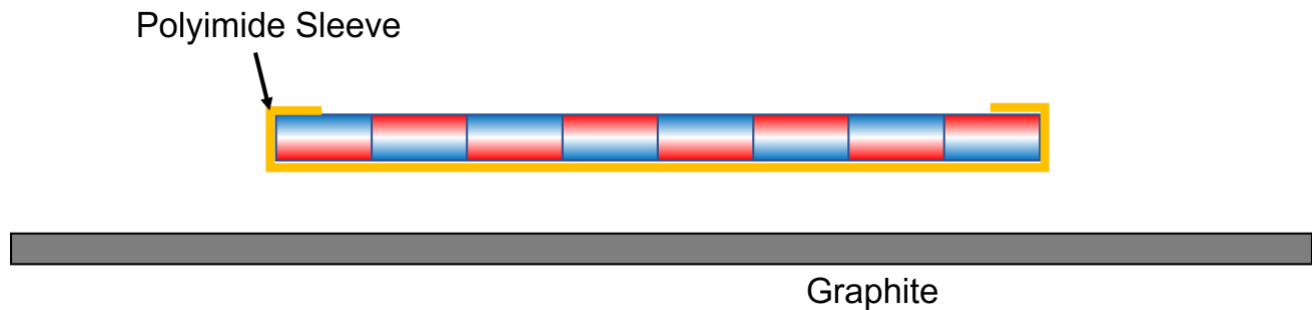


Fig. 4.5: Protective Sleeve Concept

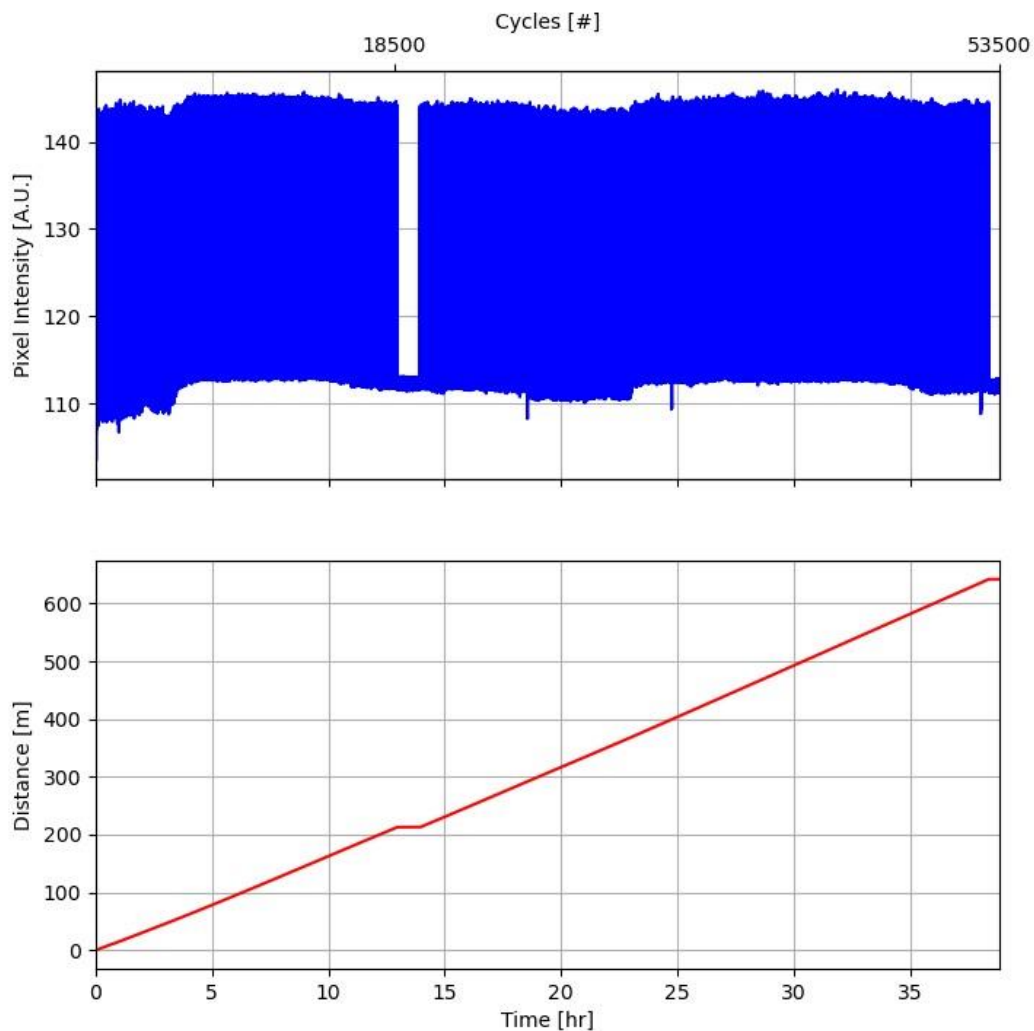
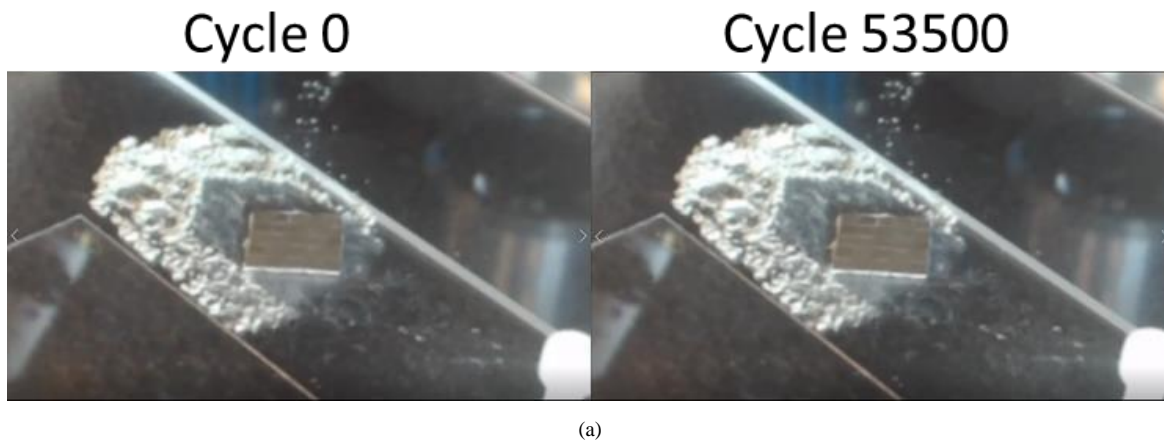
Since the robot is levitated, the robot can easily drive over particles much smaller than the levitation gap, and indeed some of these remaining particles are visible as a yellow powder residue in the swept region of the track in Fig. 4.3. Particles that are much larger than the levitation gap can also be easily brushed aside since they will not jam underneath the robot. The particles that are of the largest concern are those exactly the size of the gap, or particle clumps that are of the same or similar size to the levitation gap. Therefore, we believe by performing a pre-sweeping step with a dedicated robot to clear debris off of the track, reliable motion of subsequent robots can be achieved (Section 4.3).

To alleviate these issues, we believe a simple particle filter and offsetting the sweep from the edge of the robot, can form a kind of “snow plow” that can be easily connected or disconnected thereby attracting most of the particles to a known spot that can be removed and cleaned using other methods (Fig. 4.4). This robot would only have to operate periodically or as needed since lunar dust should only occur due to mechanical motion. By adding our dust plow to the front and back of a robot, it can push particles that are greater than half of the gap size. In addition, to clear the track of any ferrous particles, we can use a tiny permanent magnet to attract any ferrous particles on the track. By embedding the magnet into the snow plow, and also making it removable, we can easily attract particles to the dust plow, and then remove the magnet or demagnetize the magnet to remove all of the particles and then re-magnetize the collector as an easy autonomous way to clean off the particles.

Figure 4.5 shows another concept for making the robots easy to clean from electrostatic or ferromagnetic dust, by placing a polyimide sleeve or cover (thin Kapton) around the magnet. By making it easily removable, ferromagnetic particles stuck to the bottom side of the Kapton can be easily removed once the magnets are moved far enough away from the sleeve. Other electromagnetic dust and particles can be cleaned using other mechanical and electrostatic methods without affecting the magnets.

### 4.3 Life-Cycle Testing

To demonstrate that sweeping away particles is sufficient for another robot to traverse the space, we then placed a robot (the same robot after cleaning the robot of some large particle clumps) back onto the same track and then ran life-cycle abrasion tests totalling >50000 cycles for the robot, equating to >600 m of driving over the same track area. Figure 4.6 shows the image tracking of the robot using the average pixel intensity of a region of space to track the motion of the robot. The robot was run for 1,000, 17,500, and then 35,000 cycles with a delay in between the 18,500 and 35,000 cycles, since the experiment was conducted unattended overnight, totalling 53,500 cycles spanning a >72 hour time span (Figure 4.6 shows only the active testing during that



(b)

Fig. 4.6: Life Cycle Testing: (a) shows the track and the beginning of the test and at the end of the 53500; (b) shows the Cycles as a function of cycle time (actual time and pauses between cycles runs (1000,17500,35000) have been removed) and Cycles have been extracted from raw video. If any wear or tear would have been noticed, there would be motion artifacts or skips detected in the cycles in (b), but even features or markers on the track look identical between cycle 0 and cycle 53,500

time span). Each cycle consisted of a 6 mm motion forward and backwards, resulting in 12 mm of motion per cycle, and totaling 642 m over 53,500 cycles. Figure 4.6 also shows the robot and the track after 53,500 cycles. As expected, no visible wear or tear on the robot or the track was observed since the robot is fully levitated.

#### 4.4 Flexible Compliant Robots

The analysis from Section 3.1.2 illustrated the need for designing a flexible and compliant robot in order to handle undulating, out-of-plane curvature in the track. To demonstrate this concept experimentally, we explored adding compliance by linking 4 smaller magnet arrays (4x4 standard checkerboard arrays composed of 16, 1.4 x 1.4 x 0.4 mm magnets) with flexures made from 12.5  $\mu\text{m}$  thick x 1.5 mm wide x 4.24 mm long Kapton (polyimide) film (see Fig. 4.7). Effectively, we are creating a larger, compliant magnet array by linking together a series of smaller magnet arrays with compliant flexures, and replacing some of the area fraction of the larger magnet array with empty space to further provide compliance.

Experimentally, we found that only a 3 x 1.414 mm separation gap between the four connected magnet arrays was sufficient to avoid unintended attraction / snap-in instabilities between them. Due to the internal multipole configuration within each of the four checkerboard magnet arrays, the interaction forces between magnet arrays does not scale with the area of each array, since most of the fields cancel due to the alternating north–south configuration within each array. Therefore, for larger magnet arrays (e.g. 1 m x 1 m), the same separation distance (3 x 1.414 mm) can also be used. With this magnet array, we are able to demonstrate levitation of our compliant robot within a graphite well with a radius of out of plane curvature of 7.5 cm (Fig. 4.7). As a control, we also built a similar sized complete standard magnet array (4 x 11) with the same length as our compliant robot and find in the same graphite bowl that the magnet array gets stuck due to bottoming out as expected (Fig. 3.8).

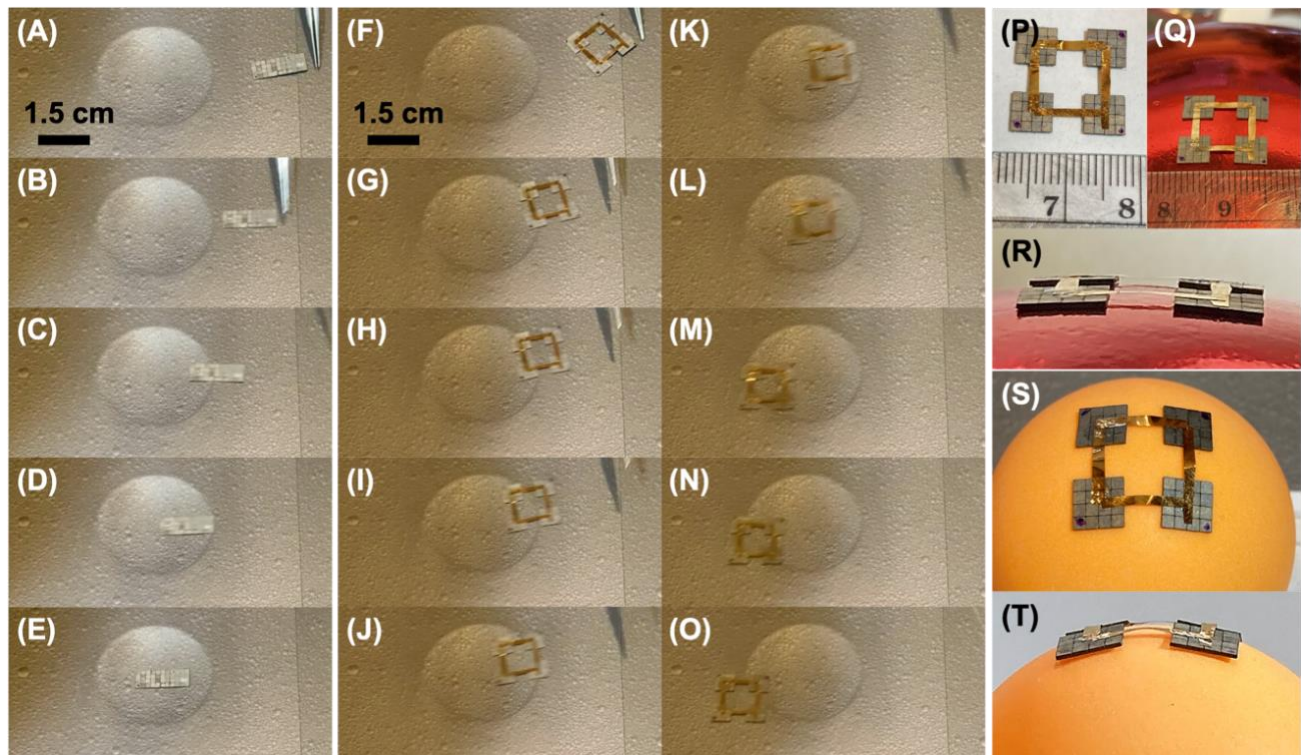


Fig. 4.7: A rigid robot (1.55 x 0.56 cm) gets stuck in a curved bowl / crater carved into pyrolytic graphite (A-E), while a compliant robot (1.55 x 1.55 cm) of equal length moves unimpeded through the same bowl (F-O). Close-up images of the compliant robot on flat (P) and curved surfaces of 7.5 cm radius (Q-R) and 1.25 cm radius (S-T). Compliant robot is composed of four 4 x 4 arrays of 2 mm<sup>2</sup> magnets held together with polyimide tape. Video available at: <https://www.youtube.com/watch?v=rQ2p-qdPW1>

#### 4.5 Magnetization and Repair of Magnets

To tackle issues of repair and durability, we also investigated methods of repairing aspects of the FLOAT track. One primary concern is the demagnetization of the magnets over time, potentially due to temperatures exceeding the operating temperature for NdFeB [62] – ranging from  $80^{\circ}\text{C}$  to  $200^{\circ}\text{C}$ , and dependent on the type of NdFeB magnet chosen (as there are material trade-offs between the remanant magnetization ( $B_r$ ) and Curie temperature). Temperatures below the operating temperature are reversible (i.e. the magnetization recovers); however, temperatures above the Curie result in irreversible demagnetization. Fortunately, magnets can be remagnetized when placed in the presence of a strong enough magnetic field to re-align the magnetic domains.

Figure 4.8 shows a simple magnetizer using a split solenoid constructed from two solenoids in series to generate a large uniform magnetic field along the central axis of the solenoid. The gap between the solenoids is  $\sim 700\text{--}800\ \mu\text{m}$  with a peak magnetic field of  $\sim 25000\ \text{G}$  [2.5 T]. To generate the large magnetic field without overheating the coils, we pulse the coils using a high voltage power supply (150 V) for 1.5 ms shown in Figure 4.8c at 58 A. We use an optocoupler or optorelay to isolate the high voltage power supply from the digital control, which was provided using an Arduino MEGA 2560 microcontroller. The peak pulse that can be applied is determined by the inductance of the solenoid ( $L = 270\ \mu\text{H}$ ) and the resistance of the coil ( $R_{\text{coil}} \sim 2.1\ \Omega$ ).

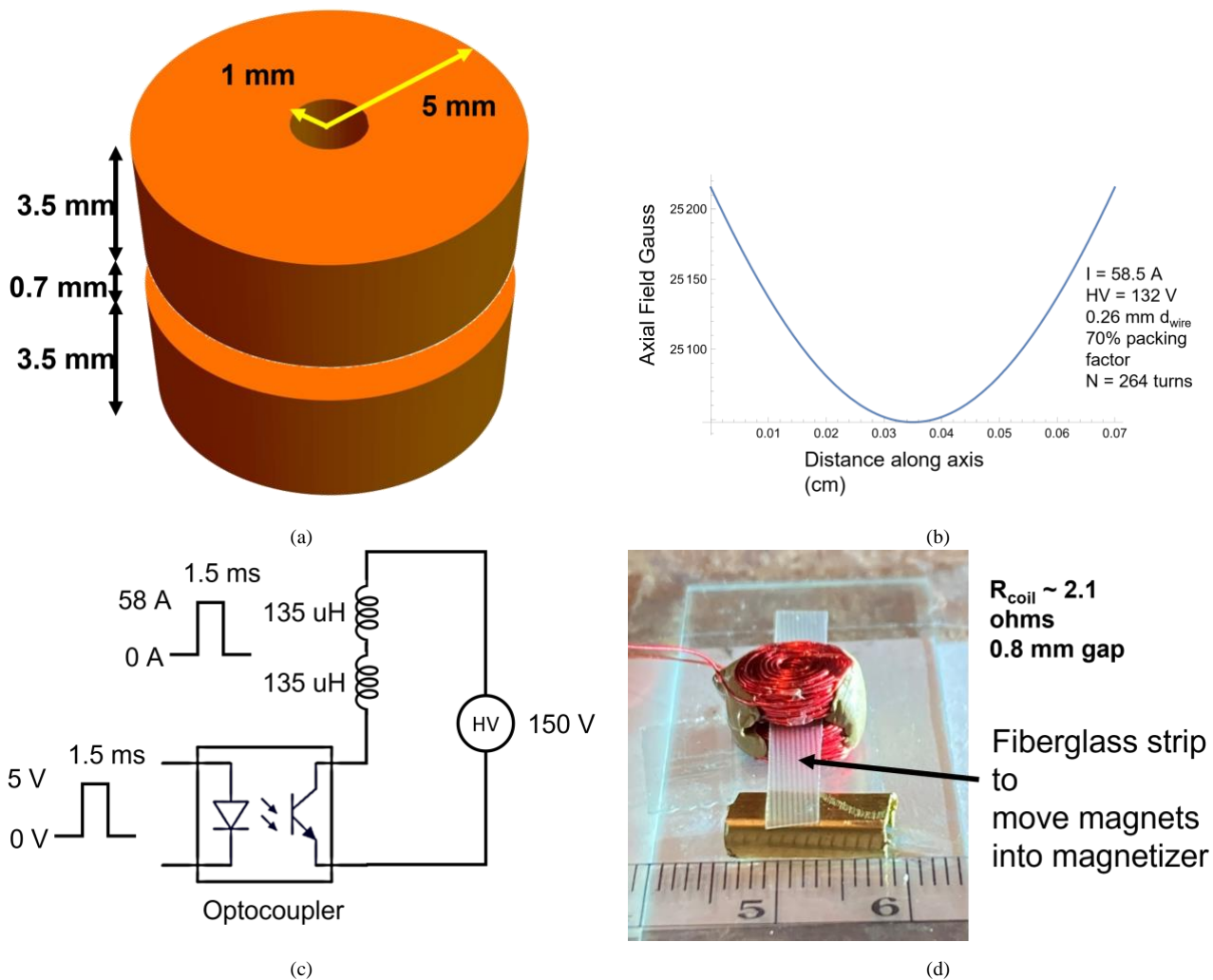


Fig. 4.8: Magnetizer. (a) Diagram of Magnetizer Coils, (b) Simulation of Magnetic Field for Magnetizer, (c) Circuit Schematic for Magnetizer, (d) Experimentally Constructed Magnetizer. A fiberglass tray is used to insert magnets into the peak magnetic field found in the center of the gap and in the center of the inductor



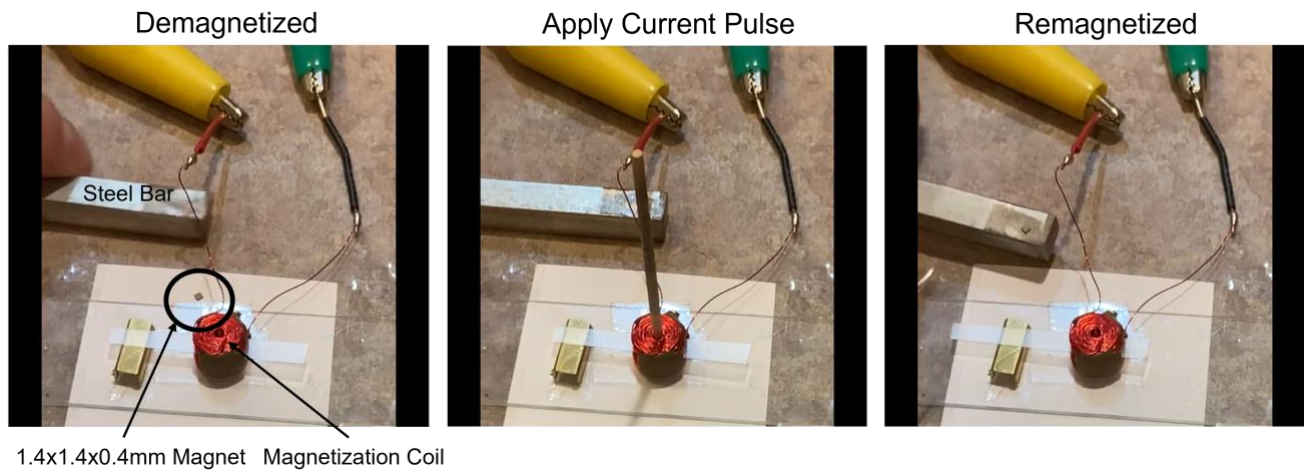


Fig. 4.9: Remagnetization Procedure for a Single Magnet: Demagnetized (dead) magnet falls off steel bar (left); magnet is magnetized (middle); fully magnetized magnet (right) sticks to steel bar in mid-left of image.

Figure 4.9 shows a complete cycle of how the individual magnets assembling the robot can be remagnetized after thermal cycling. By placing the individual magnets inside of the magnetization volume and turning on the magnetizer we can achieve  $\sim 98.5\%$  magnetization (measured through the biased-levitation of the re-magnetized magnets). While this experiment was intended to investigate the repair of magnets, this same approach can also be used for the automated construction of magnet arrays as un-magnetized magnetic feed-stock can also be introduced into the magnetizer and by changing the polarity of the current pulse, we can magnetize magnets both positive and negative and then assemble into the array using self-assembly processes [7].

#### 4.6 Vacuum Testing

One final potential environmental / operating concern that must be considered for the FLOAT concept, is operating in a vacuum environment. In past unpublished work, we have conducted operation of the FLOAT hardware (i.e. levitated magnets, graphite, and electromagnetic drive) within a standard scanning electron microscope (SEM) shown in Figure 4.10, with the control electronics and power amplifiers located outside of the SEM. We performed multiple bake-outs and dehydration of the components before operation and were able to achieve  $1.55 \times 10^{-6}$  Torr. Figure 4.10 shows the infrared camera located within the SEM that enabled us to observe full levitation of the micro-robot (5x5 standard array). In addition, we were also able to directly image the robot with the electron-beam during operation, thereby exposing the robots to a charge environment while levitated. Due to operation in the vacuum, thermal dissipation was more challenging within the SEM since the stage column was not designed for power dissipation; however, the SEM stage stayed well within standard operating temperatures and no large degradation of levitation was observed.



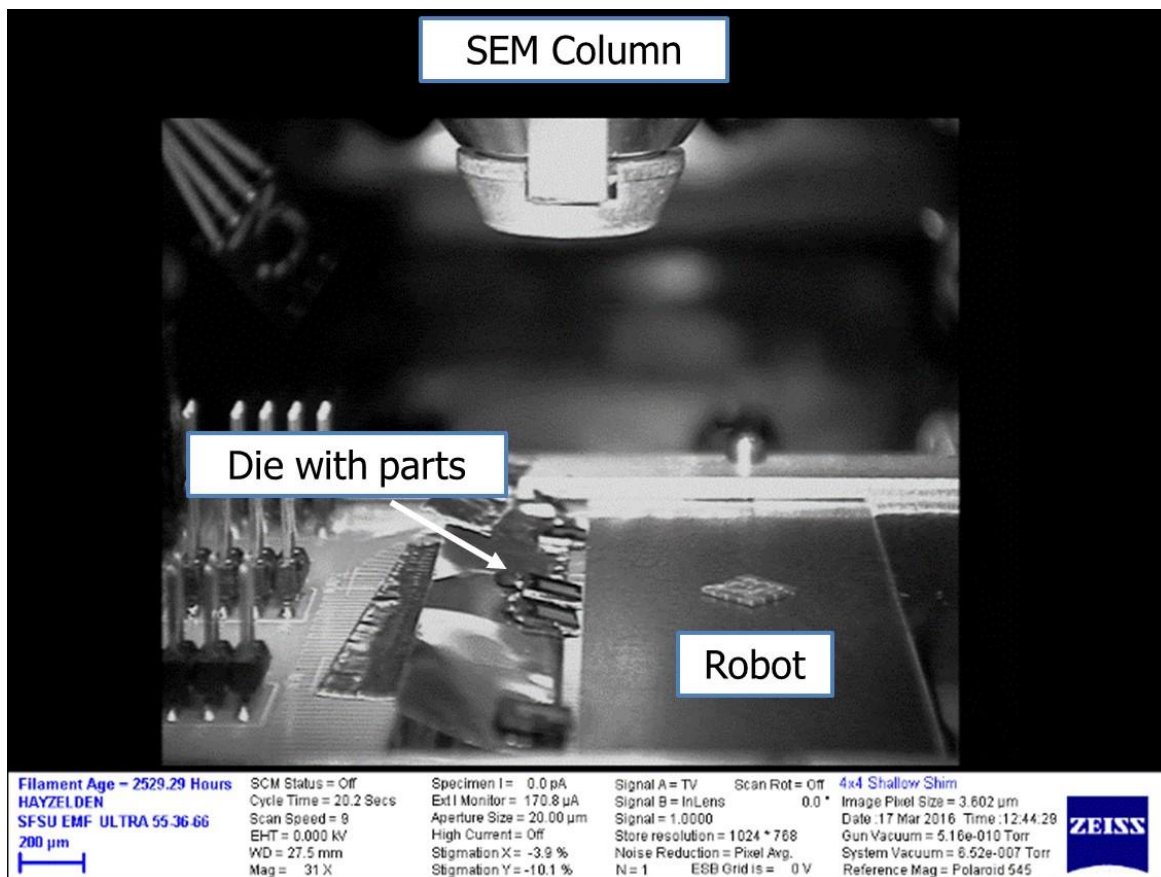


Fig. 4.10: Operation of Diamagnetic Levitated System within a Scanning Electron Microscope.  
Image acquired / provided by SRI.

## 5 SYSTEM DESIGN

System design work focused on 2 major areas for the FLOAT concept: (1) trade space analysis (Sec. 5.1), including total system requirements (mass, power, etc.) for the three RLSO2 mission options and cost-of-transport comparison to wheeled robots; and a (2) refined models for the FLOAT robots, tracks, and deployment system (Sec. 5.2) based on lessons-learned from the simulation and experimental results in the prior sections.

### 5.1 Trade Space Analysis

We developed a FLOAT system simulation that combines performance estimates with RLSO2 mission parameters to design / size potential lunar FLOAT systems. The model is quite versatile, and can calculate system design properties (e.g. number of robots, system mass / volume, power consumption / generation) across a range of input parameters, including robot / track performance levels (e.g. robot speed / payload), 3 lunar base mission options (e.g. track distance / daily payload req.), and 3 track configurations (see Fig. 5.1). It also estimates solar power generation based on solar flux for each mission option's latitude (see 2.4) and system power consumption based on each mission option's expected slope. The model uses the simulation results we found in our incline analysis (see Sec. 3.2.3) and a rough estimate of the maximum slope in each mission option to calculate a conservative peak system power consumption.

#### 5.1.1 Track Configurations

Three different track configurations are being considered and modeled as illustrated in Fig. 5.1. The first configuration is an “out and back” configuration where the robots travel primarily along a single track with pull-offs to allow robots traveling in opposite directions to pass each other. The number of robots ( $N$ ) required in this track configuration is calculated as follows:

$$N = \frac{2lq}{vTc} \quad (5.39)$$

$$l = 3 \cdot \frac{N}{2} (L_R + s) + d \quad (5.40)$$

Combining equations 5.39 and 5.40:

$$N = \frac{2dq}{vTc - 3L_Rq - 3sq} \quad (5.41)$$

Where,

$N$  = number of robots

$d$  = distance between base and mine ( $km$ )

$l$  = total track length ( $km$ )

$L_R$  = length of robot ( $km$ )

$s$  = minimum spacing between two robots ( $km$ )

$q$  = daily quota of material ( $kg$ )

$T$  = time per day operational ( $hr$ )

$v$  = robot speed ( $km/hr$ )

$c$  = robot payload capacity ( $kg$ )

The second track configuration we have modeled is a two parallel track configuration where robots travel along one section of track going from the mine to the base and a separate track traveling from the base to the mine. There are intermittent connections between the two parallel tracks to allow for continued use even if sections of the track are in need of maintenance. The number of robots required in this configuration is calculated using the following equation:

$$N = \frac{2dq}{vTc} \quad (5.42)$$

Where,

$N$  = number of robots

$d$  = distance between base and mine ( $km$ )

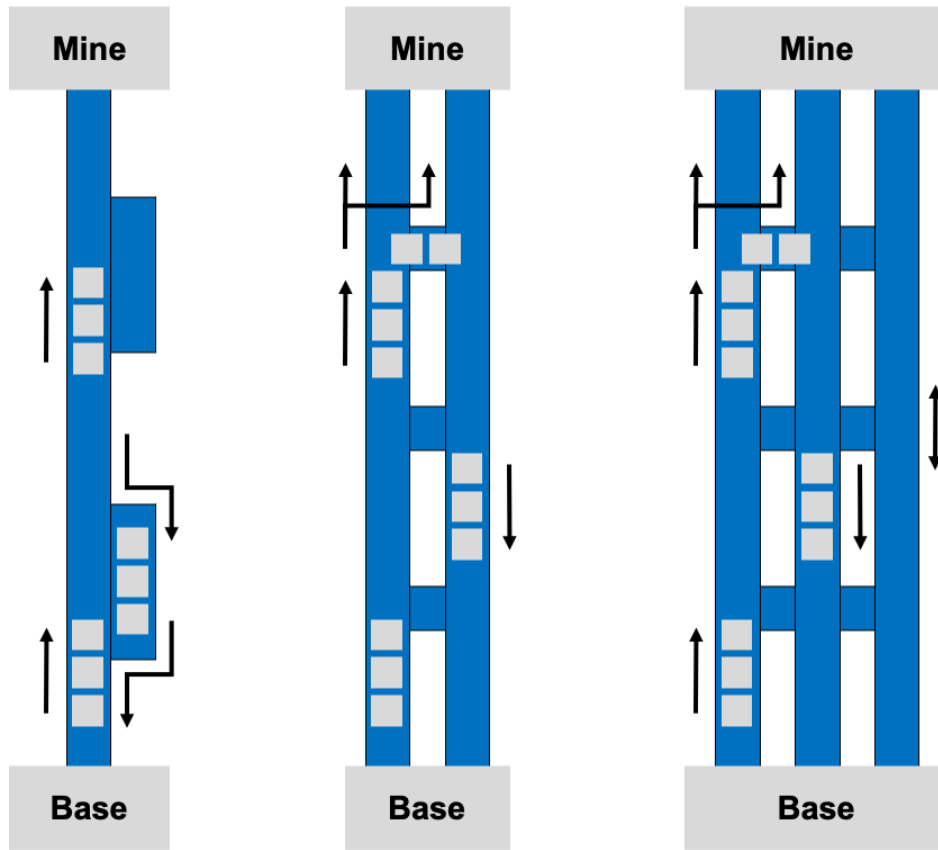


Fig. 5.1: Track Configuration Options. Left to right: Out and back configuration, Two parallel track configuration, Three parallel track configuration.

$q$  = daily quota of material ( $kg$ )

$T$  = time per day operational ( $hr$ )

$v$  = robot speed ( $km/hr$ )

$c$  = robot payload capacity ( $kg$ )

The final track configuration being considered is a three parallel track configuration. This works the same as the two parallel track configuration but there is a third track included primarily to be used when one of the other two track sections is down for maintenance. This configuration requires a larger amount of track but will minimize system downtime. The number of robots required are calculated using the same equation as in the two parallel track case (Eq. 5.42).

### 5.1.2 Trade Space Analysis Results

As expected, the results of the system simulations show that the number of robots required is inversely related to both the payload capacity of each robot and the speed of travel (Fig. 5.2). We found that travelling at speeds  $>2$  km/hr (0.5 m/s) guarantees a reasonable number of robots in the system irrespective to the payload capacity of the robots. Another important finding was the relationship that the travel distance and travel speed have on the total mass of the system. As can be seen in Fig. 5.3, the system mass is driven more by the length of track required than by the speed of the robots. This will inform the system design to favor configurations with shorter sections of track to reduce the mass of the system. Fig. 5.5 the packing volume required to transport the system to the moon has a near identical relationship with the robot speed and distance showing that the packing volume of both the track and the robots is proportional to their mass. The track packing volume is calculated by considering the total track length as split up into 100 m rolled up segments of track with an inner radius of 25 cm, and additional 10 cm buffer is included between each roll of track. The volume of the robots is simply the volume of the robots plus their regolith trays with a 2 cm buffer between each robot. We also investigated the relationship that robot speed and distance between the mine and base have on the power generation / consumption (Fig. 5.4). The plots for each RSLO2 mission

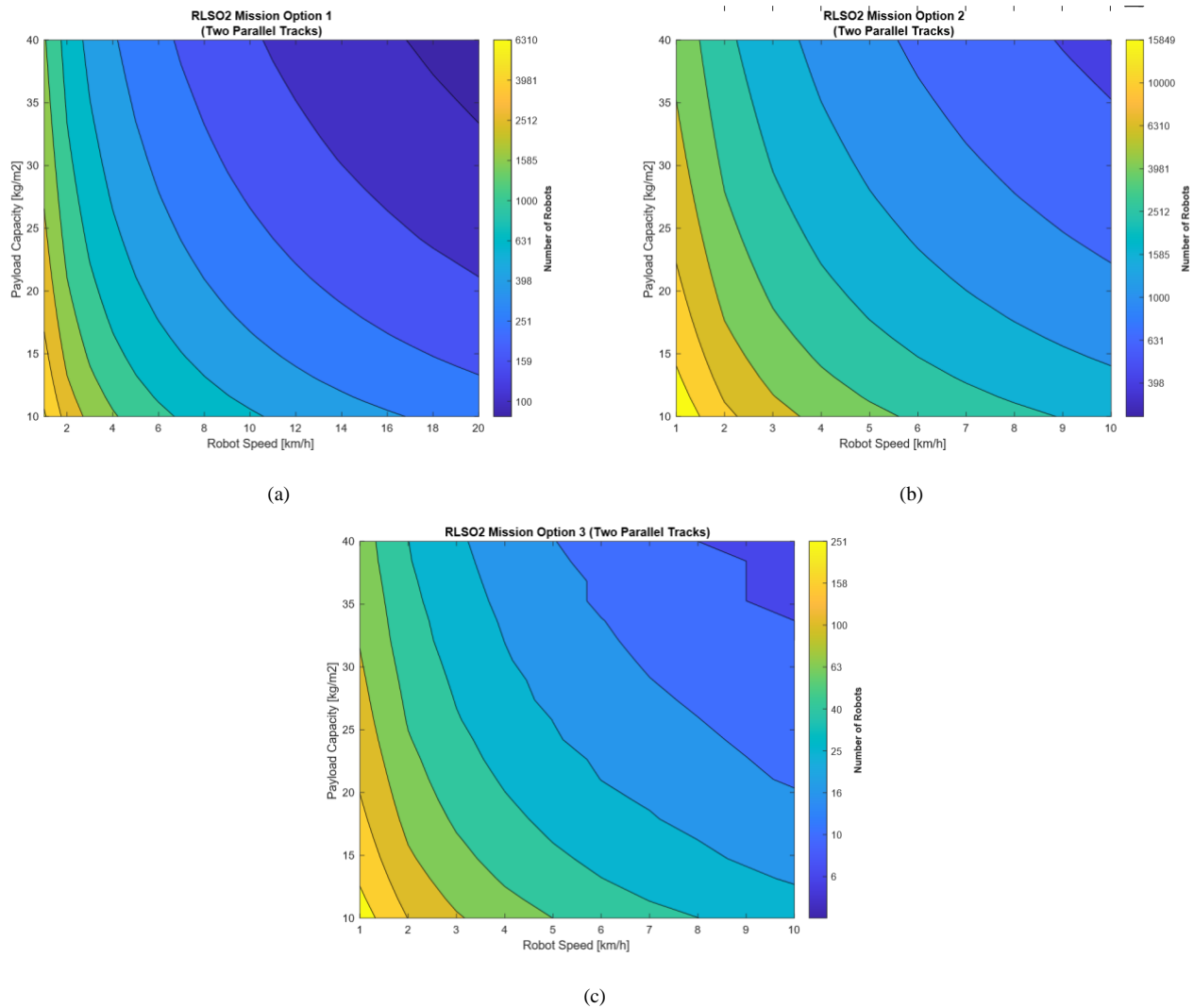


Fig. 5.2: System Trade Space Analysis: Robot Speed v. Payload Capacity v. Robots. These three plots show the effect that the robots' speed and payload capacity has on the number of robots required to meet the daily payload quota in each RSLO2 mission option. In all cases the number of robots required is inversely proportional to both the speed and payload capacity. These plots also show that it is likely necessary for the robots to travel at a speed  $> 2$  km/hr. (a) Shows the results for RSLO2 Mission Option 1 (b) Shows the results for RSLO2 Mission Option 2 (c) Shows the results for RSLO2 Mission Option 3.

option look quite different due to each being in different sunlight conditions. Option 1 is in a permanently shaded region therefore there is no power generation and the power consumption only depends on the number of robots in the system. Option 2 is assumed to have 45% of the track in sunlight and the power generation increases with the length of track required as the longer the track the more surface area there will be for power generation, the power generation also increases slightly with robot speed as less distance of track is needed to generate the same amount of power. This is due to the fact that a higher robot speed results in less robots and therefore reduced system power consumption. Option 3 is assumed to have 85% of the system in direct sunlight, this combined with the fact that option 3 requires very few robots leads to the power output being almost totally dependent on the length of track required.

The results from this system model will be a valuable tool in determining the specifications the FLOAT system must meet to be feasible, this model will need to be enhanced further to be more useful as this project matures.

### 5.1.3 Future System Model Development

In future work, we would like to enhance this model to provide realistic estimates for mission-specific FLOAT track layouts on the Moon, based on lunar satellite imagery and digital elevation maps (DEMs). Key drivers of system power consumption are

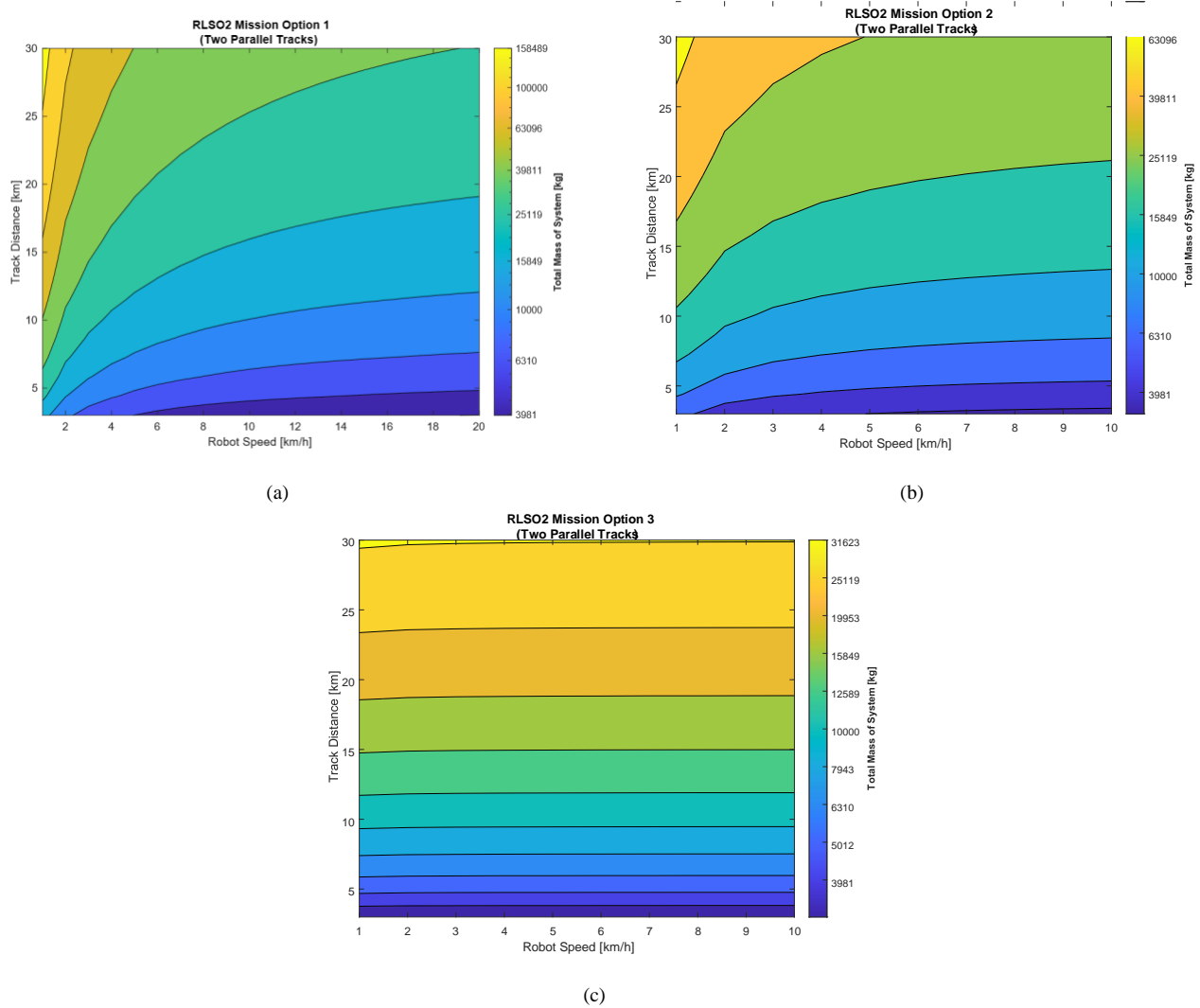


Fig. 5.3: System Trade Space Analysis: Robot Speed v. Track Distance v. System Mass. These three plots show the effect that the robots’ speed and the distance between the base and mine have on the total system mass. In all three cases the mass is directly proportional to both the speed and distance, but it is apparent that the track distance has a greater effect on the system mass. (a) Shows this relationship for RLSO2 Mission Option 1. (b) Shows this relationship for RLSO2 Mission Option 2. (c) Shows this relationship for RLSO2 Mission Option 3. In this case the robot speed has almost no effect on the total system mass, since so few robots are needed for this option the mass is almost entirely driven by the length of track required.

the track slopes / curves around which the FLOAT robots must maneuver, so grounding our models in realistic lunar terrains will be critical for accurate system power estimates. Outputs from the system model (e.g. Fig. 5.2) also show the significant interdependence of system mass / volume with the number of robots, per-robot speed / payload, and track length. For this reason, we would like to incorporate a realistic “traffic flow” model that incorporates robot acceleration / max velocity profiles on top of the realistic track layouts (e.g. hills / craters, curves, or junctions).

#### 5.1.4 FLOAT Sizing for RLSO2

Based on FLOAT performance (Sec. 1.1) and regolith / ice transport masses for the three RLSO2 mission options (Sec. 1.2), the FLOAT system size necessary to support RLSO2 operations can be estimated. Using the system simulation described in Sec. 5.1 we are able to calculate single point solutions based on a standard design point that assumes FLOAT robots are 1x1 meter (1 m<sup>2</sup>) in size, with 3 kg/m<sup>2</sup> robot mass and 30 kg/m<sup>2</sup> payload (3 kg/m<sup>2</sup> of container mass, 27 kg/m<sup>2</sup> regolith), travel at the tested top speed of 2.0 km/hr (0.55 m/s), consume ~1-5 W power each (fully-loaded on slopes up to 40°), and move 90% of the day. Thin-film solar cell efficiency assumed to be 20.4% [11]. Note that power estimates are for energizing the track / controlling robots,

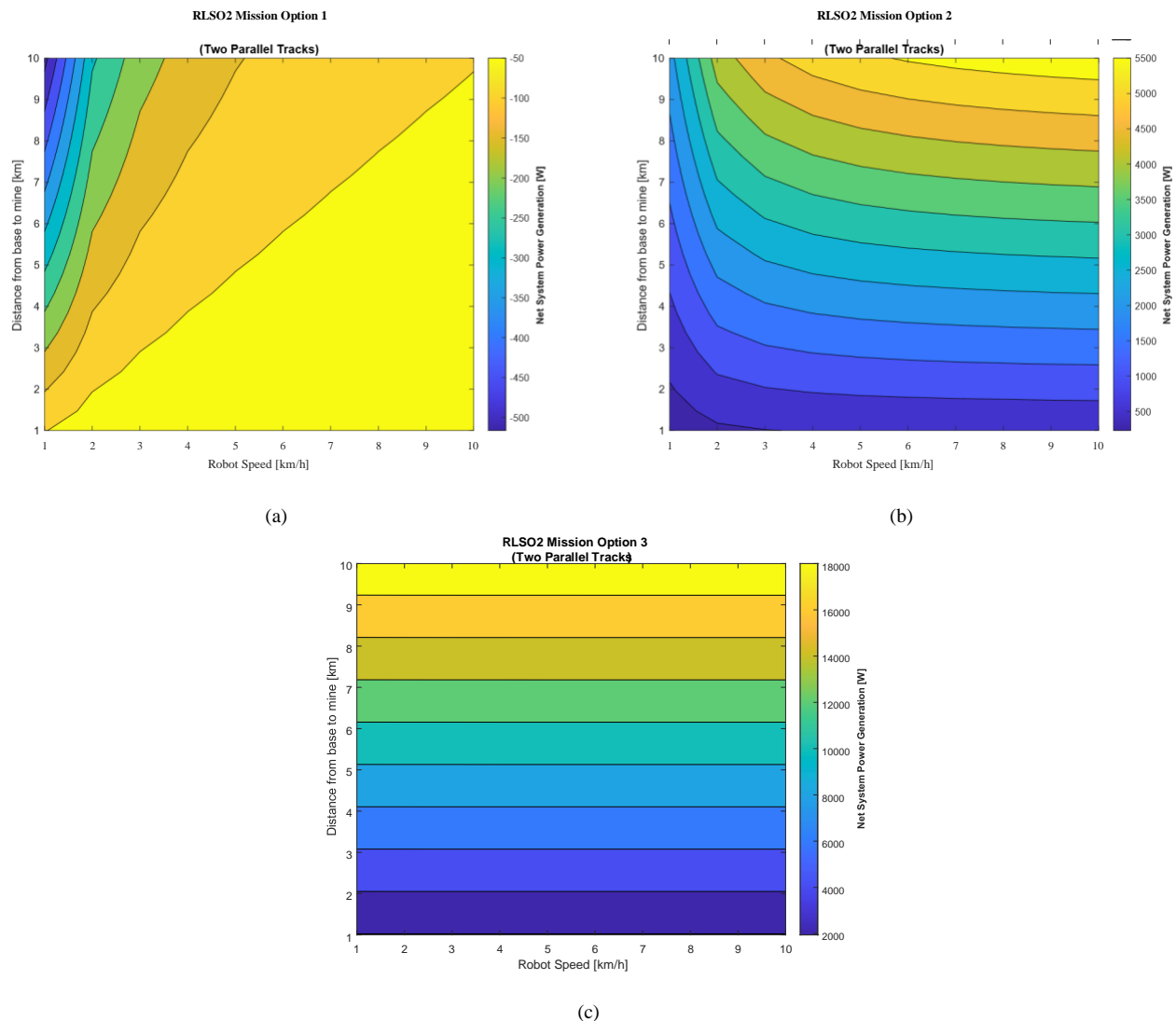


Fig. 5.4: System Trade Space Analysis: Robot Speed v. Track Distance v. Net Power Generation/Consumption. These three plots show the effect that the robots' speed and the distance between the base and mine have on the net power generation/consumption of the system. These plots use a conservative estimate that assumes all the robots in the system are climbing the max expected slope at the same time. To calculate the power consumption a model derived from the data in 3.2.3 is used. A solar efficiency value of 20.4% is used and the solar flux model discussed in 2.4 is used to determine the power generated. (a) Shows this relationship for RSLO2 Mission Option 1. In this mission option the system is in a permanently shaded region so there is no power generation. The power consumption will increase with the number of robots required so short distances and fast speeds will lead to lower power consumption. (b) Shows this relationship for RSLO2 Mission Option 2. In this case it is assumed that 45% of the system is in sunlight. It can be seen that in this case having longer track increases the power generation and there is also a slight increase in power generation as speed increases. This is due to the reduced number of robots in the system required at higher speeds. (c) Shows this relationship for RSLO2 Mission Option 3. In this case 85% of the system is in sunlight and the robot speed has almost no effect on the net power generation, since so few robots are needed for this option the power generation is almost entirely driven by the length of track.

and don't currently include controller power usage. Based on these assumptions:

**Option 1:** Carry 236,000 kg/day of raw regolith <1 km on flat terrain

- **System:** 379 Robots, 2 km Track (<1 km distance with 2-lanes or a continuous loop)
- **Mass:** 4,804 kg = 2,113 kg for track + 2,691 kg for robots / containers (w/ 10,953 kg payload)
- **Power:** <77 W peak consumed by robots (no sunlight for solar power generation on track)



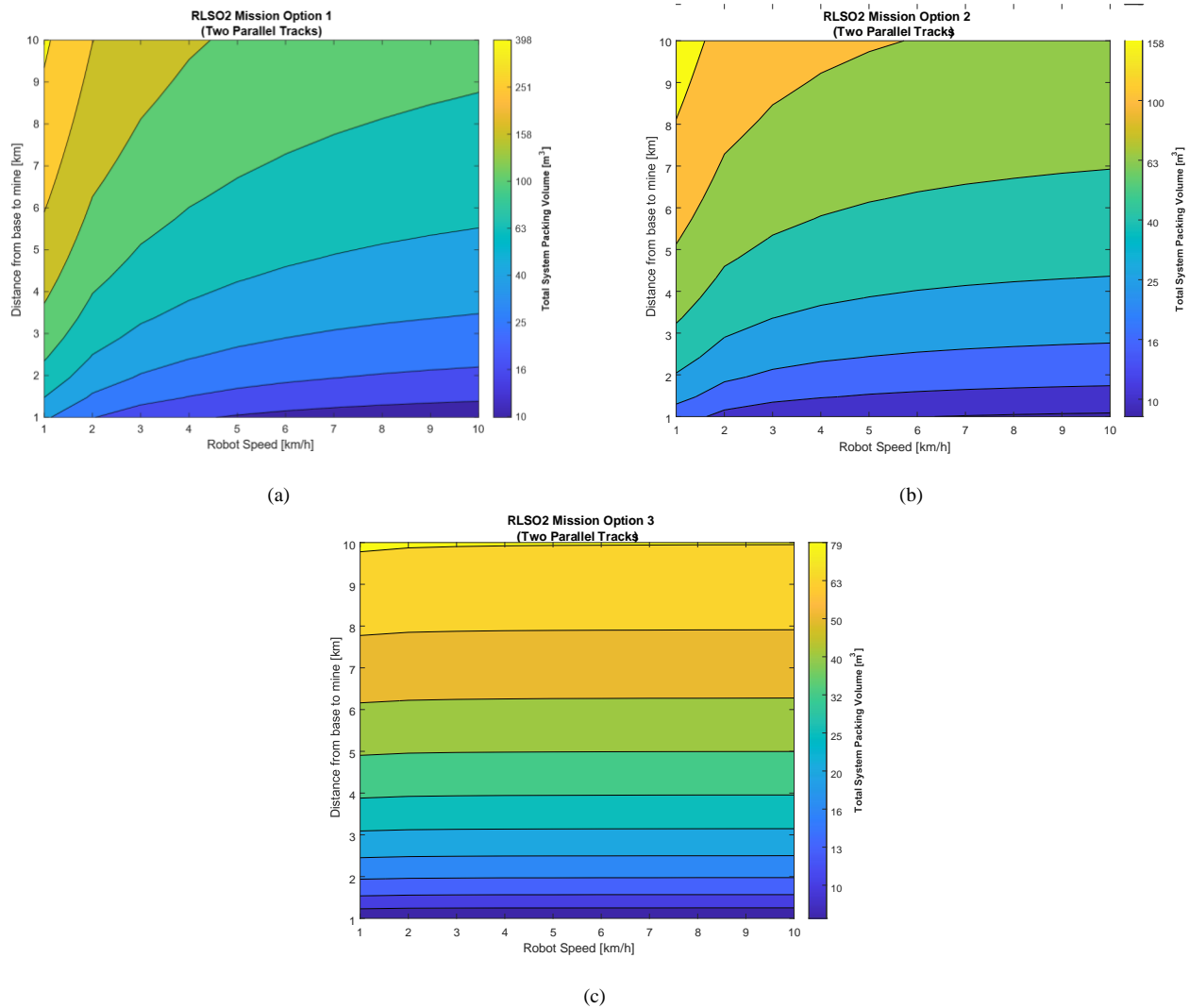


Fig. 5.5: System Trade Space Analysis: Robot Speed v. Track Distance v. Total System Packing Volume. These three plots show the relationship between the robot's speed and the distance between the base and mine have on the total packing volume the system would take up during transport to the moon. The volume of the track sections are calculated by determining how many 100m long rolls of track would be needed. The rolls of track are assumed to have an inner radius of 25 cm. A 10 cm buffer between rolls is given to make the estimate conservative. The robot packing volume is calculated by the volume of the robots plus a 2 cm buffer between robots. In all three cases these plots look very similar to the total mass plots shown in Fig. 5.3 this means that both the robots and track take up a volume proportional to their mass. (a) Shows this relationship for RLSO2 Mission Option 1. (b) Shows this relationship for RLSO2 Mission Option 2. (c) Shows this relationship for RLSO2 Mission Option 3.

**Option 2:** Carry 80,000 kg/day of beneficiated regolith ~10 km up crater rim at 35° slope

- **System:** 1,282 Robots, 20 km Track (<10 km distance with 2-lanes or a continuous loop)
- **Mass:** 30,235 kg = 21,133 kg track + 9,102 kg robots / containers (w/ 37,050 kg payload)
- **Power:** <1.94 kW peak consumed (4.1 kW generated by track if 45% in sunlight on slope)

**Option 3:** Carry 1,130 kg/day of water 3-8 km on moderate terrain

- **System:** 15 Robots, 8 km Track (<8 km distance, robots platoon to minimize pull-offs)
- **Mass:** 8,607 kg = 8,500 kg track + 107 kg robots / containers (w/ 434 kg payload)
- **Power:** <3 W peak consumed (5.2 kW generated by track if 85% in sunlight)

A complete FLOAT system implementation will thus require approx. 5,000-30,000 kg of payload delivered to the Lunar base, along with a FLOAT track deployment system compatible with a construction rover like ATHLETE or P@X [23], [63], [64]. For comparison, equal lengths of train tracks have >40x track mass (plus trains / railcars) and cableways have up to 10x cable mass (plus towers / buckets). Additionally, with future planned lunar landers (SpaceX Starship HLS) having a purported 100,000-200,000 kg payload to Moon, an entire FLOAT system would be able to be transported to the Moon on a single flight.

FLOAT's predicted peak power consumption for driving the robotic fleet (<2 kW) in even the most demanding situation (up the slope of Shackleton Crater, in Option 2) is also small – amounting to <0.4% of RLSO2 net base / ISRU power consumption (515-959 kW) [21]–[24] – although it does not yet account for the additional power requirements of the track control electronics, or electrical losses along the track.

FLOAT robot speed (2.0 km/hr at small scales) limits the number of daily round trips each robot can make, and thus significantly impacts the quantity of robots required for a given mission (especially in Option 2). Increasing robot operating speed will be an important component of future study and beyond. Other potential 'death threats' for FLOAT include: performance degradation from environmental factors (thermal, dust, micro-meteoroid impacts), inadvertent robot / track contact during motion (track curvature over terrain, payload distribution, robot overloading), and track panel alignment accuracy (impacts ability to confine / propel robots along the track).

### 5.1.5 Cost-of-Transport Comparison

One of the major advantages of FLOAT over alternative regolith transportation options is the low power requirements associated with the system. A good method for comparing the energy efficiency of two transportation methods is by calculating the cost of transport [65] which is calculated as follows:

$$COT = \frac{P}{mgv} \quad (5.43)$$

Where,

$P$  = Power input to the system (W)

$m$  = Mass of vehicle (kg)

$g$  = Acceleration due to gravity ( $m/s^2$ )

$v$  = Vehicle velocity (m/s)

Using the data from our incline analysis (Sec. 3.2.3), we are able to estimate the power requirement of a FLOAT robot with a given payload on a given slope. We chose to compare FLOAT's efficiency of transport to that of a wheeled rover, which is a well understood alternative solution. To calculate the electrical power input for a wheeled rover traveling up a slope, we used the following equation:

$$P_{rover} = mgv(R + \tan(\phi)) \quad (5.44)$$

Where,

$m$  = Rover mass (kg)

$g$  = Acceleration due to gravity ( $m/s^2$ )

$v$  = Rover velocity (m/s)

$R$  = Motion resistance

$\phi$  = Incline angle (degrees)

Using the power estimates for the FLOAT robots and a rover with the same parameters as NASA's Mars 2020 Perseverance rover, we are able to compare both the power requirements and cost of transport of the two systems – shown in Fig. 5.6. The comparisons were done between a fleet of FLOAT robots that carry an equivalent payload to the single rover (assumed to carry 150% of its mass as additional payload). A motion resistance value of 0.06 was used for the rover, which is considered a "state of the art" motion resistance. The results of these comparisons are shown in Fig. 5.6, which shows that the FLOAT robots have  $\sim 10^3$ x reduced cost of transport (Fig. 5.6a) and  $\sim 10^1$ - $10^2$ x reduced electrical power (Fig. 5.6b) compared with a rover. An additional advantage of the FLOAT system is that the power requirement does not notably increase with velocity (Fig. 5.6c), as it does on wheeled vehicles, until extremely high velocities are achieved (where Eddy current drag dominates).

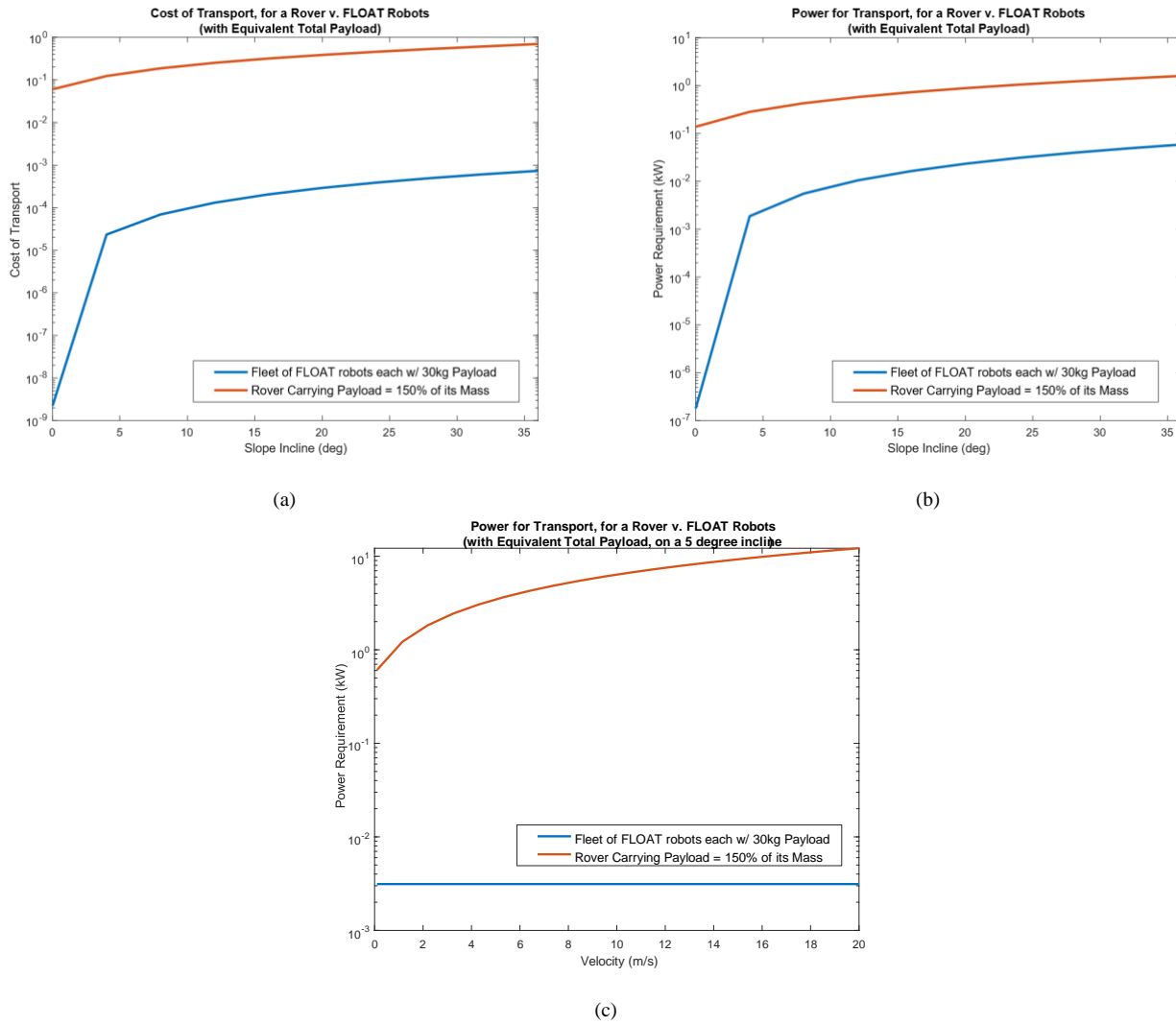


Fig. 5.6: Power and Cost of Transport Comparison. (a) Compares the cost of transport of a rover carrying a payload equivalent to 150% of its mass to the cost of transport of a fleet of FLOAT robots each carrying 30kg. The combined payload across the fleet of FLOAT robots is equivalent payload of the single rover. The cost of transport is  $\sim 10^3$ x lower for the fleet of FLOAT robots on all slopes from 0 degrees to 35 degrees. (b) Compares the total power consumption of the same 2 systems examined in (a), and the power consumption is still  $\sim 10^1$ - $10^2$ x lower for the FLOAT robots on all slope angles. (c) Compares the power requirements of the 2 systems examined in (a) and (b) however in this figure the slope is held constant at 5 degrees and only the speed is varied. The power consumption of the FLOAT robots does not appreciably depend on their speed, giving it an advantage over a wheeled rover.

## 5.2 Phase I System Design

Over the course of the Phase I task, we have refined the design of the FLOAT robots and track. Conceptual CAD models and illustrations for a realistic FLOAT system, taking into account practical design considerations such as deployment, misalignment, and dealing with non-flat terrain, are discussed in this section.

### 5.2.1 Modular Track Concept

To realize a robust system architecture, we propose designing FLOAT as a modular track system with  $\sim 1$ -2 m long x 1.2 m wide flex-circuit panels connected with compliant flexures into  $\sim 100$  m track segments, and controlled by stand-alone power electronics boxes that plug into each track panel (Fig. 5.7). Placing all power electronics components to a separate box (rather than integrating directly into the track panels) ensures that these components can remain in a thermally-controlled environment, while also maintaining the flexibility of the track and avoiding CTE issues with surface-mount components. Magnetic sensors

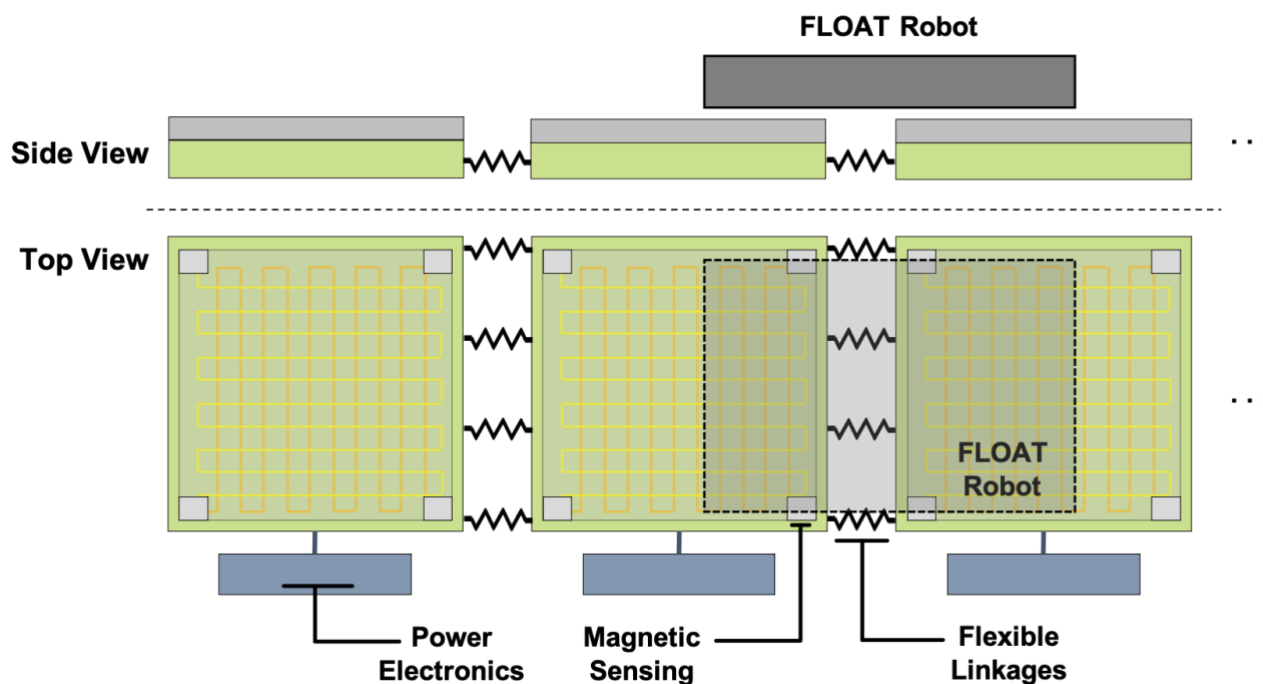


Fig. 5.7: Modular Track Concept, with flex-circuit panels connected via compliant flexures and stand-alone power electronics boxes that plug into each track panel.

at the track panel boundaries are used for closed-loop position control of the magnetic robots and to correct for misalignment between adjacent panels. This design provides robust operation under lunar conditions:

**Thermal Expansion:** flexible linkages between track segments enable expansion and contraction due to thermal gradients. Up to 1% strain is predicted in the track across a full diurnal thermal cycle ( $\sim 300^{\circ}\text{C}$ ), which equates to 1 cm of track expansion / contraction per meter, however reduced temperature ranges are expected around the lunar poles.

**Manufacturability:** individual panel segments can be made using standard available PCB panel processing without development of a continuous roll-to-roll monolithic process. Failures in individual panels can be removed / replaced easily during manufacturing, V&V, and during operation on the Moon.

**Self-Contained:** all power, control, and bus signals are self-contained in a single box, for easy wiring and replacement.

**Track Misalignment:** Magnetic sensing and closed loop feedback within panel can correct for x-y misalignment between panels.

**Redundancy:** track segments can be replaced without having to redo the entire track based on the mean-time to failure of segments

One key concept of this approach is the need for closed-loop control since individual track segments do not need to communicate directly with neighboring track segments. Coordination between track segments is accomplished through the physical handshaking of the robot as it passes over individual track segments. In addition, once the robots are up to speed, most of the robots will travel ballistically over the track only requiring the necessary power to confine the robot or automatically compensate for any misalignment in the X-Y plane of the robot. Building the system with decentralized control also simplifies control latency over long distances.

### 5.2.2 Control Electronics

Figure 5.8 shows a modular design for the control electronics for closed loop feedback. The output path of the feedback loop consists a microcontroller, digital to analog converter (DAC), and Multi-channel Power Amplifier (PWM Amplifier) which drive the individual traces in the tracks and generate forces on the robots. The input path of the feedback loop consists of sensors (i.e.

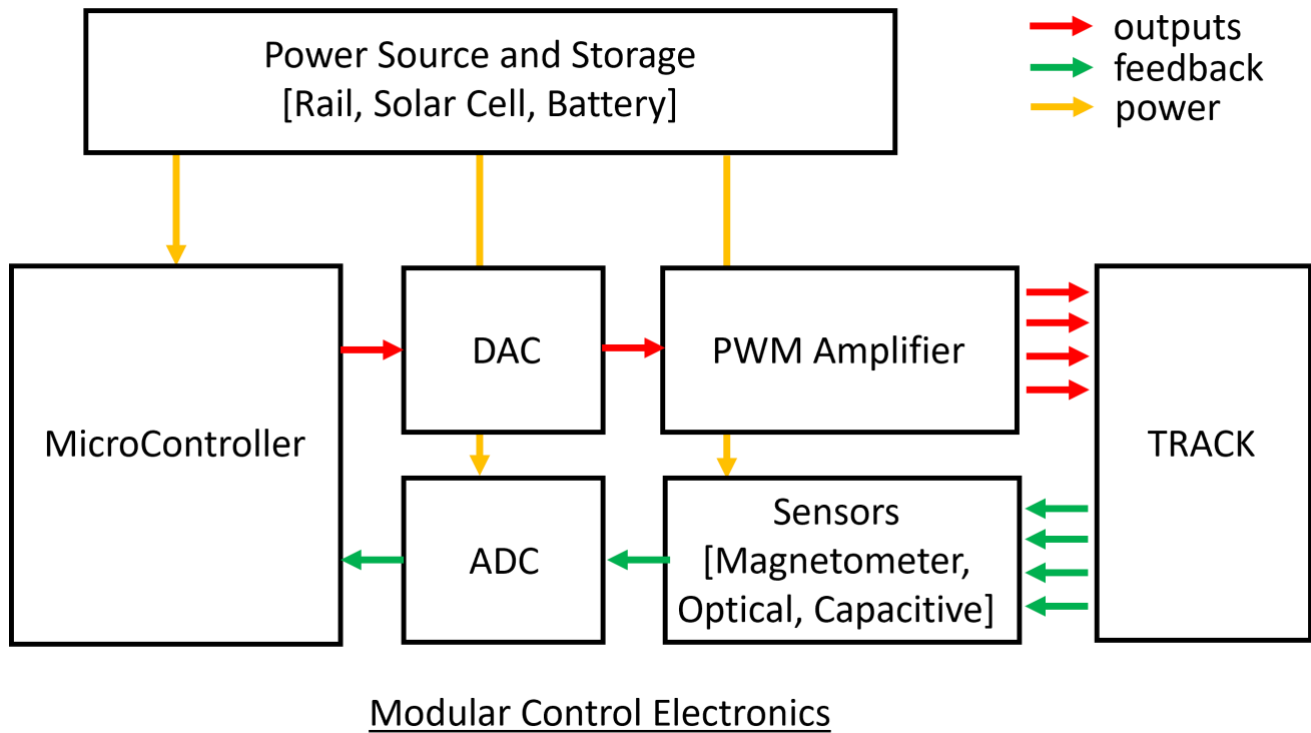


Fig. 5.8: Control Electronics

magnetometer, optical, capacitive) that measure the robot state and pose, which are feed back to the microcontroller through the analog to digital converter (ADC).

The microcontroller exerts force control on the robot by controlling the current in the track's traces; however, this can be transformed into position or velocity feedback within the microcontroller to adapt for various situations (i.e. loading and unloading material, or maintaining throughput). Typical resistances calculated from Eq. 3.27 for our FLOAT modular track, assuming traces occupying a 1m x 1m area on each track segment, are  $\sim 240 \Omega$  and thus requires a drive current of 0-0.2 A; therefore, a voltage supply of 48 V is required for the system. Depending on system complexity either local power supplies or a power rail utilizing DC/DC converters to step up/down a voltage may be required.

The control electronics are assumed to be packaged into a stand-alone module that is plugged into individual track panels. This avoids challenges that would arise if the control electronics were integrated directly into the flex-circuit tracks, including: differing coefficients of thermal expansion (which could cause surface-mount chips to delaminate from the track), differing compliance (which would reduce the ability of the track to conform to the lunar surface), and differing thickness between flex-PCB belts and rigid surface-mount components (which would make it difficult for tracks to be rolled up for transport). This modular approach also allows the control electronics to be swapped out separately from the track panels, should either component fail.

### 5.2.3 Integrated CAD Concept for FLOAT System / Deployment

The initial integrated concept for the FLOAT Robot, FLOAT Track, and a Track Deployment Robot is shown in Fig. 5.9, leveraging the results described in the prior Simulation, Experimental, and System Design sections.

Rolls of modular FLOAT tracks approximately 100 m long x 1.2 m wide with an outer diameter of  $\sim 0.9$ m when rolled up (on a 50 cm diameter spool) are mounted on a Track Deployment Robot (TDR). The TDR uses a series of articulated conveyor belts and robotic arms to deploy / recover tracks as needed on the lunar terrain. Control electronics modules for the FLOAT tracks can be stored within the track roll's spool, and accessed / deployed / connected to the tracks using the robot arms on the TDR. The TDR is approximately 2.3 m wide x 2.6 m long x 1.62 m tall (including the track spool). A separate robot equipped with plow / scoop (shown in the background of Fig. 1.1) is also required to prepare the lunar terrain over which the track is to be deployed,

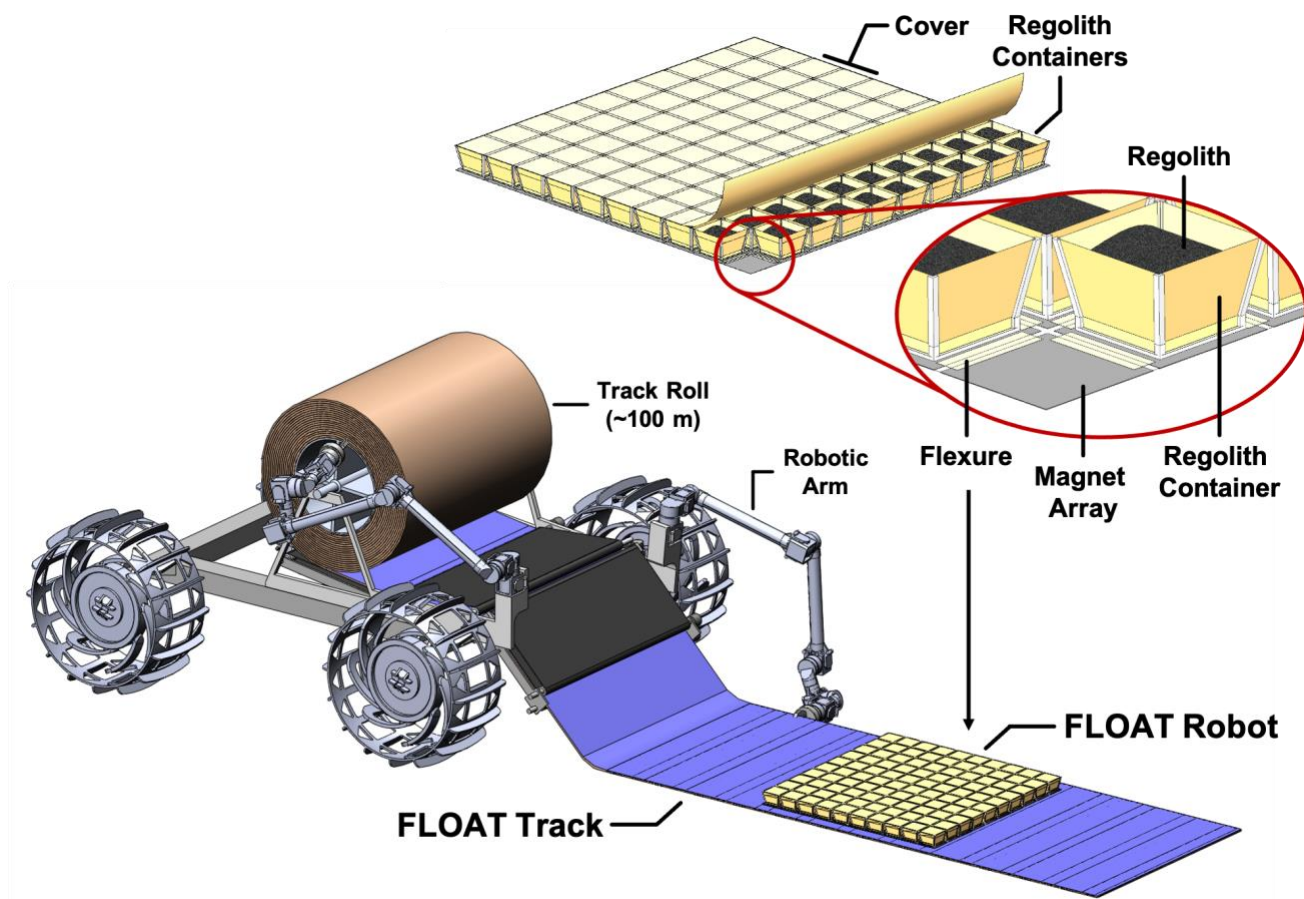


Fig. 5.9: Concept for FLOAT Robot, FLOAT Track, and Track Deployment Robot. Each FLOAT robot is 1.05 x 1.05 m and composed of one hundred 10 x 10 cm magnet arrays, that are spaced ~6 mm apart, are linked together with compliant flexures, and are each supporting a regolith container. Rolls of FLOAT tracks approximately 100 m long x 1.2 m wide with an outer diameter of ~0.9m when rolled up (on a 50 cm diameter spool) are mounted on a Track Deployment Robot (TDR), which uses a series of conveyor belts and robotic arms to deploy / recover tracks as needed. Control electronics for the FLOAT tracks can be stored within the track roll, and accessed / deployed / connected to the tracks using the robot arms on the TDR.

removing excessively-large rocks and filling in craters to meet the out-of-plane requirements of the FLOAT tracks (from Sec. 3.1.2).

Each FLOAT robot is 1.05 x 1.05 m and composed of one hundred 10 x 10 cm magnet arrays, that are spaced ~5 mm apart, are linked together with compliant flexures, and are each supporting a regolith container. A separate system (not shown) would be necessary to deploy the FLOAT robots on the track, but can be located at a staging area near the lunar base and connected into the FLOAT track network. The baseline concept of FLOAT robot deployment has all magnet robots stacked in pallets (with regolith trays stacked separately) to minimize volume during transport from Earth to the Moon. Magnet robots are then separated from one another, and regolith trays are connected onto each 10 x 10 cm magnet array using magnetic alignment features to ensure a reliable snap-in connection with proper alignment [66]. The regolith trays are 66 mm tall, 7.5 mm x 7.5 mm at their base and 9.6 mm x 9.6 mm at the top. When carrying 30 kg of lunar regolith ( $\sigma = 1.5 \text{ g/cm}^3$ ) the regolith level is ~28 mm from the bottom of the tray.

#### 5.2.4 Cost Analysis

Using existing vendors and quotations, we performed an initial cost analysis and TRL assessment for a FLOAT system, assuming the full 1 m<sup>2</sup> concept. Preliminary estimates for full-scale implementation are shown in Table 5.5, below. Track costs are substantially higher than the \$0.6-1.2 M/km cost of conventional railroads on Earth [33], but comparable to high-speed / maglev rail systems (\$4.5-31 M/km) depending on site conditions [34].

Some of these increased costs are due to the limitations of the size and economies of scale. For example, we will work



Table 5.5: Cost Analysis: order-of-magnitude cost estimates, including component TRL. These costs only cover manufacturing components (no Q&A / V&V). Control electronics are, however, estimated using rad-hardened micro-controllers / motor drivers.

System	Notes	TRL	# Units	Unit Cost	Net Cost
<b>FLOAT Track</b>	<b>Cost per km track</b>				<b>\$16.50M</b>
Flex-Circuit Layer (flex-PCB)	1.67 m x 0.55 m per panel	5-6	1800	\$3.41K	\$6.14M
Graphite Layer (pyrolytic graphite)	1.67 m x 0.55 m per panel	8	1800	\$2.36K	\$4.24M
Solar Panel Layer (thin-film panel)	Not critical path	4	1800	–	–
Control Electronics	Space / rad-tolerant hardware	5	1800	\$3.40K	\$6.12M
<b>FLOAT Robots</b>	<b>Cost per robot</b>				<b>\$37.5K</b>
Magnets	1.0 x 1.0 x 0.8 mm / magnet	8	1M	\$0.037	\$37.0K
Polyimide Tape / Film	Not appreciable cost	8	–	–	–
Regolith Trays	Not critical path	3	100	\$5	\$0.5K
Auxiliary Tools	Not critical path	4	–	–	–
<b>Support Vehicles</b>	<b>Built on BADGER frame</b>				
Deployment Robot	Need cost estimates	2	2	–	–
Terrain Preparation Robot	Need cost estimates	2	2	–	–

with flex-PCB vendors to refine estimates on future capabilities for manufacturing large-area flex-PCB using Pyralux HT – an extreme-temp. tolerant formulation that permits direct bonding of copper / polyimide without adhesives (which degrade at low temps.). Vendors that have supplied flight-qualified flex-PCBs to JPL are currently limited to 18” x 24” panels for Pyralux HT (versus 24” x 80” for standard Pyralux). More details on flex-PCB manufacturing capabilities can be found through various manufacturers [67].

The control electronics cost have been assumed using COTS rad-hard electronics and microcontrollers. Balancing the module size of the track and this cost can be done to decrease the number of electronic components.

## 6 CONCLUSION

In Phase I, we established the fundamental feasibility of FLOAT as a lunar transportation system, through a series of component- and system-level simulations, as well as targeted experimental testing on existing benchtop hardware. Our simulations validated initial extrapolations of scaling laws for robot performance (levitation pressure and height) on the moon, and allowed us to refine estimates for robot power consumption (across a range of payload mass and terrain slope), necessary robot compliance (to conform to undulating lunar terrain). Our experimental work provided proof-of-concept validation that we can design and fabricate compliant robots that conform to non-flat surfaces (without suffering from snap-in failures), as well as fabricate and operate 10 cm<sup>2</sup> robots (~10x larger area than prior state-of-the-art work). We also confirmed that FLOAT robots are able to sweep away abrasive dust from the track, and then operate over that same cleared patch for >50,000 cycles / >600 m driving distance without notable damage to either robots or track.

### Phase I Simulation / Design Accomplishments

- Validated lunar performance estimates in simulation, including: >30 kg/m<sup>2</sup> payloads, while maintaining 50-100 μm levitation gaps and using <5 W/m<sup>2</sup> for <40° inclines and >5 m bends
- Developed FLOAT system model, fit to RLSO2 mission parameters and robot lunar performance, to estimate full system size / mass / power
- Designed modular FLOAT track and conceptual track deployment robot

### Phase I Experimental Accomplishments

- Successful operation of a 10 cm<sup>2</sup> levitated magnet robot (10x larger than prior)
- Developed lunar dust mitigation approach using secondary sweeping robot
- Continuous robot operation (>600 m / >72 hrs) in simulated dust environment
- Demonstrated compliant levitating robots traversing bowls w/ 7.5 cm radius

## 6.1 Open Questions for Future Investigation

At the end of Phase I, the primary open questions / mission risks that we have identified, which will need to be investigated in future work, include:

- Closed-loop control of large-area, compliant, levitating robots is required to maximize speed and correct alignment errors between modular track panels
- Understanding the dynamics of compliant robots traversing non-flat terrain
- Understanding thermal effects of the lunar environment on the track panels (thermal expansion / buckling / misalignment) and the robot magnets (demagnetization can occur at prolonged elevated temperatures)
- Refining dust clearing / sweeping capabilities (initial tests showed electrostatic attraction of dust may require advanced cleaning end effectors)
- Estimating realistic power demands for the entire FLOAT system during operation
- Defining a technology road map for scalability / manufacturability of full-size robots / tracks

Past work has developed localized closed loop control using a microscope or camera [60], [68]; however, open questions for implementing integrated closed loop control may require other commercial sensors (i.e optical, capacitive, and magnetic) for state and pose estimation of the robot and analysis. Assuming operation at 0.5 m/s, the amount of time over each panel will be interacting with the robot is only a couple of seconds, which implies a feedback loop of 1 kHz should be plenty sufficient, which can be easily accomplished with standard micro-controllers.

As for better understanding the dynamics of compliant robots, more sophisticated simulations are required to couple both the physics of electromagnetics and rigid-body dynamics and flexures. Past work has utilized robotics simulations packages such as

Gazebo and ROS to investigate the behavior of micro-robotic systems. Adapting these custom physics plugins in Gazebo to non-planar geometries (i.e. 2D in plane rotations, and 3D bending) to enable simulations of electromagnetic and diamagnetic forces can allow us to incorporate realistic lunar terrain and track layouts, serving as a rudimentary digital twin of the deployed FLOAT system, enabling us to rapidly address both component and system level issues and failure modes. The level of physical fidelity of the simulation can be guided by experimental results (e.g. eddy current drag), however, the included physics can be tailored to balance computation speed vs physical fidelity. In addition, since Gazebo also integrates very nicely with the Robot Operating System (ROS), low level closed loop control or even high-level scheduling algorithms may also be incorporated.

More detailed thermal modelling of FLOAT under lunar conditions is also required to better understand the thermal effects due to CTE, the thermal budget to hardware operating limits, and heat transfer via radiation (between track / robots and into space) and conduction into the lunar regolith. In addition, the temperature dependent effects of diamagnetic forces of graphite and their effects on the system may also be important to understand [69], [70], and identifying design mitigations (e.g. MLI covers) to ensure the magnetic robots maintain sufficiently cool to retain magnetization during the lunar day.

Various environmental effects also have to be considered for prototyping both regolith trays and end effectors that can deal with environmental effects, such as plows / brushes for dust mitigation, ferromagnetic attractors for sweeping up ferrous particles, skirts and sheets to keep the robot clean, and electrostatic discharging spikes to minimize any effects of operation in a vacuum. This includes designing robots with fail safes such as bumper magnets to repel neighboring magnets as well as other robotic accessories for robust operation. In addition, confinement magnets may come at a cost of reduced vertical stability while increasing lateral stability; therefore, more detailed analysis of these system tradeoffs is still needed.

Power requirements for the system still need to be refined to look at the trade-offs between local power generation / storage versus a power rail, and associated electronic subsystem requirements (AC/DC inverters, local batteries, High Voltage lines, etc.) needed for full system deployment. In addition, continued development of our track deployment for modular tracks, integration with non-straight track elements (turns / junctions), and begin defining mission requirements for routing intersecting tracks or additional track spurs for track maintenance are also important remaining questions about the throughput of our FLOAT concept. To provide realistic estimates for mission-specific FLOAT track layouts on the Moon, lunar satellite imagery and digital elevation maps (DEMs) may need to be modelled since key drivers of system power consumption are the track slopes / curves around which the FLOAT robots must maneuver, so grounding our models in realistic lunar terrains are also critical for accurate system power estimates. Outputs from the system model also show the significant interdependence of system mass / volume with the number of robots, per-robot speed / payload, and track length. For this reason, Incorporating a realistic “traffic flow” model that incorporates robot acceleration / max velocity profiles on top of the realistic track layouts (e.g. hills / craters, curves, or junctions) can add to our more accurate power and system performance estimates.

Finally, the technology road map for scaling up and construction of a FLOAT track is also an open question. Manufacturability of graphite, flex tracks, and magnets have to be more closely examined. For example, Hallbach arrays offer much larger levitation forces; however, they are much more difficult to fabricate. Standard magnet arrays still offer reasonable performance; however, future work in manufacturability of both standard and Hallbach arrays is a key issue for future work. In addition, various other techniques for automating the (currently manual) process of assembling large arrays of planar magnets for these robots need to be investigated (i.e. advanced jigging and fixturing, automated robotic assembly, direct magnetic patterning [66], [71], and electromagnetic assisted self-assembly [7]). In addition further work on examining the cost and scalability of production of flex tracks and graphite is required; both are commercially available; however, neither are optimized for such large areas.

These open questions aim to address the feasibility of the FLOAT concept by further understanding the key issues related to the durability, robustness, and mean-time-to-failure (MTTF) of this approach for its adoption in future NASA missions.

## 6.2 Potential Impact

FLOAT is a mechanically-simple, low-mass, long-life system to transport payloads of all shapes / sizes around a permanent lunar base. It can reconfigure or expand – in area coverage, payload capacity, and power generation – to match the needs of a growing base. FLOAT relies on existing technologies combined in novel ways, scaled up in size, and applied to new applications. It doesn't break physics or require inventing new materials.

The Artemis program is already generating a renaissance in lunar-focused technology, science, and manned missions. FLOAT is a critical, enabling infrastructure technology for the sustainable lunar base desired in the 2030s, and brings this mission concept one step closer to reality. As a viable lunar transport system, FLOAT would also spur / be a key enabling technology for fledgling commercial interests in lunar resource mining [72], [73]. Finally, FLOAT inspires comparisons to the flying cars and magnetic-levitation trains of science fiction lore that have captured public imagination for nearly 100 years.

FLOAT technology can also be infused into short- and mid-term NASA missions, outside the scope of a long-term lunar base mission presented in this work. FLOAT can serve as a low-cost, low-mass substitute for robotic arms deployed on a CLPS lander on the Moon (short-term) or on Discovery / New Frontiers-class landers on low-gravity worlds like Titan, Europa, or Enceladus (mid-term). The lander would unroll FLOAT tracks onto the terrain (e.g. using air pressure, like a party horn, or shape-memory-alloys), and use FLOAT robots to transport scientific instruments (microscopes, ground-penetrating radar, seismometers, etc.) off the lander or retrieve regolith samples for onboard analysis. Such a system could potentially access terrain tens of meters in radius around the lander, as compared to 1-2 meters for a robot arm. FLOAT can also function in micro-gravity as reaction wheels for cubesats, as a space station transport system, or provide dynamic thermal control / micro-meteorite shielding to the station (using FLOAT robots carrying thermal reflectors / ceramic plates).

Improved FLOAT technology can also be deployed on Earth to enable high-precision manufacturing (SRI's Microfactory [5]), spur development of new low-friction magnetic bearing or actuator technologies (for no-touch object manipulation), and create dynamic art installations.

## REFERENCES

- [1] NASA, “Forward to the Moon: NASA’s Strategic Plan for Human Exploration.” 2019. Available: [https://www.nasa.gov/sites/default/files/atoms/files/america\\_to\\_the\\_moon\\_2024\\_artemis\\_20190523.pdf](https://www.nasa.gov/sites/default/files/atoms/files/america_to_the_moon_2024_artemis_20190523.pdf)
- [2] NASA, “New VIPER Lunar Rover to Map Water Ice on the Moon.” 2019. Available: <https://www.nasa.gov/feature/new-viper-lunar-rover-to-map-water-ice-on-the-moon>
- [3] NASA Science, “Moon’s South Pole in NASA’s Landing Sites.” 2019. Available: <https://solarsystem.nasa.gov/news/907/moons-south-pole-in-nasas-landing-sites/>
- [4] M. Chamberlain, S. Kiefer, and J. Banik, “Roll-Out Solar Array (ROSA).” 2019. Available: [https://www.nasa.gov/mission\\_pages/station/research/experiments/explorer/Investigation.html?#id=1876](https://www.nasa.gov/mission_pages/station/research/experiments/explorer/Investigation.html?#id=1876)
- [5] E. Ackerman, “SRI’s Micro Robots Can Now Manufacture Their Own Tools.” 2016.
- [6] R. Pelrine *et al.*, “Diamagnetically levitated robots: An approach to massively parallel robotic systems with unusual motion properties,” in *IEEE ICRA 2012*, May 2012, pp. 739–744. doi: [10.1109/ICRA.2012.6225089](https://doi.org/10.1109/ICRA.2012.6225089).
- [7] R. Pelrine, A. Wong-Foy, A. Hsu, and B. McCoy, “Self-assembly of milli-scale robotic manipulators: A path to highly adaptive, robust automation systems,” in *MARSS 2016*, Jul. 2016, pp. 1–6. doi: [10.1109/MARSS.2016.7561728](https://doi.org/10.1109/MARSS.2016.7561728).
- [8] R. Pelrine, A. Hsu, A. Wong-Foy, B. McCoy, and C. Cowan, “Optimal control of diamagnetically levitated milli robots using automated search patterns,” in *MARSS 2016*, Jul. 2016, pp. 1–6. doi: [10.1109/MARSS.2016.7561725](https://doi.org/10.1109/MARSS.2016.7561725).
- [9] R. Pelrine, A. Hsu, C. Cowan, and A. Wong-Foy, “Multi-agent systems using diamagnetic micro manipulation — From floating swarms to mobile sensors,” in *MARSS 2017*, Jul. 2017, pp. 1–6. doi: [10.1109/MARSS.2017.8001930](https://doi.org/10.1109/MARSS.2017.8001930).
- [10] J. Jean, A. Wang, and V. Bulović, “In situ vapor-deposited parylene substrates for ultra-thin, lightweight organic solar cells,” *Organic Electronics*, vol. 31, pp. 120–126, Apr. 2016, doi: [10.1016/j.orgel.2016.01.022](https://doi.org/10.1016/j.orgel.2016.01.022).
- [11] “Empa - Communication - A new world record for solar cell efficiency.” Available: <https://www.empa.ch/web/s604/weltrekord>
- [12] NASA STMD, “Kilopower.” 2019. Available: [nasa.gov/directorates/spacetech/kilopower](https://nasa.gov/directorates/spacetech/kilopower)
- [13] M. Heverly, J. Matthews, M. Frost, C. McQuin, and C. Quin, “Development of the Tri-ATHLETE Lunar Vehicle Prototype,” in *40th aerospace mechanisms symposium*, May 2010, p. 10. Available: [https://www-robotics.jpl.nasa.gov/publications/Matthew\\_Heverly/Heverly\\_2010\\_AMS\\_Tri-ATHLETE.pdf](https://www-robotics.jpl.nasa.gov/publications/Matthew_Heverly/Heverly_2010_AMS_Tri-ATHLETE.pdf)
- [14] R. P. Mueller, R. E. Cox, T. Ebert, J. D. Smith, J. M. Schuler, and A. J. Nick, “Regolith Advanced Surface Systems Operations Robot (RASSOR),” *IEEE Aerospace Conference Proceedings*, pp. 1–10, 2013, doi: [10.1109/AERO.2013.6497341](https://doi.org/10.1109/AERO.2013.6497341).
- [15] NASA, “Space Exploration Vehicle Concept.” NASA, pp. 2–4. Available: [https://www.nasa.gov/pdf/464826main\\_SEV\\_FactSheet\\_508.pdf](https://www.nasa.gov/pdf/464826main_SEV_FactSheet_508.pdf)
- [16] NASA JSC, “Spidernaut.” Available: <https://spidernaut.jsc.nasa.gov/>
- [17] L. A. Taylor, “The lunar dust problem: a possible remedy,” in *Space resources roundtable II*, 2000, p. 2. Available: <http://adsabs.harvard.edu/abs/2000srtr.conf...71T>
- [18] C. I. Calle, C. R. Buhler, M. R. Johansen, M. D. Hogue, and S. J. Snyder, “Active dust control and mitigation technology for lunar and Martian exploration,” *Acta Astronautica*, vol. 69, no. 11–12, pp. 1082–1088, 2011, doi: [10.1016/j.actaastro.2011.06.010](https://doi.org/10.1016/j.actaastro.2011.06.010).
- [19] C. I. Calle, C. R. Buhler, J. L. McFall, and S. J. Snyder, “Particle removal by electrostatic and dielectrophoretic forces for dust control during lunar exploration missions,” *Journal of Electrostatics*, vol. 67, no. 2–3, pp. 89–92, 2009, doi: [10.1016/j.elstat.2009.02.012](https://doi.org/10.1016/j.elstat.2009.02.012).
- [20] P. D. Spudis, K. R. Stockstill, W. J. Ockels, and M. Kruijff, “Physical environment of the lunar south pole from clementine data: implications for the future exploration of the Moon,” in *Lunar and planetary science conference*, 1995, p. 1339. Available: <https://adsabs.harvard.edu/full/1995LPI....26.1339S>
- [21] A. Austin *et al.*, “RLSO2 – Robotic Lunar Surface Operations 2,” NASA JPL, 2019.
- [22] A. Austin *et al.*, “Robotic Lunar Surface Operations 2,” in *International astronomical congress (IAC)*, 2019, p. 13.
- [23] A. S. Howe *et al.*, “Planetary Autonomous Construction System (P@X),” in *International astronomical congress (IAC)*, 2019, p. 11.
- [24] J. Elliott *et al.*, “ISRU in Support of an Architecture for a Self-Sustained Lunar Base,” in *International astronomical congress (IAC)*, 2019, p. 10.
- [25] D. S. McKay *et al.*, “Lunar Sourcebook: A User’s Guide to the Moon,” in *Lunar sourcebook: A user’s guide to the moon*, Available: [https://www.lpi.usra.edu/publications/books/lunar\\_sourcebook/pdf/Chapter07.pdf](https://www.lpi.usra.edu/publications/books/lunar_sourcebook/pdf/Chapter07.pdf)
- [26] “Planetary Simulant Database.” Available: <https://simulantdb.com/>
- [27] A. Ivankov, “Luna 13.” Available: <https://nssdc.gsfc.nasa.gov/nmc/spacecraft/display.action?id=1966-116A>
- [28] N. L. Division and P. Programs, “Surveyor Program Results,” NASA; NASA Scientific; Technical Information Division, 1969. Available: <https://archive.org/details/surveyorprogramr00unit/page/n5/mode/2up>
- [29] D. A. Kring, “Parameters of Lunar Soils,” 2006. Available: [https://www.lpi.usra.edu/science/kring/lunar\\_exploration/briefings/lunar\\_soil\\_physical\\_properties.pdf](https://www.lpi.usra.edu/science/kring/lunar_exploration/briefings/lunar_soil_physical_properties.pdf)
- [30] D. A. Kring, “Regolith properties of permanently shadowed regions (PSRs) in polar regions of the Moon and implications for rover trafficability : Outlining the problem,” 2015. Available: <https://sservi.nasa.gov/prw/downloads/presentations/kring.pdf>
- [31] W. D. Carrier III, “The four things you need to know about the GEOTECHNICAL PROPERTIES OF LUNAR SOIL,” 2005.
- [32] C. Meyer, “NASA Lunar Petrographic Educational Thin Section Set,” Planetary Materials Branch, Solar System Exploration Division, NASA Johnson Space Center, 2003. Available: <https://www-curator.jsc.nasa.gov/education/lpetss/index.cfm>



- [33] University of Central Florida, “LHS-1 Lunar Highlands Simulant.” [Online]. Available: <https://sciences.ucf.edu/class/simulant/lunarhighlands/>
- [34] B. Wilcox, A. Nasif, and R. Welch, “Implications of martian rock distributions on rover scaling,” *International Conf on Mobile Planetary Robots & Rovers Roundup*, 1997, Available: <https://trs.jpl.nasa.gov/handle/2014/21727>
- [35] J. L. Bandfield, R. R. Ghent, A. R. Vasavada, D. A. Paige, S. J. Lawrence, and M. S. Robinson, “Lunar surface rock abundance and regolith fines temperatures derived from LRO Diviner Radiometer data,” *Journal of Geophysical Research*, vol. 116, p. E00H02, Dec. 2011, doi: [10.1029/2011JE003866](https://doi.org/10.1029/2011JE003866).
- [36] C. Elder *et al.*, “The Lunar Rock Size Frequency Distribution from Diviner Infrared Measurements,” 2016. Available: <https://trs.jpl.nasa.gov/handle/2014/47289>
- [37] C. Elder, “THE LUNAR ROCK SIZE FREQUENCY DISTRIBUTION DERIVED FROM THERMAL INFRARED OBSERVATIONS,” 2021. doi: [10.1130/abs/2021AM-370792](https://doi.org/10.1130/abs/2021AM-370792).
- [38] B. Li, Z. Ling, J. Zhang, and J. Chen, “Rock size-frequency distributions analysis at lunar landing sites based on remote sensing and in-situ imagery,” *Planetary and Space Science*, vol. 146, pp. 30–39, Oct. 2017, doi: [10.1016/j.pss.2017.08.008](https://doi.org/10.1016/j.pss.2017.08.008).
- [39] B. Li, Z. Ling, J. Zhang, and J. Chen, “Rock size-frequency distributions at lunar landing sites,” *48th Lunar and Planetary Science Conference*, pp. 2–3, 2017, Available: <https://www.hou.usra.edu/meetings/lpsc2017/pdf/1800.pdf>
- [40] J. Plescia, “The Moon – The Lunar Surface.” 2008. Available: [http://www.spudislunarresources.com/moon101/moon\\_101\\_surface.pdf](http://www.spudislunarresources.com/moon101/moon_101_surface.pdf)
- [41] “Earth’s Moon – NASA Solar System Exploration.” Available: <https://solarsystem.nasa.gov/moons/earths-moon/in-depth/>
- [42] “Casting Light on Permanently Shadowed Regions | Lunar Reconnaissance Orbiter Camera.” Available: <http://lroc.sese.asu.edu/posts/979>
- [43] M. T. Zuber *et al.*, “Constraints on the volatile distribution within Shackleton crater at the lunar south pole,” *Nature*, vol. 486, no. 7403, pp. 378–381, Jun. 2012, doi: [10.1038/nature11216](https://doi.org/10.1038/nature11216).
- [44] S. Yu and W. Fa, “Thermal conductivity of surficial lunar regolith estimated from Lunar Reconnaissance Orbiter Diviner Radiometer data,” *Planetary and Space Science*, vol. 124, pp. 48–61, May 2016, doi: [10.1016/j.pss.2016.02.001](https://doi.org/10.1016/j.pss.2016.02.001).
- [45] P. D. Spudis, B. Bussey, J. Plescia, J.-L. Josset, and S. Beauvivre, “Geology of Shackleton Crater and the south pole of the Moon,” *Geophys. Res. Lett.*, vol. 35, p. 14201, 2008, doi: [10.1029/2008GL034468](https://doi.org/10.1029/2008GL034468).
- [46] R. V. Wagner, M. S. Robinson, E. J. Speyerer, and P. Mahanti, “Topography of 20-km Diameter Craters on the Moon,” 2013. Available: <https://www.lpi.usra.edu/meetings/lpsc2013/eposter/2924.pdf>
- [47] J. D. Jackson, *Classical Electrodynamics*, 3rd ed. New York, NY, USA: Wiley, 1999.
- [48] W. Thomson, “On the forces experienced by small spheres under magnetic influence; and on some of the phenomena presented by diamagnetic substances,” 1847.
- [49] W. Braunbek, “Freies Schweben diamagnetischer Körper im Magnetfeld,” *Zeitschrift für Physik*, vol. 112, no. 11–12, pp. 764–769, Nov. 1939, doi: [10.1007/BF01339980](https://doi.org/10.1007/BF01339980).
- [50] M. D. Simon and A. K. Geim, “Diamagnetic levitation: Flying frogs and floating magnets (invited),” *Journal of Applied Physics*, vol. 87, no. 9, pp. 6200–6204, May 2000, doi: [10.1063/1.372654](https://doi.org/10.1063/1.372654).
- [51] R. E. Pelrine, “Magnetic field levitation.” Mar. 1995. Available: <https://patents.google.com/patent/US5396136A/en>
- [52] E. E. Hunter, E. B. Steager, A. Hsu, A. Wong-Foy, R. Pelrine, and V. Kumar, “Nanoliter Fluid Handling for Microbiology Via Levitated Magnetic Microrobots,” *IEEE Robotics and Automation Letters*, vol. 4, no. 2, pp. 997–1004, Apr. 2019, doi: [10.1109/LRA.2019.2893682](https://doi.org/10.1109/LRA.2019.2893682).
- [53] A. Hsu *et al.*, “Diamagnetically levitated Milli-robots for heterogeneous 3D assembly,” *Journal of Micro-Bio Robotics*, vol. 14, no. 1–2, pp. 1–16, Jun. 2018, doi: [10.1007/s12213-018-0103-4](https://doi.org/10.1007/s12213-018-0103-4).
- [54] A. Hsu *et al.*, “Application of micro-robots for building carbon fiber trusses,” in *2016 international conference on manipulation, automation and robotics at small scales (MARSS)*, Jul. 2016, pp. 1–6. doi: [10.1109/MARSS.2016.7561729](https://doi.org/10.1109/MARSS.2016.7561729).
- [55] J. F. Schenck, “The role of magnetic susceptibility in magnetic resonance imaging: MRI magnetic compatibility of the first and second kinds,” *Medical Physics*, vol. 23, no. 6, pp. 815–850, Jun. 1996, doi: [10.1118/1.597854](https://doi.org/10.1118/1.597854).
- [56] M. Kaczmarzyk, M. Gawronski, and G. Piatkowski, “Global database of direct solar radiation at the Moon’s surface for lunar engineering purposes,” *E3S Web of Conferences*, vol. 49, p. 00053, Aug. 2018, doi: [10.1051/e3sconf/20184900053](https://doi.org/10.1051/e3sconf/20184900053).
- [57] H.-L. Chen *et al.*, “A 19.9%-efficient ultrathin solar cell based on a 205-nm-thick GaAs absorber and a silver nanostructured back mirror,” *Nature Energy*, vol. 4, no. 9, pp. 761–767, Sep. 2019, doi: [10.1038/s41560-019-0434-y](https://doi.org/10.1038/s41560-019-0434-y).
- [58] S. Bose *et al.*, “A morphological and electronic study of ultrathin rear passivated Cu(In,Ga)Se<sub>2</sub> solar cells,” *Thin Solid Films*, vol. 671, pp. 77–84, Feb. 2019, doi: [10.1016/j.tsf.2018.12.028](https://doi.org/10.1016/j.tsf.2018.12.028).
- [59] P. Centeno *et al.*, “Self-Cleaned Photonic-Enhanced Solar Cells with Nanostructured Parylene-C,” *Advanced Materials Interfaces*, vol. 7, no. 15, p. 2000264, Aug. 2020, doi: [10.1002/admi.202000264](https://doi.org/10.1002/admi.202000264).
- [60] A. Hsu *et al.*, “Automated 2D micro-assembly using diamagnetically levitated milli-robots,” in *2017 international conference on manipulation, automation and robotics at small scales (MARSS)*, Jul. 2017, pp. 1–6. doi: [10.1109/MARSS.2017.8001926](https://doi.org/10.1109/MARSS.2017.8001926).
- [61] A. Elements, “Pyrolytic Graphite.” Available: <https://www.americanelements.com/pyrolytic-graphite-7782-42-5>
- [62] “K&J Magnetics - Specifications.” Available: <https://www.kjmagnetics.com/specs.asp>
- [63] A. S. Howe, B. H. Wilcox, M. Barmatz, and G. Voecks, “ATHLETE as a Mobile ISRU and Regolith Construction Platform,” in *Earth & space 2016*, 2016, pp. 1–15.
- [64] A. S. Howe and B. Wilcox, “Outpost Assembly using the ATHLETE Mobility System,” in *IEEE aerospace conference*, 2016, p. 9. doi: [10.1109/AERO.2016.7500794](https://doi.org/10.1109/AERO.2016.7500794).

- [65] V. Radhakrishnan, “Locomotion: Dealing with friction,” *Proceedings of the National Academy of Sciences*, vol. 95, no. 10, pp. 5448–5455, May 1998, doi: [10.1073/pnas.95.10.5448](https://doi.org/10.1073/pnas.95.10.5448).
- [66] C. Velez Cuervo, “Engineering Microscale Magnetic Devices for Next-Generation Microrobotics,” pp. 1–239, 2017, Available: <https://ufdc.ufl.edu/UFE0051516/00001>
- [67] Pioneer Circuits, “Extended Length Flexible Circuitry: A Short History.” Available: <https://www.pioneercircuits.com/extended-length-flexible-circuitry-a-short-history/>
- [68] A. Hsu, H. Zhao, M. Gaudreault, A. W. Foy, and R. Pelrine, “Magnetic Milli-Robot Swarm Platform: A Safety Barrier Certificate Enabled, Low-Cost Test Bed,” *IEEE Robotics and Automation Letters*, vol. 5, no. 2, pp. 2913–2920, Apr. 2020, doi: [10.1109/LRA.2020.2974713](https://doi.org/10.1109/LRA.2020.2974713).
- [69] M. Ewall-Wice *et al.*, “Optomechanical Actuation of Diamagnetically Levitated Pyrolytic Graphite,” *IEEE Transactions on Magnetics*, vol. 55, no. 7, Jul. 2019, doi: [10.1109/TMAG.2019.2892332](https://doi.org/10.1109/TMAG.2019.2892332).
- [70] M. Kobayashi and J. Abe, “Optical Motion Control of Maglev Graphite,” *Journal of the American Chemical Society*, vol. 134, no. 51, pp. 20593–20596, Dec. 2012, doi: [10.1021/ja310365k](https://doi.org/10.1021/ja310365k).
- [71] C. Velez and D. Arnold, “Batch-fabrication of magnetically patterned bases for diamagnetically levitated micro-robots.”
- [72] J. Bridenstine, “Space Resources are the Key to Safe and Sustainable Lunar Exploration.” Sep. 2020. Available: <https://blogs.nasa.gov/bridenstine/2020/09/10/space-resources-are-the-key-to-safe-and-sustainable-lunar-exploration/>
- [73] NASA, “Purchase of Lunar Regolith and/or Rock Materials from Contractor.” 2020. Available: <https://beta.sam.gov/opp/77726177617a45d0a196e23a587d7c14/view>

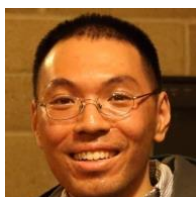
## BIOGRAPHIES



**Ethan W. Schaler, Ph.D. (NASA JPL)** Dr. Ethan Schaler is a member of the Robotic Actuation and Sensing group, within the Mobility and Robotic Systems section at NASA JPL, where he supports both research and flight tasks. As a Robotic Systems Engineer on the Mars 2020 project, he currently supports tactical and strategic sampling operations of the Perseverance rover's robotic arm and sample caching subsystem on Mars. Previously, he has performed planning, commissioning, testing (V&V), and analysis of the rover's Robotic Arm and integrated force / torque sensor. As a researcher, he has also supported multiple DARPA and DOD research tasks, involving construction of legged robots, flexible grippers, and more.

He is an expert in designing unique meso-scale robotic systems – particularly those that integrate flexible structures, actuators, adhesives, and sensors. He manufactures these systems using a combination of macro-scale (3D printing, machining, etching) and micro-scale techniques (deposition, micromachining).

Dr. Schaler received a B.S. in Mechanical Engineering from the University of Maryland, College Park in 2011, an M.Phil. in Micro- / Nano-Technology Enterprise from the University of Cambridge in 2012, and a Ph.D. in Electrical Engineering from the University of California, Berkeley in 2018. He has previously been awarded a Churchill Scholarship, Goldwater Scholarship, NSF GRFP Fellowship, and NDSEG Fellowship. Dr. Schaler is a 2-time NIAC fellow.



**Allen Hsu, Ph.D. (SRI International)** Dr. Allen Hsu is a Research Engineer in the Robotics Group within the Advanced Technology and Systems Division at SRI International. His research interests lie in the fields of micro-robotics, swarm controls, micro heterogenous assembly, and electro-magnetic systems including diamagnetic levitating systems and motors. As part of his work, Dr. Hsu has been involved in the design, implementation, and operation of multiple magnetically driven hardware platforms for magnetic manipulation of objects at the micro to cm size-scale.

Dr. Hsu received a B.S. in Electrical Engineering from Princeton University in 2006, and an M.S. and Ph.D. in Electrical Engineering and Computer Science from the Massachusetts Institute of Technology in 2008 and 2014, respectively.



**Ronald Pelrine, Ph.D. (SRI International / Pelrine Innovations)** Dr. Pelrine was a Chief Scientist for SRI International until May 2021, and more recently is CEO of his startup company Pelrine Innovations LLC. Dr. Pelrine is a world leader in diamagnetic levitation and micro robotics with over 30 years experience in both fields. He developed and patented the world's first self-levitated magnet array using diamagnetic levitation, a basic technology advance that is at the core of FLOAT. Dr. Pelrine also has long term experience in magnetic drives using flex and PCB circuits as well as conventional coils. He currently holds approximately 115 patents, including in the fields of diamagnetic levitation and electromagnetic drives.

Dr. Pelrine received his B.S. in Physics from the Massachusetts Institute of Technology, an M.S. in Physics from the University of Washington, Seattle, and a Ph.D. in Mechanical Engineering from the University of Texas, Austin.



**A. Scott Howe, Ph.D. (NASA JPL)** Dr. Scott Howe is a licensed architect and robotics engineer at NASA's Jet Propulsion Laboratory. He earned PhDs in industrial and manufacturing systems engineering from Hong Kong University and in architecture from University of Michigan. Dr. Howe spent 13 years of practice in Tokyo, Japan, and speaks, reads, and writes fluent Japanese on a technical level. He taught for 6 years at Hong Kong University. In addition, he has 29 years of experience specializing in robotic construction and currently supports NASA Lunar Surface Systems efforts and is on the NASA development team building long-duration human habitats for deep space and permanent outposts for the moon and Mars. Dr. Howe is also a member of the JPL All-Terrain Hex-Limbed Extra-Terrestrial Explorer (ATHLETE) robotic mobility system development team, and STMD ISRU Excavation team.



**Rui J. de Gouvea Pinto (NASA JPL / Georgia Institute of Technology)** Rui J. de Gouvea Pinto is a Mechanical Engineering Intern at NASA JPL, working on both the FLOAT NIAC study and a Europa Lander research testbed. He is currently completing his Mechanical Engineering degree at the Georgia Institute of Technology, with a minor in Computing and Intelligence. Rui has also conducted research in the Intelligent Robotics & Emergent Automation Lab at Georgia Tech, on drone docking and take-off from a moving vehicle, and held prior internships at Area-I and GE Appliances.